## *The Development of Microfluidic and Plasmonic Devices for Terahertz Frequencies*

BARAGWANATH, ADAM,JOHN

# The Development of Microfluidic and Plasmonic Devices for Terahertz Frequencies

Adam John Baragwanath

A Thesis submitted for the degree of Doctor of Philosophy

Department of Physics

Durham University


July 2011

## Abstract

The wealth of opportunities associated with the terahertz (THz) region of the electromagnetic spectrum have only recently, thanks to advances in technology, begun to be fully recognised and exploited. The advent of terahertz time-domain spectroscopy (THz-TDS) has led to a wide spectrum of research, spanning chemical, biological and physical systems. However, the relative immaturity of THz techniques results in a variety of inherent problems which limit the potential applications. With an equality existing between the wavelength of THz radiation, and the length scales associated with modern microfabrication techniques, such technology can be exploited to facilitate in finding solutions to these problems.

This thesis seeks to address one of these problems, namely the strong absorptions associated with liquid water in the THz region. A simple design idea, that if the optical path length through a fluidic sample were reduced, strong signals could be detected after direct transmission, resulted in a micromachined fluidic cell being devised. The design, fabrication and testing of a microfluidic device inherently transparent to THz radiation, and designed for use in a standard THz-TDS arrangement, is presented. A range of samples, including primary alcohol-water mixtures, commercial whiskies and organic materials are analysed, which, when used in conjunction with data extraction algorithms, allows for accurate dielectric information to be yielded.

Further exploitation of micromachining techniques are presented, where a variety of structures, seeking to initiate and utilise a class of surface electromagnetic wave known as surface plasmon polaritons (SPPs), are realised. By flanking a single sub-wavelength aperture with sub-wavelength periodic corrugations, extraordinary optical transmission (EOT) can be observed. This technique allows smaller apertures to be used for THz near-field imaging applications, with a view to increase spatial resolution. The first demonstration

of THz near-field imaging using sub-wavelength plasmonic apertures in conjunction with a THz quantum cascade laser source, is presented.

Detailed investigations into EOT for the case of two-dimensional, sub-wavelength aperture arrays are documented. A qualitative time-of-flight model describing the transmission properties of these structures is presented, resulting from systematic investigations into a variety of geometrical effects. This model has allowed sharp resonances to be engineered in the frequency domain. A hybrid device featuring a combination of sub-wavelength periodic apertures and corrugations is also investigated. Such a structure is not known to have been described previously in the literature, either in the optical or THz domains. The device demonstrates unparallelled transmission efficiencies, termed 'super' EOT.

Finally, a device combining the microfluidic technology with the highly resonant SPP structures is presented. This device seeks to exploit the innate dependence of SPPs to a metal-dielectric interface, for use as a sensor. By introducing a range of fluids into the device, the change in the metal-dielectric interface induced a change in the frequency response of the resonant structure. The magnitude of the observed frequency shift can be related back to the dielectric properties of the fluid. This result displays how microfabrication techniques can be successfully exploited to create devices for THz applications, seeking to provide solutions to the inherent problems associated with this part of the electromagnetic spectrum.

# Table of Contents

# Acknowledgements

I would like to begin by thanking my supervisors, Professor Martyn Chamberlain and Dr. Andrew Gallant, for their commitment, guidance and support throughout my PhD. In particular, I would like to thank Martyn for introducing me to all things THz, the initial offer of a PhD, and for his unrivalled knowledge of the field. Likewise, I thank Andrew for the almost daily technical support, advice and reassurance, concerning everything from data analysis, to broken vacuum pumps. It has been a great pleasure and privilege to work with them both, and I will miss our fruitful Friday morning discussions.

Much of the fabrication work in this thesis would not have been possible without the help of Dr. Mark Rosamond. I would like to thank him for his constant help, ideas, advice and general company in the cleanroom. The majority of the devices presented in this thesis are a product of his extensive knowledge, technical skills and passionate dedication to the lab. I would also like to thank Dr. DeChang Dai for his help with the laser. It is down to his knowledge and expertise that the laser has survived this long, and seen me through my PhD. Also, I would like to thank Dr. Peter Swift for showing me the ropes in the THz lab.

I would also like to thank Dr. Axel Zeitler and Dr. Joshua Freeman for allowing me to spend time at the Cavendish Laboratory to work on the QCL imaging experiments. I thank them for their commitment to the work, and for the enjoyable evenings at Gonville and Caius College.

I would like to thank my friends and family for their support and company throughout my seven years of study at Durham. Special thanks go to my girlfriend Rachael for her friendship, love and support over the past three years, and for generally putting up with me! Finally, I would like to thank my parents for their constant love and support, and convincing me a PhD was the right thing to do. As usual, they were right.

# Copyright

# Publication List

The work in this thesis has featured in the following publications:

## Journal Articles

- **Chapter 3:** A. J. Baragwanath, G. P. Swift, D. Dai, A. J. Gallant, and J. M. Chamberlain, "Silicon based microfluidic cell for terahertz frequencies", *J. Appl. Phys., vol. 108, 013102, (2010).*

- **Chapter 3:** A. J. Baragwanath, G. P. Swift, D. Dai, D. Zeze, A. J. Gallant, and J. M. Chamberlain, "Micro-machined fluidic devices for terahertz time-domain spectroscopy", *Phys. Status Solidi C, vol. 1-3, DOI 10.1002/pssc.201084088, (2011).*

- **Chapter 5:** A. J. Baragwanath, J. R. Freeman, A. J. Gallant, J. A. Zeitler, H. E. Beere, D. A. Ritchie, and J. M. Chamberlain, "Terahertz near-field imaging using sub-wavelength plasmonic apertures and a quantum cascade laser source", *Opt. Lett., vol. 36, no. 13, pp. 2393-2395, (2011).*

- **Chapter 6:** A. J. Baragwanath, M. Rosamond, A. J. Gallant, and J. M. Chamberlain, "Time-of-flight model for the extraordinary transmission through periodic arrays of subwavelength apertures at THz frequencies", *Plasmonics, vol. 6, no. 3, DOI 10.1007/s11468-011-9244-1, (2011).*

## Conference Papers

- **Chapter 3:** A. J. Baragwanath, G. P. Swift, D. Dai, A. J. Gallant, and J. M. Chamberlain, "Silicon based microfluidic device for terahertz frequencies", in *35th International Conference on Infrared, Millimeter and Terahertz Waves, (Rome, Italy), DOI: 10.1109/ICIMW.2010.5612777, September 2010.*

- **Chapter 3:** A. J. Baragwanath, G. P. Swift, D. Dai, D. Zeze, A. J. Gallant, and J. M. Chamberlain, "Micro-machined fluidic devices for terahertz time-domain spectroscopy", in *Fourth International Conference on Optical, Optoelectronic and Photonic Materials and Applications, (Budapest, Hungary), August 2010.*

- **Chapter 5:** A. J. Baragwanath, J. R. Freeman, A. J. Gallant, J. A. Zeitler, H. E. Beere, D. A. Ritchie, and J. M. Chamberlain, "Plasmonic Apertures for THz QCL Near-Field Imaging", in *35th International Conference on Infrared, Millimeter and Terahertz Waves, (Rome, Italy), DOI: 10.1109/ICIMW.2010.5612861, September 2010.*

- **Chapter 6:** A. J. Baragwanath, M. Rosamond, A. J. Gallant, and J. M. Chamberlain, "Time-of-flight model for the extraordinary optical transmission through 2-dimensional aperture arrays", submitted to *36th International Conference on Infrared, Millimeter and Terahertz Waves, (Houston, TX), October 2011.*

- **Chapter 6:** A. J. Baragwanath, M. Rosamond, A. J. Gallant, and J. M. Chamberlain, "A hybrid aperture-corrugation plasmonic device demonstrating super extraordinary transmission at terahertz frequencies", submitted to *36th International Conference on Infrared, Millimeter and Terahertz Waves, (Houston, TX), October 2011.*

## Book Chapters

- **Chapter 4:** A. J. Baragwanath, A. J. Gallant, and J. M. Chamberlain, *Terahertz Plasmonic Structures in Terahertz Spectroscopy: Theory and Applications, Berlin: Springer-Verlag, 2011. To be published.*

## Further Publications

Further publications on which I am an author:

- **Journal Paper:** G. P. Swift, A. J. Gallant, N. Kaliteevskaya, M. A. Kaliteevski, S. Brand, D. Dai, A. J. Baragwanath, I. Iorsh, R. A. Abram, and J. M. Chamberlain, "Negative refraction and the spectral filtering of terahertz radiation by a photonic crystal prism" *Opt. Lett., vol. 36, 9, pp. 1641-1643, (2011).*

- **Conference Paper:** G. P. Swift, N. Kaliteevskaya, D. Dai, M. A. Kaliteevski, A. J. Baragwanath, A. J. Gallant, and J. M. Chamberlain, "Negatively refracting plasmonic devices at THz frequencies", in *35th International Conference on Infrared, Millimeter and Terahertz Waves, (Rome, Italy), DOI: 10.1109/ICIMW.2010.5612539, September 2010.*

- **Conference Paper:** M. G. King, A. J. Baragwanath, M. C. Rosamond, D. Wood, and A. J. Gallant, "Porous PDMS force sensitive resistors", Procedia Chemistry, *Proceedings of the Eurosensors XXIII conference, (Lausanne, Switzerland), vol. 1, 1, pp. 568-571, September 2009.*

- **Conference Paper:** A. J. Gallant, A. J. Baragwanath, G. P. Swift, D. Wood, and J. M. Chamberlain, "Micromachined terahertz waveguides with embedded metal rods", in *33rd international conference on infrared, millimeter and terahertz waves, (Pasadena, CA), DOI: 10.1109/ICIMW.2008.4665466, September 2008.*

- **Conference Poster:** O. A. H. Jones, A. J. Baragwanath, and G. P. Swift, "Lighting Up Metabolomics: The Use of Terahertz Lasers For The Analysis of Polluted Soils", in *2nd Australasian Symposium on Metabolomics, (Melbourne, Australia), September 2010*.

## Presentations

Invited Talks:

- A. J. Baragwanath, "Sensing the properties of biomolecules on ultrafast timescales", Rank Prize Funds Symposium on Ultrafast Biophotonics, Grasmere, UK, August 2010.
- A. J. Baragwanath, "Terahertz Plasmonic Devices", Invited Talk, Institute of High Frequency and Quantum Electronics (HQE), Siegen, Germany, April 2011.

## Awards

Department of Physics:

- 2011 Graham Russell Prize for Applied Physics.

School of Engineering and Computing Sciences:

- Best Abstract, Research Day 2011.

# Chapter 1

# Introduction

Terahertz (THz) radiation is situated between the electrical and optical realms of the electromagnetic (EM) spectrum. Typically taken to reside between 300 GHz and 10 THz, the so called 'THz gap' has remained relatively unexplored compared to its microwave and infrared counterparts, largely due to a lack of coherent sources [1].

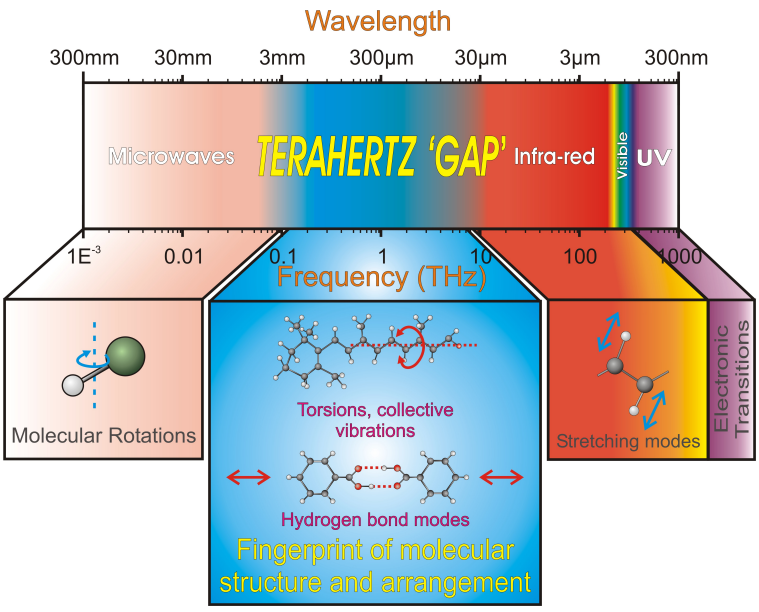


Figure 1.1: The electromagnetic spectrum, highlighting the THz region and the structural modes associated with this frequency range.

Recent years have seen an explosion of interest in the THz region, where academia and industry alike, seek to harness the innate properties of this non-ionising radiation.

The low photon energies associated with THz radiation (1 THz $\equiv$ 4.1 meV) correspond to the thermal energy associated with a range of biological processes, providing a direct probe to explore a range of complex mechanisms, including conformational changes in protein structures [2, 3]. THz radiation has been employed to interrogate the intra- and inter-molecular vibrational dynamics of a variety of structures including DNA [4, 5], chiral compounds [6], saccharides [7] and protein hydration shells [8–12].

The advent of terahertz time-domain spectroscopy (THz-TDS) [13–15] enabled the generation and detection of single cycle THz pulses, providing a broadband, albeit low intensity, THz source. THz-TDS has been used extensively as an aid to investigate the hydration dynamics and structure of liquid water and polar solvents [16–28], whilst characteristic THz 'fingerprints' have been used to identify illicit drugs and explosives [29, 30] for security applications. By utilising the 'radar-like' [31] temporal domain of THz-TDS, a range of non-destructive testing applications have been explored, including artwork [32], aircraft composites [33] as well as potential biomedical applications [34].

Besides the vast amount of chemical, biological and materials research conducted using terahertz radiation, recent years have seen rising interest in a classification of EM surface wave known as surface plasmon polaritons (SPPs). SPPs exist at the interface between a metal and a dielectric, and have been studied in great depth since the 1970's [35, 36]. Interest in SPPs remained steady, until the (re)discovery of extraordinary optical transmission (EOT) in 1998 [37] sparked a renewed interest in the topic. Recent theoretical work investigating the properties of materials decorated with sub-wavelength features [38] predicts the existence of 'spoof' SPPs, providing vast possibilities, especially in the THz region. As clean room microfabrication techniques allow structures to be fabricated with dimensions commensurate with the wavelength scales of THz radiation (1 THz $\equiv$ 300 $\mu$m) with relative ease, a great deal of this interest has focussed on the THz region. By combining existing microfabrication techniques with advancing THz technologies, SPPs have been observed, probed and exploited at THz frequencies [39, 40]. A variety of po-

tential applications have been demonstrated, including biological [41] and dielectric film sensing [42], guiding of THz radiation [43] and as an aid for THz imaging [44]. Whilst the underlying physics surrounding THz SPPs is still contested in the literature, the true potential of this relatively immature technology has yet to be fully realised.

## 1.1 Structure of this Thesis

The work presented in this thesis utilises existing microfabrication techniques to provide engineering solutions to problems associated with THz applications. Chapter 2 provides an introduction to coherent terahertz sources and detectors, focussing on the THz-TDS technique employed for the majority of THz studies documented in this thesis. Data extraction techniques are also detailed, demonstrating how dielectric information can be extracted from the time-domain pulses obtained using THz-TDS.

Chapter 3 documents the design, fabrication and testing of a microfluidic device for use in a THz-TDS arrangement. This device seeks to provide a direct solution to the strong water absorptions experienced when analysing aqueous samples in the THz region. A range of samples were analysed, including primary alcohol-water mixtures, commercial whiskies and aqueous biological solutions.

A background to the underlying physics surrounding surface plasmons is presented in chapter 4. This begins with an introduction to optical plasmons, and progresses to discuss the nature of both 'spoof' and THz frequency plasmons. The detailed analysis seeks to provide clarity to otherwise incoherent literature, where boundaries between 'spoof' and 'real' plasmons, and 'metamaterial' and 'sub-wavelength structured materials', are currently lacking. The phenomenon of extraordinary optical transmission through two-dimensional arrays of sub-wavelength apertures is analysed in detail, concluding with a literature review of THz studies investigating this effect.

Chapter 5 documents the design and fabrication of plasmonic apertures for use in THz

near-field imaging. These structures exploit surface plasmons, using them to increase transmission through sub-wavelength apertures. This technique ultimately allows the use of smaller apertures, increasing spatial resolution for THz imaging applications. The first demonstration of THz imaging using a quantum cascade laser (QCL) source and a plasmonic aperture is presented, where an inhomogeneous mixture of an amorphous pharmaceutical polymer coating and a crystalline drug material was imaged.

Systematic investigations into EOT forms the basis of chapter 6. A novel microfabrication method using electroformed copper, enabled bulk fabrication of two-dimensional sub-wavelength aperture arrays. The free standing nature of the array produced dramatically improved transmission efficiencies. An investigation into the combined effects of changing aperture area, length, width, aspect ratio and orientation, led to the development of a time-of-flight model to describe the transmission properties of these structures. This qualitative model ultimately allows sharp resonances to be engineered in the frequency domain for sensor applications. A 'hybrid' plasmonic device is also presented, demonstrating exceptionally high transmission efficiencies.

Chapter 7 draws together the work presented in chapters 3 and 6. The design, fabrication and demonstration of a microfluidic device featuring an embedded plasmonic sensor is documented. Two potential design avenues are presented, with the chosen device featuring a suspended copper aperture array embedded within a silicon cavity. A proof of principle experiment investigating IPA-$H_2O$ mixtures demonstrates the sensitivity of the device.

The thesis is concluded in chapter 8, where a variety of suggestions for future research directions are proposed.

# Chapter 2

# Background Theory and Experimental Methods

The majority of the experiments presented in this thesis have been conducted using a terahertz time-domain spectroscopy (THz-TDS) arrangement. Since the first demonstration of the technique for experimental measurements in 1989 [45], THz-TDS has become commonplace in laboratories around the world, both as an objective of research for continued system development, and as a characterisation tool for the terahertz region. This chapter will give an introduction to THz-TDS, detailing the background physics surrounding its operation. The following section will present the variety of techniques commonly used to both generate, and detect terahertz radiation. An overview of the THz-TDS system at Durham University will be given, followed by an account of the continued system development undertaken as part of this PhD. The final section of this chapter documents the data extraction techniques adopted in this thesis, where a Nelder-Mead search algorithm has been implemented for reliable and accurate extraction of dielectric information.

## 2.1 Terahertz Sources

The apparent 'terahertz gap' which exists between the electrical and optical realms of the electromagnetic spectrum has, in recent years, been bridged by the development of a variety of novel sources [1]. Approaching the problem from an electrical perspective has led to continued development of Gunn [46] and Schottky diodes [47], which when used in conjunction with multiplier devices, provide a reasonable source of terahertz radiation. Conversely, by approaching the 'gap' from the optical region, terahertz quantum cascade lasers (THz QCL), which provide a high power, spectrally pure terahertz beam, have been developed [48]. QCLs exploit molecular beam epitaxy (MBE) techniques to create periodic semiconductor quantum structures, in which population inversions can be engineered between sub-bands. After undergoing a successful intersub-band transition (leading to photon emission), the electrons tunnel through to the next period, where the same process is repeated. Cryogenic temperatures are inevitably required to ensure the intersub-band transitions are not overwhelmed by interband transitions, which are readily excited at room temperatures. Current research looks to lower the output frequency [49] and increase the operating temperatures of these devices [50], whilst others have sought to fabricate two colour sources [51].

Further terahertz sources include free electron lasers, which produce extremely high power THz output from synchrotron beams. Molecular gas lasers (e.g. $CO_2$ lasers) operate at the high frequency end of the terahertz window [52] ($\approx$ 28 THz), whilst backward wave oscillators are reliable sources for imaging at the lower end of the region [53, 54]. One final class of terahertz source utilise opto-electronic effects. Numerous sources utilise non-linear frequency mixing, which relies on optical rectification. Photoconductive sources, the emitters commonly used for THz-TDS, will be discussed in the following section.

### 2.1.1 Photoconductive Antennas

Photoconductive antennas, which rely on the optical excitation of semiconductor sources to produce a pulse of EM radiation, were first demonstrated by Auston et al. in 1984. A photoconductive emitter consists of two gold electrodes evaporated on the surface of a semiconductor substrate (typically GaAs). Electrode designs typically feature a bow-tie arrangement (fig. 2.1) to provide field enhancements and improve emission [55].

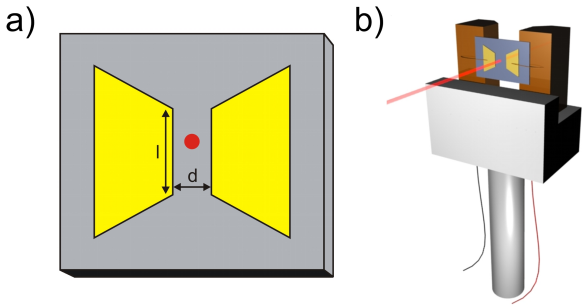


Figure 2.1: a) Diagram of a typical photoconductive emitter. The length of the bow-tie, l, is typically of the order of 3 mm, whilst the electrode separation, d, is of the order of 200 $\mu$m. b) Diagram of the emitter mount featuring two copper heat sinks. The red circle corresponds to the focussed laser beam.

Ultra-fast laser pulses, whose photon energy is greater than the band-gap of the semiconductor, are focussed between a pair of biased electrodes, producing electron hole pairs. The external bias field accelerates the electrons and holes towards their respective electrodes, establishing a changing dipole moment, which in turn, radiates a pulse of EM radiation. The electric field from a photoconductive antenna is proportional to the time derivative of the photocurrent density, $\overline{J}$, and can be described as [56]:

$$\overline{E}_{THz} \propto \frac{\partial \overline{J}}{\partial t} \tag{2.1}$$

where the photocurrent density, $\overline{J}$, can be expressed by:

$$\overline{J} = en\overline{v} \tag{2.2}$$

where $e$ is the carrier charge, $n$ is the carrier density and $\overline{v}$ is the relative velocity between the electrons and holes. The electric field of the radiated pulse can be described by the following relationship [56]:

$$\overline{E}_{THz} \propto en\frac{\partial \overline{v}}{\partial t} + e\overline{v}\frac{\partial n}{\partial t} \tag{2.3}$$

The first term on the right hand side of equation 2.3 demonstrates how the emitted radiation is proportional to the acceleration of the charge carriers under the bias field, whilst the second term demonstrates a proportionality to the change in carrier density. Ultra-short laser pulses ensure a rapid change in carrier density, whilst large bias fields between the electrodes, combined with high carrier mobilities, ensure fast carrier acceleration. Low-temperature gallium arsenide (LT-GaAs) substrates are often favoured for terahertz emitters due to the relatively high electron mobilities, high resistivity (allowing greater bias voltages) and very short carrier lifetimes (improving the bandwidth of the emission) [57].

As the electric field of the terahertz pulse is proportional to the first derivative of the photocurrent, it features both positive and negative half cycles. The first, positive half cycle is extremely fast ($<$ 1 ps) due to the rapid increase in the photocurrent associated with the ultrafast laser pulse. The second half cycle, however, is often much slower due to carrier recombination and 'screening' of the bias field due to the uneven distribution of charge carriers. THz radiation is emitted in a direction perpendicular to the surface of the semiconductor. The radiation which passes through the substrate is undoubtedly attenuated, limiting the achievable bandwidth, however the much simpler optical arrangements associated with such emission are often preferred. Higher bandwidths can be achieved by collecting the emission from the front face of the substrate. Although a reliable source of terahertz radiation, the typical average powers produced by photoconductive sources are in the order of $\mu$W [58]. The use of coherent detection techniques, in combination with lock-in detection methods ensures exceptional signal-to-noise ratios can be achieved with these relatively inefficient sources (e.g. 600:1 in Durham THz-TDS arrangement).

## 2.2 Terahertz Detectors

Terahertz radiation is currently much easier to detect than it is to generate in a useful form. Detection can be distilled into two main categories - incoherent and coherent. Incoherent detectors measure the heating effects of the incident radiation. Whilst no phase information can be obtained by such techniques, a measure of the total radiation intensity can be acquired. Typical examples of incoherent thermal detectors are bolometers and Golay cells. Golay cells rely on the expansion of xenon gas due to heating by the incident radiation. The expansion causes a deflection in a diaphragm, the magnitude of which can be measured by either a strain gauge, or via a light sensitive detector, aligned to measure the change in reflection of an internal light source incident on the diaphragm. Cryogenic temperatures are required to use bolometers for detecting terahertz radiation. Bolometers consist of an absorbing material in thermal contact with a heat sink; impinging radiation raises the temperature of the absorber relative to the heat sink. The temperature difference is then measured using a thermocouple.

Coherent detectors take the form of either photoconductive antennas or electro-optic crystals. Photoconductive detectors work on an inverse principle to the emitters presented in section 2.1.1. Electron-hole pairs are excited in the same manner, and are subsequently accelerated between two unbiased electrodes by the electric field of the incident terahertz radiation. The resultant electric field established between the two electrodes can then be measured, giving a direct measurement of the instantaneous amplitude of the terahertz signal. The time-domain measurement technique described in section 2.3, details how this amplitude can be sampled in time. Detection, in a similar way to emission, relies on the properties of the semiconductor substrate, specifically the charge carrier density, the recombination lifetime of the carriers and the amplitude of the incident terahertz field. Often, slightly broader temporal pulses are detected using photoconductive detectors due to the finite carrier lifetimes, leading to the loss of higher frequency components [59]. However, frequencies in excess of 20 THz have been detected using LT-GaAs detectors

[60]. A combination of photoconductive emission and electro-optic detection is used for the THz-TDS arrangement in Durham.

### 2.2.1 Electro-optic Detection

The Pockels effect is a linear electro-optic effect, where birefringence is induced in an optical medium by the application of an external electric field. The magnitude of the observed birefringence is directly proportional to the incident electric field. Birefringence occurs in anisotropic crystalline materials, affecting the speed at which orthogonal polarisations traverse the crystal. For light incident perpendicular to both the optical axis and the crystal face, orthogonal polarisations will experience unequal indices of refraction, causing a retardation of one polarisation with respect to the other. Each polarisation inevitably emerges at different times, incurring a phase difference, the magnitude of which depends on the crystal thickness and the wavelength of the incident radiation. Quarter wave plates are based on this principle, where a $\pi/2$ phase shift is introduced, changing the polarisation of a beam from plane to circular.

For the case of terahertz detection, ZnTe is most commonly used as an electro-optic crystal. A probe laser beam passes through a ZnTe crystal, a quarter wave plate and finally through a Wollaston prism. The quarter wave plate changes the laser beam from plane polarised to circularly polarised, whilst the Wollaston prism separates the orthogonal polarisation states, which are subsequently focussed onto a pair of balanced photodiodes. With no incident terahertz field, the plane polarised laser beam passes through the crystal unaffected. The circularly polarised beam which exits the quarter wave plate is split into two equal orthogonal components by the Wollaston prism, leading to a zero reading on the balanced detector. When a terahertz field is incident upon the crystal however, the crystal exhibits birefringence, leading to an elliptically polarised beam exiting the crystal. The plane of polarisation of the beam is altered by the quarter wave plate, though the elliptical nature still remains. The Wollaston prism splits the orthogonal polarisation states,

creating two beams of unequal intensities. This creates an inbalance between the pair of photodiodes, allowing a current to be detected.

As the length of the terahertz pulse is much greater than that of the probe laser beam, the detected current serves as an instantaneous direct measurement of the refractive index of the ZnTe crystal. The measurement of the refractive index is a direct, instantaneous effect of the birefringence of the crystal. Furthermore, as the birefringence is a consequence of the Pockels effect, it is directly proportional to the incident electric field. Thus, the current measured between the photodiodes is directly proportional to the instantaneous electric field of the incident terahertz pulse. By gating the delay of the probe beam with respect to the terahertz beam, one can map the electric field of the incident terahertz pulse as a function of time.

## 2.3 THz Time-Domain Spectroscopy

Pioneered by Daniel Grischkowsky and co-workers in the late 1980s, terahertz time-domain spectroscopy has rapidly become a valuable analysis tool in both chemistry and physics laboratories. The time-domain nature of the technique allows terahertz frequency interactions to be probed on a picosecond timescale. The combination of the spectroscopic information with the temporal nature of the measurements, provides an extremely powerful technique, suited to both academic research and non-destructive industrial testing alike. The nature of the technique utilises a femtosecond (fs) laser pulse for both generation and detection of the terahertz radiation. Generation and detection is achieved using either photoconductive devices, or electro-optic crystals as described above.

The technique relies upon two optical paths, the pump and the probe, split from the same fs laser source. The pump beam is used to generate the free space terahertz radiation, which is collimated and focussed using a series of off-axis parabolic mirrors. The beam is transmitted through, or reflected off a sample of interest, after which the beam

is re-collimated and focussed onto the detector. The probe beam is co-focussed onto the detector, and, in the case of electro-optic detection, onto the balanced photodiodes. Fundamentally, the technique hinges upon the relative path lengths of the pump and the probe beams. When the path lengths are equal, only terahertz pulses created by the same part of the laser beam as that incident on the detector can be detected. By inserting an automated translation stage in either beam arm, one beam can be delayed with respect to the other. By scanning through the point of equal path lengths, the electric field of the terahertz radiation can be recorded as a function of time (stage position), with a time resolution limited by the step size of the stage. The low power of the terahertz pulses generated using photoconductive switches requires lock-in amplification for reliable detection. By placing either an optical chopper in the pump beam, or electrically chopping the emitter bias, a reference frequency can be provided for the lock-in detector, vastly increasing the signal-to-noise. Measurements are taken by firstly recording a reference scan of free space, with no sample inserted. With the sample present, a further scan is taken where a modified pulse will be obtained. With knowledge of how electromagnetic radiation interacts with the sample, dielectric information can be extracted, as discussed in section 2.4.

### 2.3.1 Durham THz-TDS arrangement

The THz-TDS system at Durham has been continually developed since its introduction in 2004. At the heart of the system lies a Ti:Sapphire laser (Coherent Inc.), with a central wavelength of 790 nm, 45 nm bandwidth, 20 fs Gaussian pulse, 76 MHz repetition rate and 450 mW average pulse power. Four, two-inch, 90° off-axis parabolics are used for the terahertz collection optics, typically collecting the radiation emitted through the GaAs emitter. The optical layout for the system can be seen in figure 2.2.

Over the course of this PhD, continued system development has focussed on three main areas: improving signal-to-noise, development of rapid terahertz imaging using a fast

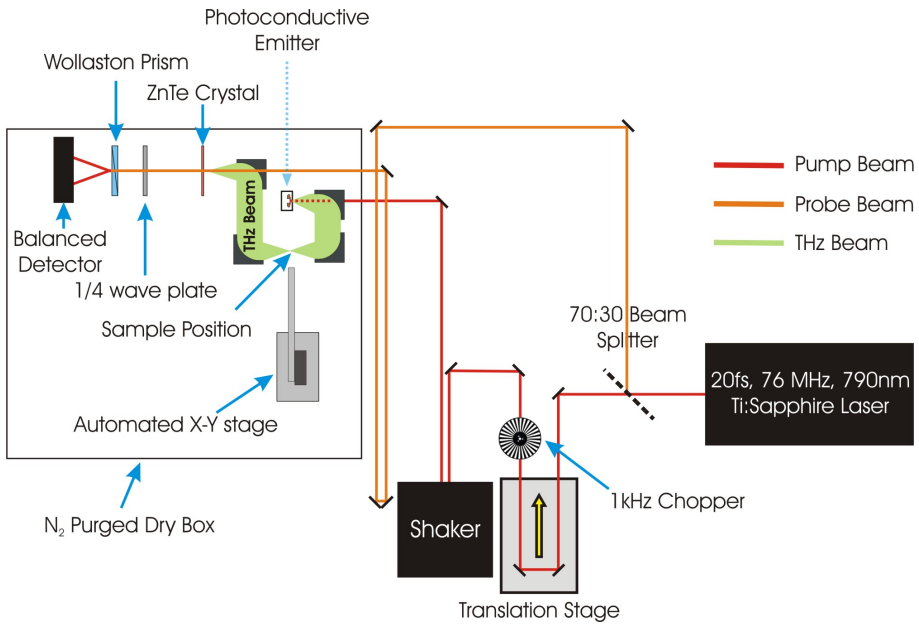


Figure 2.2: Typical optical arrangement for the THz-TDS system at Durham.

optical delay line, and the design of a new dry box to aid in the removal of atmospheric water vapour. Upon arrival, a typical signal-to-noise ratio (SNR) with the TDS system was in the order of 100:1. Improving the SNR has been achieved through many small, individual steps. Firstly, the purchase of a new balanced photo-detector (Thorlabs PDB 150A) with increased gain provided distinct benefits for signal detection. The fabrication of emitters on a variety of GaAs samples has shown a marked increase in achievable signal. The move away from photoconductive detectors towards electro-optic detection provided the most dramatic increase in signal-to-noise however. Using 0.5 mm thick ZnTe crystals, SNRs in the order of 600:1 were soon commonplace in the lab. The inclusion of a translation stage to move the ZnTe crystal through the co-focal point of the terahertz and NIR laser beams, further improved the system.

The design of a new acrylic dry box was paramount to achieving the quality of results presented in section 6.4, where well defined temporal oscillations were necessary to observe slight resonance shifts in the frequency domain. The dry box was designed such that all the generation, collection and detection optics could be placed in the purged environment, along with an automated X-Y sample stage. A series of ports were drilled through the box,

whose centres aligned not only with the tracks on the optical bench, but with the height of the laser beam also. Quartz windows could be bolted to the front of the box when ports were to be used, whilst thin acrylic plates covered those which were not required. With the windows aligning perfectly to the optical bench, further beams can be easily directed into the dry box for possible optical pump, terahertz probe experiments. Whilst the size of the dry box was on the large size, humidity readings as low as 1 % could be achieved with less than 10 minutes of purging. A three dimensional sketch of the dry box can be seen in figure 2.3, where the vast array of ports can be clearly seen.

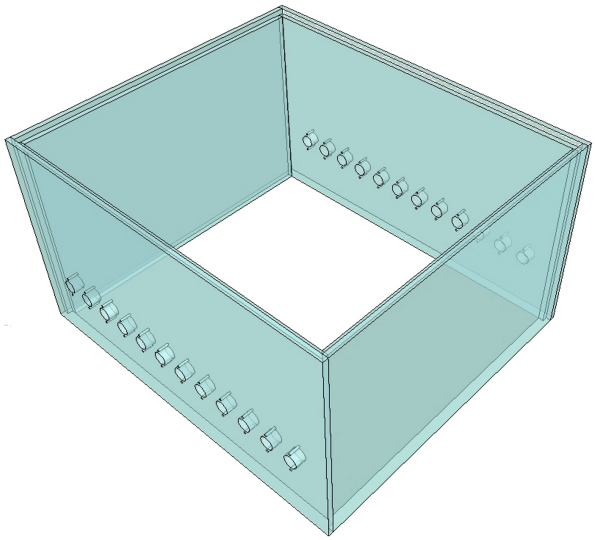

Figure 2.3: Three dimensional sketch of the final drybox design.

The inclusion of a fast optical delay line in the pump beam (APE ScanDelay 50) enabled rapid terahertz images to be acquired, in conjunction with a high precision X-Y translation stage arrangement (Newport MFA-CC). Alignment of the delay stage in the system was achieved via the design and fabrication of an aluminium mount which ensured the trigonal mirror arrangement reflected a beam parallel to the optical bench. Signal acquisition was achieved through the use of an oscilloscope (Agilent DSO 6052A) in conjunction with a lock-in amplifier (SRS SR830DSP). After running a standard terahertz scan, the translation stage was moved to the point of maximum signal. The fast optical delay line would then be set to oscillate, with an amplitude and frequency governed by the module

specific control options. By connecting the output of the lock-in to the input of the oscilloscope, and triggering from the oscillation frequency of the shaker, terahertz pulses could be acquired in $\approx 3$ seconds, as opposed to the minutes usually required. A LabView script was written to control and acquire data from the oscilloscope, allowing manual entry of the shaker settings to convert the module specific frequency and amplitude units into a ps time-domain measurement. A further LabView script was written to enable rapid raster scanning of the X-Y stages, acquiring an oscilloscope data set at each point. Finally, a simple MATLAB routine was written to analyse each data set, allowing 2D intensity plots to be created, based on either pulse position or magnitude. A typical example of a terahertz image acquired using the system can be observed in figure 2.4.

Figure 2.4: The image on the left shows a photograph of a leaf with a small THz image superimposed on top. The image on the right is a large area THz image of a different leaf, where the vein structure can be clearly seen.

## 2.4 Data Extraction

When undertaking THz-TDS measurements, a waveform acquired from passing a terahertz pulse through a sample of interest, is directly compared to a free space reference. A sample waveform differs in two ways from the reference - it is shifted later in time

due to the refractive index of the sample, whilst absorptions in the sample and Fresnel reflections at each interface reduce its magnitude. As a single terahertz pulse contains a broad spectrum of frequencies, a sample can be spectrally interrogated in a single scan. The mathematical process of Fourier transforming converts the temporal waveforms into individual frequency components, giving both amplitude and phase information. Frequency dependent data relating to the optical properties of the sample can then be extracted for the whole of the available spectrum. To begin the process of data extraction, we first consider an electromagnetic plane wave of frequency $\omega$ propagating in the $z$ direction through a medium with complex refractive index given by $\hat{n} = n + i\kappa$:

$$E(z,t) = E_0 \exp\left\{i(\omega t + \frac{\hat{n}\omega}{c}z)\right\} \tag{2.4}$$

where $n$, the real part of the refractive index, concerns the phase speed, and $\kappa$, the extinction coefficient, is a term which indicates the absorptions incurred in the material. This equation can be distilled into an oscillatory time dependent term, representing the wave propagation, and an exponential decay term, representing absorption in the sample:

$$E(z,t) = E_0(t) \exp\left\{i\frac{n\omega}{c}z\right\} \exp\left\{-\frac{\kappa\omega}{c}z\right\} \tag{2.5}$$

where the time dependent term, $E_0(t) = E_0 \exp(i\omega t)$, represents the wave propagating in free space before entering the absorbing medium. This equation can be equally represented in the frequency domain, where the frequency dependent electric field for both a reference wave ($n = 1$, $\kappa = 0$), and a wave passing through a medium of thickness $d$ are given by:

$$E_{ref}(\omega) = E_0(\omega) \exp\left\{i\frac{\omega}{c}d\right\} \tag{2.6a}$$

$$E(\omega) = E_0(\omega) \exp\left\{i\frac{n(\omega)\omega}{c}d\right\} \exp\left\{-\frac{\kappa(\omega)\omega}{c}d\right\} \tag{2.6b}$$

Equation 2.6b takes into account the absorptions incurred due to propagation through the sample, but fails to detail any losses associated with Fresnel reflections from each air-sample boundary. At each boundary, the fraction of the wave transmitted can be expressed as:

$$T_{1\to 2} = \frac{2n_1}{n_1 + n_2} \tag{2.7}$$

For the case of a wave passing through an air-sample-air medium, two such losses, namely $T_{air\to sam}$ and $T_{sam\to air}$ exist, giving a complete attenuation of:

$$T_{tot} = \frac{4n(\omega)}{(n(\omega)+1)^2} \tag{2.8}$$

An equation detailing the full attenuation experienced by a plane wave propagating through an absorbing sample of thickness $d$ can now be given:

$$E_{sam}(\omega) = E_0(\omega)\frac{4n(\omega)}{(n(\omega)+1)^2}\exp\left\{i\frac{n(\omega)\omega}{c}d\right\}\exp\left\{-\frac{\kappa(\omega)\omega}{c}d\right\} \tag{2.9}$$

By dividing equation 2.9 by equation 2.6a, a theoretical transfer function can be derived:

$$\frac{E_{sam}}{E_{ref}} = \frac{4n(\omega)}{(n(\omega)+1)^2}\exp\left\{-\frac{\kappa(\omega)\omega}{c}d\right\}\exp\left\{i\frac{\omega d}{c}(n(\omega)-1)\right\} \equiv R + iI \tag{2.10}$$

The complex phase, $\varphi = \arctan(I/R)$, and amplitude, $A = \sqrt{R^2 + I^2}$, of this ratio can be used to calculate the frequency dependent refractive index and extinction coefficient respectively [61]:

$$n(\omega) = 1 + \frac{c}{\omega d}\varphi \tag{2.11a}$$

$$\kappa(\omega) = -\frac{c}{\omega d}\ln\left(\frac{(n(\omega)+1)^2}{4n(\omega)}A\right) \tag{2.11b}$$

Other related expressions, namely the absorption coefficient, $\alpha$, and the real and imaginary parts of the dielectric constants, $\epsilon'$ and $\epsilon''$, can be extracted through the following

relations:

$$\alpha(\omega) = \frac{2\kappa(\omega)\omega}{c} \tag{2.12a}$$

$$\epsilon' = n^2 - \kappa^2 \tag{2.12b}$$

$$\epsilon'' = 2n\kappa \tag{2.12c}$$

### 2.4.1 Fabry-Pérot Considerations

When dealing with multi-layered structures, the Fresnel reflections which occur at each material boundary must be taken into account if accurate dielectric properties are to be extracted from the time-domain data. Furthermore, when dealing with layers with comparable dimensions to the wavelength of the radiation, the added complexity of cavity reflections must also be accounted for. Considering the microfluidic device presented in this thesis (chapter 3), Fabry-Pérot oscillations occur in both the cavity, and each silicon wafer. A theoretical transfer function for a multi-layered structure will be presented below, taking into account the Fresnel reflections at each material boundary, along with the Fabry-Pérot oscillation in the cavity. The Fabry-Pérot effects which occur in the silicon wafers can be ignored due to the high refractive index of silicon at terahertz frequencies ($\approx 3.42$) which delays reflections sufficiently in time. Such a detailed derivation is often overlooked in work on this subject [62], however correct transfer functions have been derived for similar scenarios [63–65].

The derivation below will take into account the first three transmission orders, as depicted in figure 2.5. As an approximation, higher orders can be assumed to be extinguished from compound Fresnel reflections at each silicon-air interface. To begin the derivation, we consider the case of an incident terahertz pulse of amplitude $E_i$, propagating through an air-filled (empty) cavity of thickness $d$, as would be taken for a reference measurement when using the device:

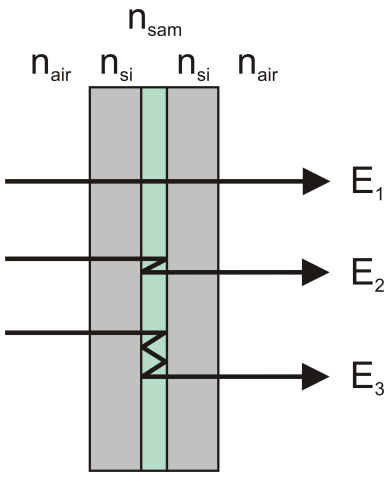


Figure 2.5: The first three transmission orders considered for the Fabry-Pérot term in the data extraction.

$$E_{ref_1}(\omega) = E_i t_{a,si} t_{si,a} t_{a,si} t_{si,a} \exp\left(\frac{id\omega}{c}\right) = E_i t_{a,si}^2 t_{si,a}^2 \exp\left(\frac{id\omega}{c}\right) \tag{2.13a}$$

$$\begin{aligned} E_{ref_2}(\omega) &= E_i t_{a,si}^2 t_{si,a}^2 r_{a,si}^2 \exp\left(\frac{id\omega}{c}\right) \exp\left(\frac{2id\omega}{c}\right) \\ &= E_i t_{a,si}^2 t_{si,a}^2 r_{a,si}^2 \exp\left(\frac{id\omega}{c}\right) \exp\left(i\delta\right) \end{aligned} \tag{2.13b}$$

$$\begin{aligned} E_{ref_3}(\omega) &= E_i t_{a,si}^2 t_{si,a}^2 r_{a,si}^4 \exp\left(\frac{id\omega}{c}\right) \exp\left(\frac{2id\omega}{c}\right) \exp\left(\frac{2id\omega}{c}\right) \\ &= E_i t_{a,si}^2 t_{si,a}^2 r_{a,si}^4 \exp\left(\frac{id\omega}{c}\right) \exp\left(2i\delta\right) \end{aligned} \tag{2.13c}$$

Here, $t_{a,si}$ ($=t_{si,a}$) and $r_{a,si}$ represent the Fresnel transmission and reflection coefficients for radiation incident upon an air-silicon (silicon-air) boundary:

$$t_{a,si} = t_{si,a} = \frac{4 n_{air} n_{si}}{(n_{air} + n_{si})^2} \tag{2.14a}$$

$$r_{a,si} = \left(\frac{n_{air} - n_{si}}{n_{air} + n_{si}}\right)^2 \tag{2.14b}$$

The reference transmission coefficient $E_{ref}$ can be calculated by summing the transmission

orders presented in equation 2.13:

$$E_{ref}(\omega) = E_{ref_1}(\omega) + E_{ref_2}(\omega) + E_{ref_3}(\omega) + \ldots \tag{2.15a}$$

$$= E_i t_{a,si}^2 t_{si,a}^2 \exp\left(\frac{i d\omega}{c}\right)\left(1 + r_{a,si}^2 \exp(i\delta) + r_{a,si}^4 \exp(2i\delta) + \ldots\right) \tag{2.15b}$$

$$= E_i t_{a,si}^2 t_{si,a}^2 \exp\left(\frac{i d\omega}{c}\right) \sum_{k=0}^{\infty} \left(r_{a,si}^2 \exp(i\delta)\right)^k \tag{2.15c}$$

$$= E_i t_{a,si}^2 t_{si,a}^2 \exp\left(\frac{i d\omega}{c}\right) \frac{1}{1 - r_{a,si}^2 \exp\left(\frac{2i d\omega}{c}\right)} \tag{2.15d}$$

where the following identity has been implemented between equations 2.15c and 2.15d:

$$\sum_{k=0}^{\infty} a r^k = \frac{a}{1-r} \tag{2.16a}$$

$$\Rightarrow \sum_{k=0}^{\infty} \left(r_{a,si}^2 \exp i\delta\right)^k = \frac{1}{1 - r_{a,si}^2 \exp i\delta} \tag{2.16b}$$

Similarly, an equivalent equation can be derived for the case when the cavity is filled with a sample of refractive index $\tilde{n}(\omega)$. This changes the Fresnel equations, resulting in $t_{sam,si}$ and $r_{sam,si}$ for the transmission and reflection coefficients respectively:

$$E_{sam}(\omega) = E_i t_{a,si} t_{si,sam} t_{sam,si} t_{si,a} \exp\left(\frac{i\tilde{n}_{sam}(\omega) d\omega}{c}\right) \frac{1}{1 - r_{sam,si}^2 \exp\left(\frac{2i\tilde{n}_{sam}(\omega) d\omega}{c}\right)} \tag{2.17}$$

By dividing equation 2.17 by equation 2.15d, the theoretical transfer function is derived:

$$\frac{E_{sam}(\omega)}{E_{ref}(\omega)} = \frac{\dfrac{E_i t_{a,si} t_{si,sam} t_{sam,si} t_{si,a} \exp\left(\dfrac{i\tilde{n}_{sam}(\omega)d\omega}{c}\right)}{1 - r_{sam,si}^2 \exp\left(\dfrac{2i\tilde{n}_{sam}(\omega)d\omega}{c}\right)}}{\dfrac{E_i t_{a,si}^2 t_{si,a}^2 \exp\left(\dfrac{id\omega}{c}\right)}{1 - r_{a,si}^2 \exp\left(\dfrac{2id\omega}{c}\right)}} \tag{2.18a}$$

$$= \exp\left(\frac{il\omega}{c}\left(\tilde{n}_{sam}(\omega) - 1\right)\right) \frac{t_{si,sam}^2}{t_{a,si}^2} \frac{1 - r_{a,si}^2 \exp\left(\dfrac{2id\omega}{c}\right)}{1 - r_{sam,si}^2 \exp\left(\dfrac{2i\tilde{n}_{sam}(\omega)d\omega}{c}\right)} \tag{2.18b}$$

Expressing this in terms of refractive indices yields:

$$\frac{E_{sam}(\omega)}{E_{ref}(\omega)} = \underbrace{\exp\left(\frac{id\omega}{c}\left(\tilde{n}_{sam}(\omega) - 1\right)\right)}_{\text{Phase term}} \underbrace{\frac{\tilde{n}_{sam}(\omega)\left(n_{si}+1\right)^2}{\left(\tilde{n}_{sam}(\omega) + n_{si}\right)^2}}_{\text{Fresnel term}} \underbrace{\frac{1 - \left(\dfrac{1-n_{si}}{n_{si}+1}\right)^2 \exp\left(\dfrac{2id\omega}{c}\right)}{1 - \left(\dfrac{\tilde{n}_{sam}(\omega) - n_{si}}{\tilde{n}_{sam}(\omega) + n_{si}}\right)^2 \exp\left(\dfrac{2i\tilde{n}_{sam}(\omega)d\omega}{c}\right)}}_{\text{Fabry-Pérot term}} \tag{2.19}$$

The theoretical transfer function shown above should be used instead of equation 2.10 presented earlier, to extract refractive index or dielectric constant information as a function of frequency. To a first approximation, the detailed transfer function in equation 2.19 acts as an acceptable data extraction technique. For more accurate values, one has to consider the acquisition of phase through the sample. The sub-wavelength optical path lengths encountered with the microfluidic device mean that the phase acquired as the radiation passes through the sample is comparable to the phase change at each material boundary. In such instances, data extraction search algorithms are required for reliable and accurate data extraction, as detailed in the following section.

### 2.4.2 Nelder-Mead Algorithm

Reliable and accurate data extraction from THz-TDS results have been presented in the literature for a variety of samples. The work of Duvillaret et al. was the first to address the problem, where an adaptation of a Newton-Raphson method was demonstrated for both optically thick and thin samples [66]. This was further developed to allow for the extraction of the sample thickness [67]. Other works on this topic have provided alternative algorithms, for example the total variation technique [68,69], whilst others have developed routines for specific samples, including thin metal films [70], glasses [71] and sub-100-$\mu$m samples [72]. The removal of unwanted reflections and etalon effects in the time-domain is also of continued interest [73].

The algorithm implemented in this thesis adopts a Nelder-Mead search approach, initially demonstrated [74], and further developed [75] by Martin Koch and colleagues. This technique allows for the analysis of thin, low index materials, and can be implemented using a variety of functions in the commercial package MATLAB. The method proceeds in the same manner as previously explained, where the ratio of the recorded reference and sample pulses gives an experimental transfer function. Fundamentally, an accurate value of $\tilde{n}_{sam}(\omega) = n_{sam}(\omega) + i\kappa(\omega)$ is extracted at each individual frequency when the difference between the theoretical and experimental transfer functions is a minimum. A measure of this difference is defined by the following error functions [74]:

$$M(\omega) = |H_{theory}(\omega)| - |H_{exp}(\omega)| \tag{2.20a}$$

$$A(\omega) = \angle H_{theory}(\omega) - \angle H_{exp}(\omega) \tag{2.20b}$$

$$Err = \sum_{\omega} (|M(\omega)| + |A(\omega)|) \tag{2.20c}$$

The error function $Err$ is minimised with respect to $n_{sam}(\omega)$ and $\kappa(\omega)$ for each

individual frequency $\omega$, using a Nelder-Mead search via the 'fminsearch' built in algorithm in MATLAB. The implementation of the algorithm is much simpler than that demonstrated in [74] due to the fact the thickness of our sample is measured to a high degree of accuracy prior to the time-domain measurements. This negates the need for error bound analysis in relation to the estimation of sample thickness from the TDS results alone. Starting points for the search algorithm are calculated by the simple equations detailed in section 2.4. Pairs of values of $n_{sam}(\omega)$ and $\kappa(\omega)$ are then cycled through to find the minimum value of $Err$ at each individual frequency. Once a minimum value is arrived at, $n_{sam}(\omega)$ and $\kappa(\omega)$ can be plotted for the entire broadband spectrum interrogated with the THz-TDS technique.

# Chapter 3

# A Silicon Based Microfluidic Device

This chapter will document the design, fabrication and testing of a microfluidic device for terahertz frequencies. The use of terahertz radiation has long been hampered by strong absorptions from polar liquid samples. The permanent dipole of water dominates, and often masks any specific terahertz absorptions which may occur from a known molecule in solution. In addition, the high optical density of polar liquids throughout the terahertz regime means that with the low emitter powers used in conventional THz-TDS experiments, relatively thin samples ($<\approx 200$ $\mu$m) almost completely absorb the incident radiation. A direct solution to this problem has so far been circumvented by using reflection optical arrangements, as opposed to transmission. Reflection arrangements suffer from challenging optical alignment, complex mathematical analysis and weak signals. Given the wealth of terahertz properties predicted for many biological molecules, a more practical solution is desirable. To date, the analysis of biological samples at terahertz frequencies has mainly focussed on dehydrated [76] or single crystal samples [77]. Given that proteins require water to function, a device enabling the analysis of such molecules in their natural environment would be invaluable to the THz community.

The microfluidic device provides one possible solution to the 'water problem' which currently hampers the analysis of polar liquids and aqueous biological samples at terahertz frequencies. The device is constructed solely from silicon, a material inherently transparent

to terahertz radiation, and is designed for use in a standard THz-TDS system. The fundamental design characteristics of the cell focus on the importance of the knowledge of the optical path length through a sample. The microfabrication techniques detailed in section 3.2 allow this path length to be defined to a high degree of accuracy, while the microfluidic design aspect keeps this path length to a minimum. The short optical path length balances sufficient sample interaction with strong signal transmission. Section 3.3 demonstrates the sensitivity of the device through a range of THz-TDS experiments, including the analysis of primary alcohols, commercial whiskies, and simple biological molecules in solution.

## 3.1 Microfluidics for Terahertz Frequencies

The large optical density of water and other polar liquids at terahertz frequencies has resulted in the development of many novel devices which aim to minimise the optical path length through the sample. Previous work on hydrated proteins [78] utilised a brass cell with terahertz transparent quartz windows to contain samples. Here, a Teflon spacer was used to separate the brass plates by a distance of $\approx 250$ $\mu$m. This device suffers from the fact that samples cannot be interchanged within quick succession, and the optical path length cannot be determined to a high degree of accuracy. Other work on proteins involved encapsulating samples in a polyethylene bag, sandwiched between two methylpentene copolymer windows [10]. This approach is beneficial in that the distance between the two polymer windows can be altered, thus varying the optical path length. However, it suffers from many drawbacks including its cumbersome arrangement, multiple surface reflections, and the difficulties associated with interchanging samples.

To solve the problems relating to the interchanging of samples highlighted above, other groups have tried a more conventional microfluidic approach. Standard materials for microfluidic device fabrication, such as polydimethylsiloxane (PDMS), exhibit vast terahertz

absorptions due to their high water content, rendering them unsuitable. Low terahertz-loss polymers such as Zeonor 1020R have been used to create suitable devices [63]. The use of plasma polymerised tetramethyldisiloxane is another possible emerging candidate for a polymer solution [79]; however, more detailed work still needs to be undertaken into the terahertz absorption properties of the material. Silicon-glass microfluidic devices have been presented in the past [80], though they are unsuitable for terahertz frequencies due to the scattering effects induced by the glass substrate.

On first thoughts, silicon does not suggest itself as an obvious material for sole fabrication of microfluidic devices due to its opaque nature at optical frequencies. The well known fact that silicon is inherently transparent to terahertz radiation has been exploited in previous work, in which silicon plates are used to contain samples [21]; though this device once again suffers from the fact that samples cannot be easily interchanged. Commercial products are available [81], however the use of such products restricts the addition of any further functionality, such as the integration of plasmonic arrays (chapter 7), antireflective structures [82] and mixing chambers, for example. The transparent nature of the material, combined with the wealth of micromachining techniques available for silicon, makes it an ideal candidate to fabricate a terahertz microfluidic device, which allows samples to be easily interchanged.

## 3.2 Device Design and Fabrication

After selecting silicon as the fabrication material, our initial design was determined by two features: the interaction chamber must have a well defined, controllable depth, and samples must be able to be pumped through the device in turn. A simple design, incorporating input and output capillaries connected to a main chamber was chosen. The capillaries were kept narrow (200 $\mu$m), to allow capillary action to draw fluid in and out of the chamber and help reduce pumping pressures. The chamber dimensions were kept

large (1 $cm^2$) to allow for simple alignment in the terahertz beam. It was estimated a chamber depth in the region of 50 $\mu$m would provide a suitable optical path length to allow for sufficient sample interaction, while still allowing a strong terahertz signal to be detected, even with an optically dense sample. Previous reports provide calculations of the optimum thicknesses for a variety of samples to be analysed using a transmission THz-TDS arrangement: for water, a thickness of 130 $\mu$m at 0.5 THz is calculated, decreasing to 100 $\mu$m at 1.0 THz [83]. This indicates that thinner samples should be used as the frequency increases. With our broadband system, frequencies up to 3 THz are achieved, thus justifying our 50 $\mu$m chamber depth. The fabrication of the device was carried out in a cleanroom environment, utilising a range of standard lithographic techniques. The following sections document the fabrication processes used at each stage in the creation of the microfluidic device.

### 3.2.1 Sample Chamber

To fabricate the sample chamber, a 5 cm $\times$ 2.5 cm piece of 600 $\mu$m thick highly resistive silicon was oxidised in a steam environment, producing a 700 nm oxide layer. The chamber and connecting capillaries were defined in an S1813, spin coated photoresist layer (3700 rpm for 40 s, 3 s exposure, 351 developer (351, $H_2O$: 1:3)). Initially, a buffered hydrogen fluoride (HF) solution was used to etch the exposed oxide region ($[NH_4]F$, HF: 4:1). This etch had the unwanted effect of stripping the protective oxide from the reverse of the wafer, required for protection in the subsequent silicon etch. For this reason, a reactive ion etch (RIE) was used instead (Oxford Plasma Lab. 80, 40 mTorr, 200 W, 32 sccm $CHF_3$, 18 sccm Ar, 30 min, 10 °C table temp.). After stripping the photoresist, the bare silicon region defining the chamber and capillaries was ready to be etched. As detailed above, a thin uniform sample cell, with a thickness that can be defined and determined to a high degree of accuracy is necessary if accurate optical constants are to be extracted. Initially, a xenon difluoride ($XeF_2$) etch was used for its highly selective etch chemistry [84].

Analysis of the chamber after this etch showed a non-uniform etch profile, with significant edge loading effects [85], as displayed in figure 3.1.

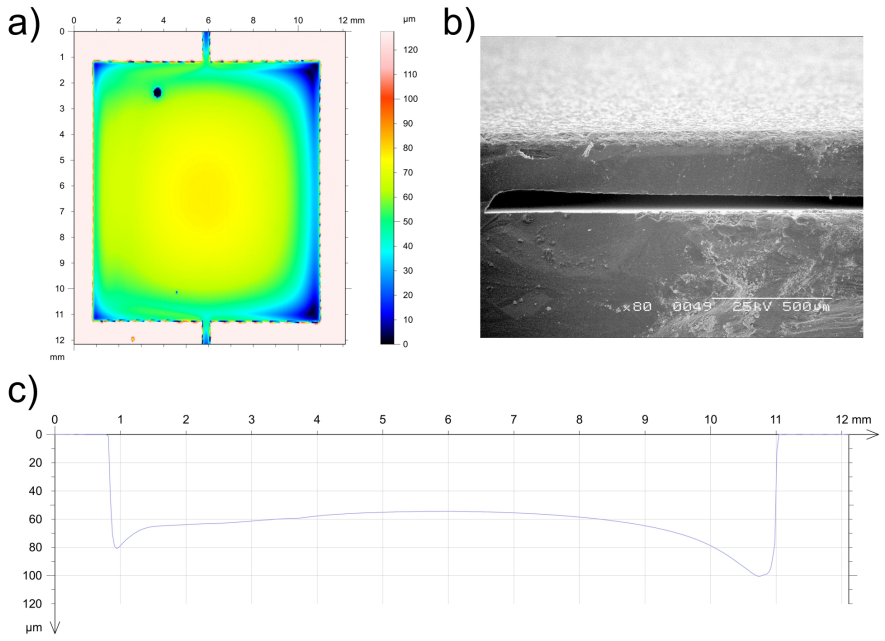


Figure 3.1: a) Surface profile of a $XeF_2$ etched chamber acquired using a STIL surface profiler. b) SEM image of sectioned $XeF_2$ bonded chamber. c) Line scan of data extracted from a) showing the non-uniformity of the etch.

For this reason, an 85 °C potassium hydroxide (KOH) etch was used instead, producing a flat, uniform chamber with a surface roughness of the order of 1 $\mu$m over the 1 $cm^2$ area (fig. 3.2). With a typical etch rate of 1 $\mu$m/min, the chamber could be etched to the desired depth with relative ease.

### 3.2.2 Fluidic Ports

Having created a uniform chamber, fluidic access ports had to be created to enable samples to be pumped through the device. After growing a further 700 nm protective oxide layer, a thicker photoresist, AZ4562, was spin coated (3700 rpm for 40s) on the unpolished side of the wafer. Circular input ports were defined using double-sided lithographic alignment techniques which, once etched, would allow access to the previously etched capillaries (18

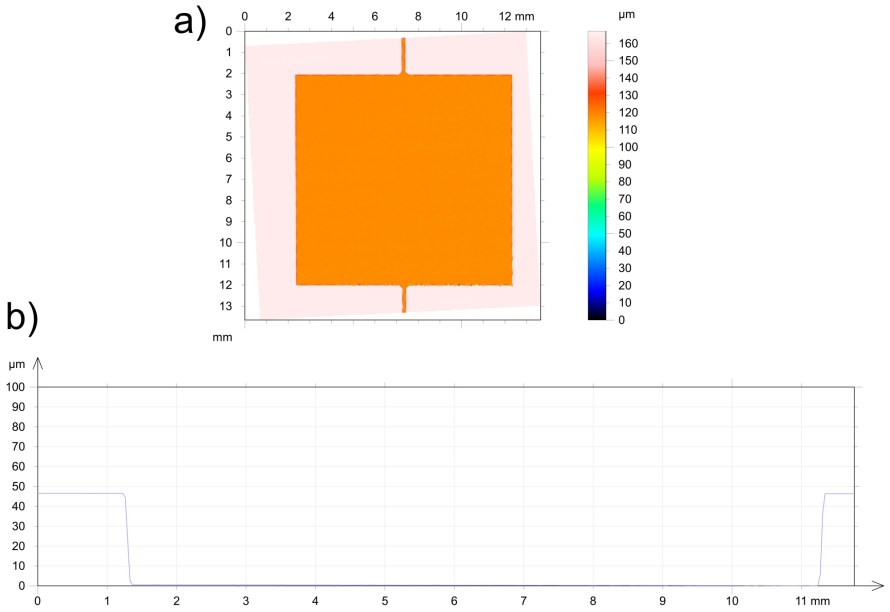


Figure 3.2: a) Surface profile of KOH etched chamber acquired using a STIL surface profiler. b) Line scan of data extracted from a) showing the uniform chamber produced by this method.

s exposure, 351 developer (351, $H_2O$: 1:3)). RIE was used to clear the exposed oxide regions as before. $XeF_2$ was used to etch the ports, chosen for its high selectivity to oxide, necessary for such a deep etch (Xactix E1, 175 cycles, 60 s/cycle, 4 Torr $XeF_2$, 4 Torr $N_2$). Before etching, the edges of the wafer were painted with PMMA to alleviate any pinhole problems. After removal of the photoresist and the remaining oxides, a device of the type shown in figure 3.3 was created.

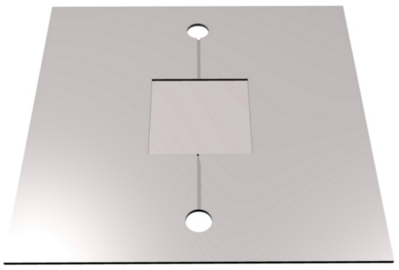

Figure 3.3: Diagram of capillaries, chamber, and ports etched into the silicon wafer.

### 3.2.3 Silicon Bonding

To create the device solely out of silicon, the technique of silicon-silicon bonding was used to seal the chamber and capillaries [86–88]. This technique negates the need for an adhesive or polymer to bond the wafers. Such substances could not only cause blockages in the capillaries, but would have introduced unwanted reflections in the terahertz temporal waveforms, and may well have caused terahertz absorptions. The bonding technique itself relies on the hydrophilicity and cleanliness of the two silicon substrates. Initial bonding via hydrogen-bridges between water molecules provides the initial room temperature bond [88]. By annealing the wafers above 100 °C, some of the water molecules diffuse laterally along the bonding interface to the edge of the wafers, whilst the remainder diffuses through any oxide and oxidises the silicon. The removal of the water molecules leaves silanol bonds at the bonding interface, creating the wafer bond [88]:

$$\text{Si-OH} + \text{HO-Si} \rightarrow \text{Si-O-Si} + \text{H}_2\text{O} \tag{3.1}$$

Although hydrophobic bond formation is possible, the majority of literature on the subject focusses on the hydrophilic technique. Surface cleanliness is essential to produce void free bonds, a fact displayed by the vast literature surrounding this topic, which presents a multitude of surface cleaning routines and treatments. Some adopt RCA cleaning procedures [89–91], whilst others use piranha solution as a means to remove metallic contaminants on the surface [92, 93]. Nitric acid is also commonly used to further clean wafers [91, 92, 94], whilst others expose the wafers to UV radiation to aid in the breakdown of organic contaminants [90]. A range of ion bombardment techniques are also adopted to increase hydrophilicity, including nitrogen [95], argon [93] and oxygen [89, 92, 96].

After a range of bonding trials, varying a selection of cleaning parameters, a procedure was developed which produced void free bonds over the whole of the wafer area. The

stringent cleaning procedure was as follows: 10 min piranha ($H_2SO_4$, $H_2O_2$, 1:1), deionised (DI) water rinse, 7 min UV exposure, isopropanol (IPA) rinse, DI rinse, 5 min piranha, DI rinse, 5 min HF etch (HF, $H_2O$, 1:10), DI rinse, 5 min piranha, DI rinse, spin dry. To increase the hydrophilicity of the silicon surface, the wafers were subjected to an oxygen plasma treatment (200 W, 100 sccm $O_2$, 200 mTorr, 30 s), followed by a 3 min hydration step in DI water. After spin drying, the wafers were brought into contact at one point to allow a 'bonding wave' to initiate, pulling the wafers together [88]. After annealing the wafer pair at 500 °C for 4 hours, the bonded system was analysed using a thermal imaging camera to ensure that the bond was void free, and that the channels were fully sealed. Two examples taken from these trials can be seen in figure 3.4. Figure 3.5 shows video stills demonstrating how capillary action fills the channels when water is dropped on one of the ports. The hydrophilic nature of the silicon ensures minimal pumping pressure when interchanging samples.

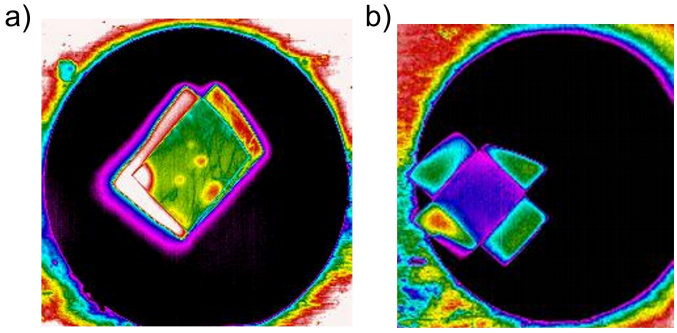


Figure 3.4: Images taken using a thermal imaging camera showing a) an unsuccessful bond with large voids and b) a void free wafer bond.

### 3.2.4 PDMS Coupling Structures

Now that a fully sealed microfluidic device fabricated solely out of silicon had been created, a reliable way of interchanging samples had to be devised. This was accomplished by fabricating PDMS coupling structures which would sit in the ports of the device, as depicted in figure 3.6b.

Figure 3.5: Still images taken using a thermal imaging camera showing how capillary action fills the chamber. Water is dropped from a pipette onto the input port of the left hand chamber. The chamber is then seen to fill with water, observed by a colour change (red to green/yellow) in the false colour image.

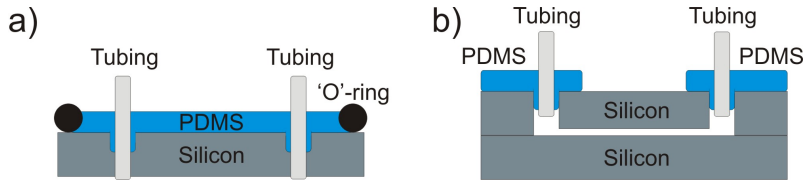


Figure 3.6: a) Moulding of the PDMS coupling structures on the dummy silicon wafer. b) Schematic of how the PDMS coupling structures sit in the ports, granting access to the capillaries and chamber.

The coupling structures were fabricated by curing PDMS around 4 mm diameter tubing on a dummy wafer (fig. 3.6a). The dummy wafer was fabricated using two subsequent etches of a silicon wafer. Two circular regions, whose dimensions matched the dimensions of the input port on the microfluidic device, were defined using S1813 photoresist. The regions were etched to a depth of 300 $\mu$m using a $XeF_2$ etch. Patterning of the reverse of the wafer was done using AZ4562 photoresist. Double sided alignment was used to define 4 mm diameter circles in the resist, centered on the etched regions on the front side of the wafer. A further $XeF_2$ process then etched these regions through the remainder of the wafer. The 4 mm diameter tubing was placed through the newly created holes, whilst a rubber O-ring was glued to the wafer to contain the PDMS. Once poured over the device, the PDMS was cured at 120 °C for 20 minutes. After peeling the PDMS from the wafer, rectangular sections were cut accordingly (fig. 3.6b). After carefully aligning the coupling structures with the ports on the microfluidic device, the whole system was placed in a clamping mechanism to apply even pressure between the PDMS and the silicon to ensure

that no leaks would occur (fig. 3.7).

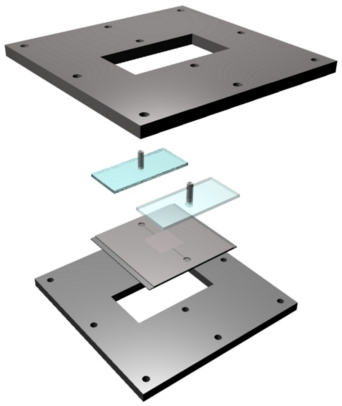

Figure 3.7: An exploded view of the system. Two metal plates are used to clamp the PDMS coupling structures in place. The central cut out in the metal plates allows the terahertz beam to pass solely through the chamber.

The above device succeeds in several areas. Firstly, the device is fabricated from a terahertz transparent material - silicon. Secondly, the depth of the chamber is kept small so that strong signals can still be detected, even when using optically dense samples. Thirdly, the chamber depth cannot only be precisely controlled, but also measured, giving us a highly accurate determination of the optical path length of the terahertz beam. Fourthly, samples can be interchanged with ease by simply pumping fluids through the chamber by means of the PDMS coupling structures. This arrangement obviates the need to remove the device from the terahertz beam, meaning no alignment discrepancies are incurred when interchanging samples. Finally, the design and construction method can be easily adapted to increase functionality through the integration of plasmonic structures or additional mixing chambers. These five advantages highlight the benefits of this device over previous solutions.

## 3.3 Results

The device function was initially investigated to see how the empty device behaved in the terahertz beam. By looking at figure 3.8a, many features of the device function can be

observed. First, the time delay of the main pulse compared to the free space reference is apparent. This time delay arises due to the high refractive index of silicon at terahertz frequencies. It is this high refractive index which also causes the reduction in signal between the free space and the empty chamber measurements. The Fresnel equations predict a 30 % reflection from each silicon-air interface. As four such boundaries are present in the device, only around 25 % of the reference signal can be expected to be detected after interaction with the chamber, as displayed by the relative pulse intensities in figure 3.8a.

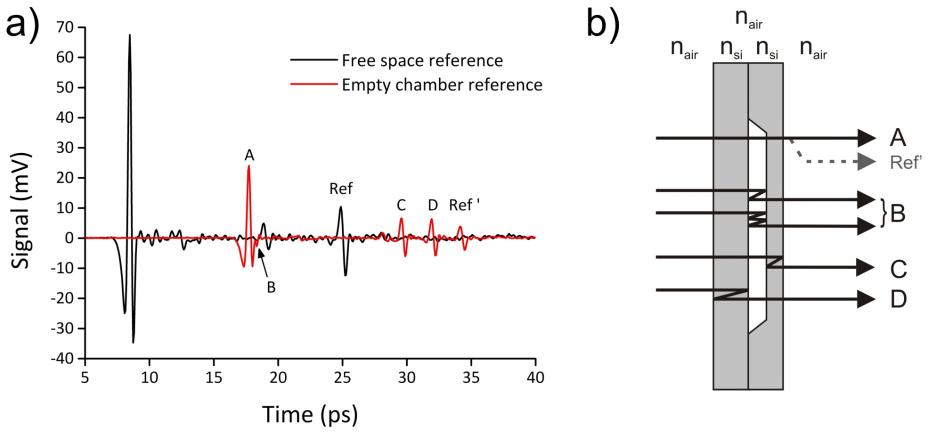


Figure 3.8: a) Temporal waveforms showing the comparison of the system reference with the empty chamber reference. Pulse A represents the main system pulse through the chamber, B represents the reflections inside the chamber, C and D arise from reflections inside the silicon substrates and Ref' represents the delayed system reflection Ref. b) Schematic of the corresponding temporal pulses recorded in a).

A system reflection in the reference scan (Ref in fig. 3.8) can be seen occurring at 25 ps. With the introduction of the chamber, this reflection can be seen at 35 ps, and is preceded by reflections occurring from inside the silicon wafers at 30 ps and 32 ps respectively. The multiple reflections occurring inside the chamber (as discussed in section 2.4.1) can be seen after the transmission of the main pulse through the chamber, identified by two small oscillations. As only two oscillations can be observed due to the compound Fresnel reflections extinguishing the beam intensity, this confirms the previous assumptions that higher orders did not need to be considered for the data extraction.

### 3.3.1 Primary Alcohols

To test the sensitivity of the device, an experiment analysing different IPA-water mixtures was undertaken. A range of mixtures were prepared, with the water content varying from 0 % to 100 % by volume, in 10 % increments. The time-domain results for this data can be seen in figure 3.9. As the reflections occurring from inside the silicon wafers occur so late in time, the temporal pulses can be truncated as shown. The featureless spectra associated with liquids in the terahertz region results in no oscillations occurring after the main pulse. This allows the truncated dataset to be zero padded, a method commonly used in far-infrared experiments as a means to improve frequency resolution [97, 98].

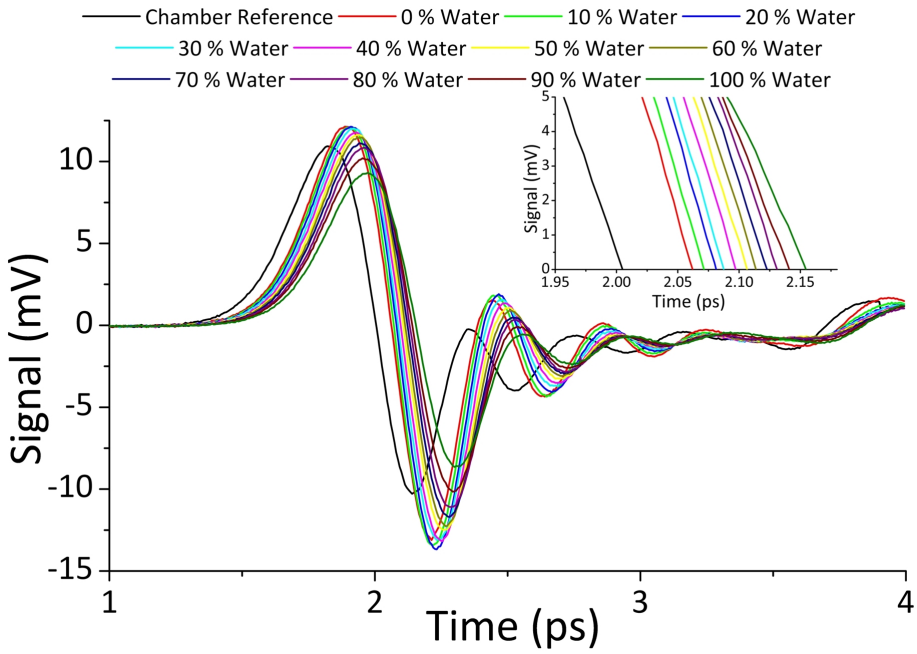


Figure 3.9: Temporal waveforms for the IPA-water mixture series.

Examination of the intensity of the main pulse shows there is a clear decrease in the signal amplitude as the water concentration is increased, owing to the greater absorption of water over IPA. As the water concentration is increased, the pulse shifts further in time with respect to the chamber reference, resulting from the higher effective refractive index of the samples. An increase in intensity can be observed between the sample and the empty chamber reference for the low water concentrations. This can be explained due to

the improved refractive index matching between the sample and the silicon, as opposed to that of silicon and air. As the water concentration is increased, the increased absorption of the sample outweighs this improved matching.

The refractive index of the solutions was extracted using the techniques described in section 2.4.2, and can be seen in figure 3.10. The results are in good agreement with data obtained via other techniques [99], and clearly display the different optical properties of IPA and water at terahertz frequencies. The 3 mm focal spot of the terahertz beam, combined with an optical path length of 50 $\mu$m, means a volume of only 1.4 $\mu$l of liquid is analysed in each scan. This highlights the sensitivity of the device: differences in the refractive index can be easily detected between 10 % changes in alcohol concentration, even with the $\mu$litre quantities being analysed, and the sub-wavelength sample interaction. In summary, the device can detect differences to the order of 2 $\mu$mol of IPA in solution. By analysing these results at selected frequencies, a linear plot is produced (fig. 3.11).

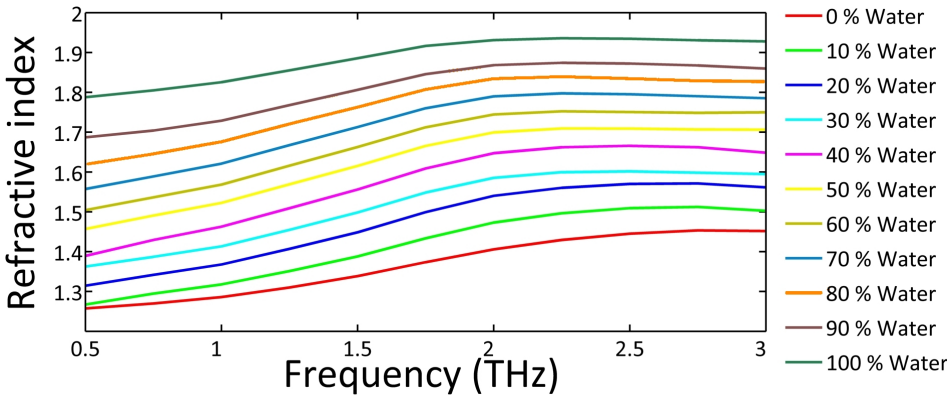


Figure 3.10: Calculated refractive indices for IPA-water mixtures.

There is only one instance in the literature where the detailed analysis of IPA-water mixtures has been undertaken [99]. To allow for greater examination of our results, a further set of experiments investigating the dielectric properties of ethanol was undertaken. For a direct comparison to work undertaken by both reflection spectroscopy techniques [16, 17, 100] and transmission arrangements [21], the real and imaginary parts of the complex dielectric function were plotted as a function of frequency (fig. 3.12). This result

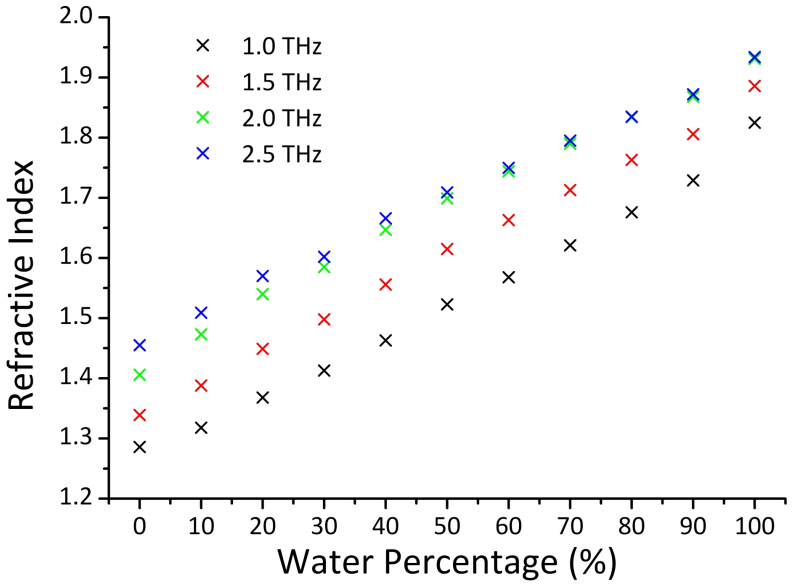


Figure 3.11: Analysis of the calculated refractive indices of different IPA-water mixtures for selected frequencies.

highlights the distinct differences between the complex dielectric function parameters of water and ethanol in the terahertz regime. Furthermore, the results are comparable to those acquired in literature by reflection and transmission arrangements [16, 17, 21, 100], confirming the validity of the device and the data extraction techniques.

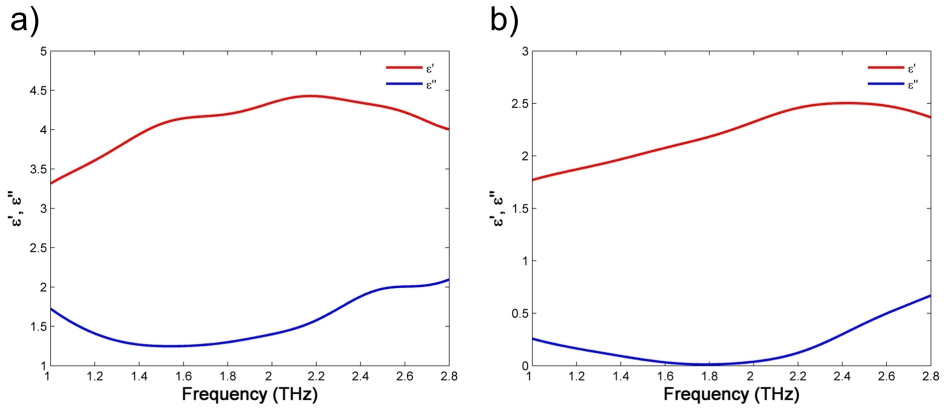


Figure 3.12: Real and imaginary parts of the complex dielectric constant for a) water and b) ethanol.

Finally, the sensitivity to different alcohols was also displayed in a further experiment involving both ethanol and IPA. Samples of each alcohol were pumped, in turn, through the device. The results displayed in figure 3.13, show the sensitivity and reproducibility of

the device, with the distinct differences between the two samples being highlighted, whilst the two readings for each individual alcohol are almost indistinguishable from each other.

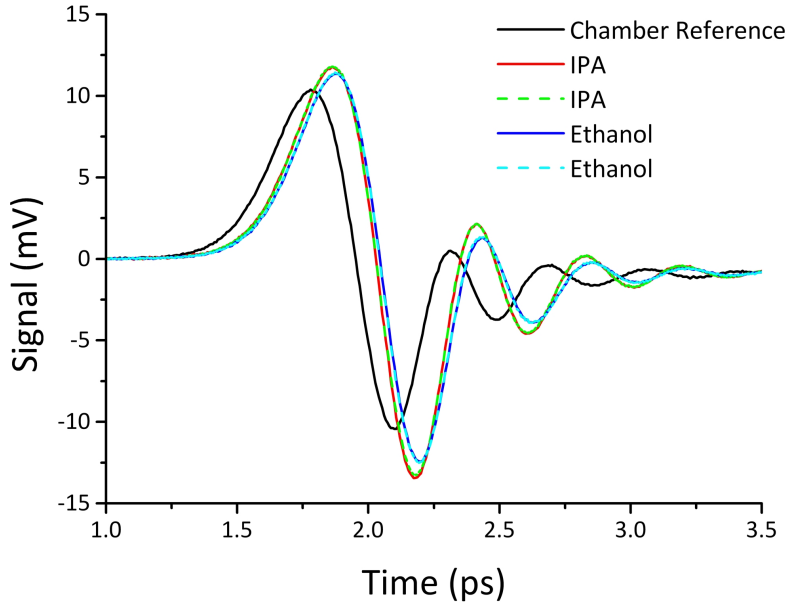


Figure 3.13: Temporal waveforms for primary alcohols demonstrating the sensitivity and reproducibility of the device.

### 3.3.2 Commercial Whiskies

A further experiment was conducted into the analysis of different commercial whiskies using the device. Figure 3.14 shows that clear differences can be detected between the samples. As all the samples had an alcohol content of 40 % by volume, these differences can be attributed to the individual composition of the samples (carbonyl compounds, carboxylic acids and esters, for example), as distinct from their alcoholic content.

To assess the reproducibility and robustness of the device and associated data extraction algorithms, a sample of 'Famous Grouse' whisky was tested on two subsequent days after a complete realignment of the device in the TDS system. The dielectric information, extracted for both sets of data, is displayed in figure 3.15.

The traces displayed in figure 3.15 have reduced chi-squared values of 2.43 and 2.19

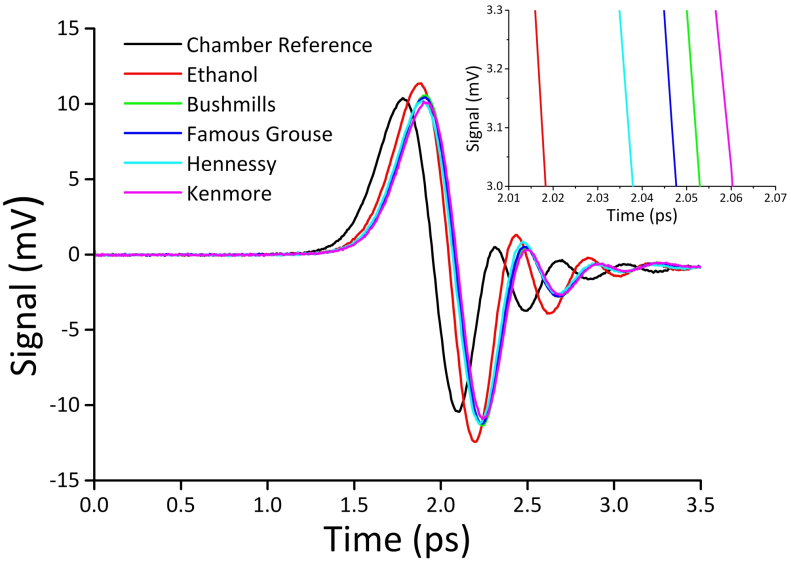


Figure 3.14: Temporal waveforms for a selection of commercial whiskies.

for $\epsilon'$ and $\epsilon''$ respectively, showing the data to be highly consistent, even after a complete realignment of the device and the day-to-day fluctuations expected with a THz-TDS arrangement. This confirms the reproducibility of the results obtained using the device and the associated data extraction algorithms. By taking alternative samples of the same whisky ('Famous Grouse') with slightly different alcoholic content (37.5 % and 40 % respectively), a further test of the device sensitivity was undertaken (fig. 3.16). The results are consistent with the alcoholic content of the samples. The sample containing 40 % alcohol has a lower $\epsilon''$ value than the 37.5 % sample. This result is to be expected as the sample containing 40 % alcohol will contain less water, which as demonstrated in section 3.3.1, is more absorbing than ethanol over the investigated frequency range. Reduced chi-squared results of 2.89 and 11.21 for $\epsilon'$ and $\epsilon''$ respectively, are achieved when analysing the two traces. These values are greater than the reduced chi-squared data calculated for the day-to-day variations in the spectroscopy arrangement. This result demonstrates how this device can be used to reliably distinguish between different commercial brands of whisky, and also distinguish between the alcoholic content of the same whisky blend. This could have potential avenues in the detection of counterfeit products.

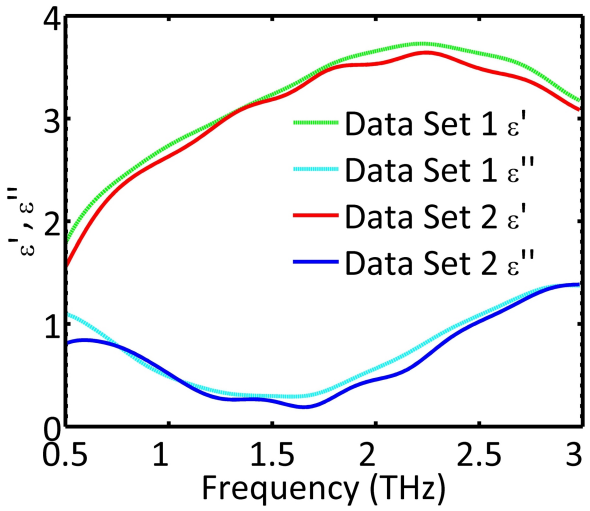


Figure 3.15: The dielectric constants extracted for the same whisky sample, taken on subsequent days after a complete realignment of the device in the TDS system.

### 3.3.3 Organic Compounds

The sensitivity of the device to organic compounds was also displayed, as shown in figure 3.17. Here, slight absorption differences could be detected between amyl and ethyl acetates, whose structures differ only in the length of the carbon backbone of the molecules. The much larger compound, diethyl malonate, resulted in a more pronounced absorption difference. The sensitivity of the device to these organic samples confirms the results presented in section 3.3.2, where absorption differences between different commercial samples were attributed to the varying amounts of organic material present.

### 3.3.4 Biotin

Biotin, commonly known as vitamin $B_7$, has been well studied at terahertz frequencies. All analysis has however, been undertaken using a dried or pellet form of the sample [101], with the sample being prepared in a polyethylene matrix. In this form, biotin exhibits specific frequency absorptions throughout the terahertz region. Here, a powdered form of the sample was mixed with de-ionised water to form a range of solutions, covering a fully dissolved regime, to a heavily saturated solution. The temporal waveforms acquired

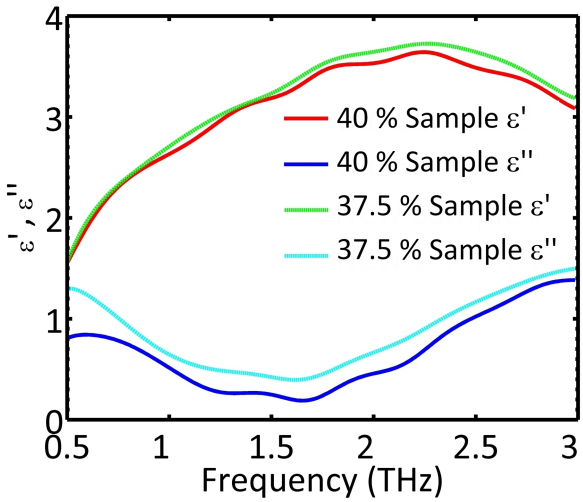


Figure 3.16: The dielectric constants extracted for different samples of the same brand of whisky ('Famous Grouse'). The lower absorption exhibited by the 40 % sample is consistent with the composition of the samples.

for these experiments are displayed in figure 3.18. The decrease in signal intensity as the percentage of biotin in solution is increased can be clearly observed, owing to the strong absorption properties of the molecule in the terahertz regime. A slight decrease in time delay referenced to the empty chamber is also observed as the biotin percentage is increased. This can be attributed to the lower real part of the refractive index of the biotin, compared to that of water.

The FFT data displayed in the inset of figure 3.18 shows that no frequency specific absorptions are evident for biotin in solution, with only blanket absorptions being observed. This result is consistent with a change in absorption mechanism when moving from a crystalline to aqueous sample in the terahertz region. The 0.5 g/l changes detected using the device corresponds to a sensitivity in the order of 3 nmol for biotin in solution. The demonstration of such sensitivity using $\mu$litre volumes at highly sub-wavelength thicknesses, confirms that the original design specifications have been achieved, and strongly suggests this device may provide a potentially useful means to analyse aqueous biological systems at terahertz frequencies.

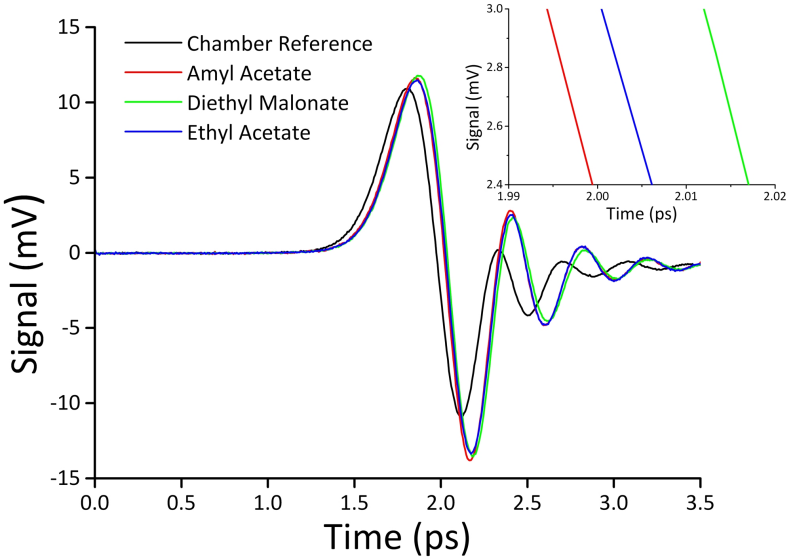


Figure 3.17: Temporal waveforms acquired for a variety or organic compounds.

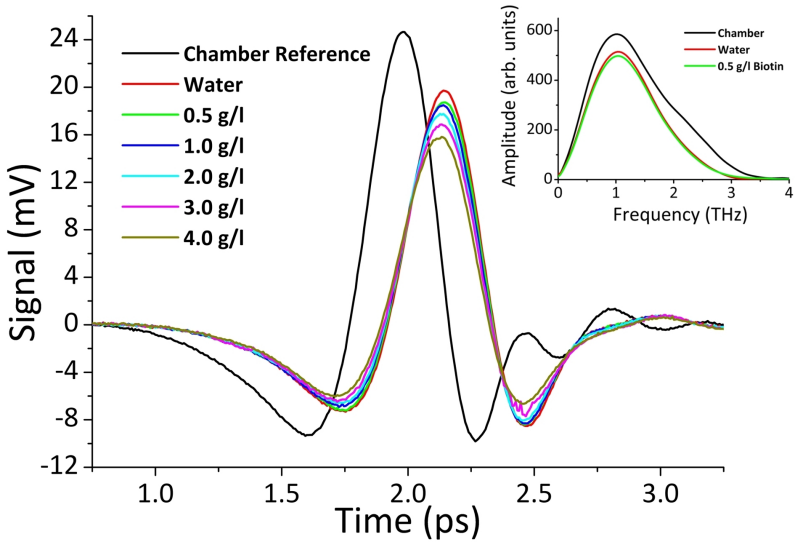


Figure 3.18: Temporal waveforms acquired for different aqueous solutions of biotin with associated FFT data.

# Chapter 4

# Surface Plasmons

The following chapter provides a detailed background to the theory underpinning the phenomenon of surface plasmon polaritons. The vast literature surrounding this topic is often approached from an optical perspective, failing to bridge the gap between traditional lower frequency surface modes such as Zenneck waves, and surface plasmons. Furthermore, with current theories surrounding surface plasmon activity in the terahertz region differing greatly, this succinct summary serves to provide a well balanced introduction to surface plasmons in the terahertz regime. A critique of experimental results is provided, along with an interpretation of the 'spoof' surface plasmon theory initially presented by Pendry [38]. The chapter describes the mechanisms exploited in chapters 5, 6 and 7, to excite and utilise surface plasmons, and also provides a background to the ideas used for the qualitative time-of-flight model, developed to explain the transmission properties of two-dimensional sub-wavelength aperture arrays, presented in chapter 6.

## 4.1 Formal Definition

A plasmon can be formally defined as "a quantum quasi-particle representing the elementary excitations, or modes, of the charge density oscillations in a plasma" [102]. This description can be distilled into two key points. Firstly, a quantum-classical parallel is

clearly evident, where a quantised particle-like system can be used to describe the essentially classical oscillations of a charge density. Secondly, the 'quasi' classification of these particles emphasises the highly-interacting (and therefore lossy) nature of these oscillations. A simple analogy can thus be drawn between plasmons and photons - a plasmon is to the charge density what photons are to the electromagnetic field [102].

When an EM wave is incident upon an optically responsive medium, energy coupling exists between the EM field oscillations and the internal degrees of freedom of the medium. Such coupling results in the formation of polaritons. For the case of EM radiation coupling to the free-electron plasma in a medium, the resultant quanta are known as a plasmon-polaritons.

Surface plasmon-polaritons (SPPs) are formed when a longitudinal charge density propagates at the interface between a dielectric medium and a conductor, after excitation by an external EM source. The resultant TM surface waves are part propagating EM radiation, part charge density oscillation. Such hybrid modes are characterised by an evanescently decaying field perpendicular to the surface, existing either side of the supporting medium. The confinement, localisation and lifetime of the SPPs rely intimately on the dielectric properties of both the conductor and the neighbouring dielectric. Structuring the surface of the conductor allows these fundamental characteristics to be engineered to suit the desired application.

The sensitive nature of SPPs has been exploited in a wide range of applications, most notably in spectroscopy, where Surface Plasmon Resonance (SPR) and Surface Enhanced Raman Spectroscopy (SERS) are now well-established techniques [103, 104]. Subwavelength confinement of SPPs throughout the optical regime has led to the development of plasmonic interconnects for photonic circuitry [105]. Elsewhere, vast amounts of research has been focussed on the role of SPPs in the phenomenon of extraordinary optical transmission (EOT), and how such effects can be observed even in the microwave and THz regimes, where metals can be described as perfect electrical conductors (PECs) [38, 106].

This topic will be explored in greater detail in section 4.3.2. The following section will seek to give a detailed narrative of the mathematical formalisms that describe SPPs - something which is often overlooked in texts on the subject.

### 4.1.1 Physical Interpretation of SPPs

SPPs exist at the boundary between a conductor and a dielectric. Physically, SPPs can be thought of as an oscillation and propagation of the conduction electrons in a conductor which reside close to the surface. A simple analogy of this is to picture SPPs as ripples in the density of conduction electrons, much like waves emanating on a still pond from the impact of a dropped stone. This analogy highlights the fact the excitation of SPPs results in the oscillation of charges. These oscillations, in turn, establish a propagating electric field along the surface, which decays exponentially away from the surface, as depicted in figure 4.1.

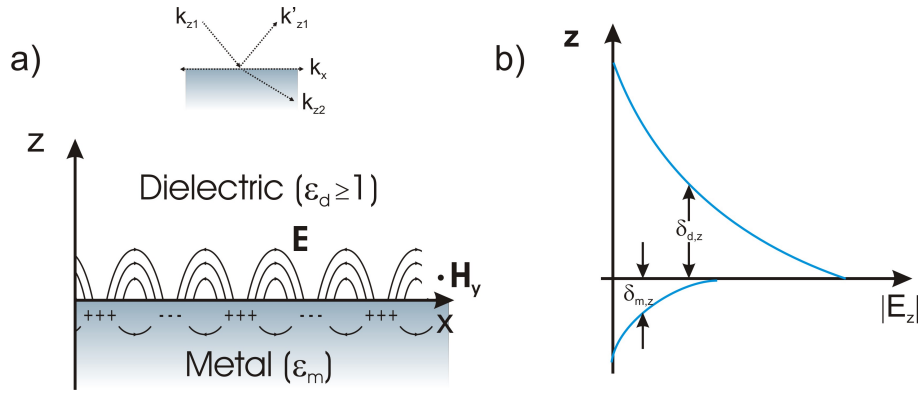


Figure 4.1: a) Diagram depicting the motion of charges and the EM fields established upon excitation of a SPP mode. b) Representation of the exponential decrease of the field perpendicular to the surface in both the metal and the dielectric. $k_x$ corresponds to the wavevector parallel to the interface, $k_{zn}$ corresponds to the perpendicular wavevector, where a $'$ indicates a reflected wavevector. Adapted from [35].

## 4.2 Origin and Classification of SPP Modes

For a thorough understanding of the complex nature of SPPs, it is essential to start from first principles, allowing us to see how even their most basic of properties are derived. In doing so, we draw upon our knowledge of how light travels along a surface. When light travels along a surface, it has a wavevector along its direction of propagation, $k_x$, which is related to the momentum of the light. The energy of this light can be expressed as:

$$E = \hbar 2\pi\nu = \hbar\omega = \hbar c k_x \tag{4.1}$$

Here, $\nu$ is the frequency of oscillation (in Hz) and $\omega$ is the angular frequency. A dispersion relation describes how both the energy and the momentum of light are related. From equation 4.1, it is trivial to prove the dispersion relation of light in a vacuum is governed by the relationship $\omega = ck_x$. SPPs, however, do not follow this simple relationship as they exist at the interface of a metal and a conductor, the dielectric properties of which are different to those of a vacuum. Such an interface has a dielectric constant, $\epsilon$, approximated by [35]:

$$\epsilon = \frac{\epsilon_m \epsilon_d}{\epsilon_m + \epsilon_d} \tag{4.2}$$

Here $\epsilon_m$ and $\epsilon_d$ are the dielectric constants of the metal and the dielectric respectively. The dielectric constant of a medium is related to its index of refraction, $n$, by the relationship:

$$n = \sqrt{\epsilon} \tag{4.3}$$

Ultimately, the dielectric constant of a medium governs the velocity of light passing through it. For a material with a dielectric constant greater than that of a vacuum (i.e. $> 1$), the velocity of light passing through that material will be reduced. As the dielectric constant of an interface supporting SPP modes is governed by the relationship given in equation 4.2, the velocity of SPPs proportional to their momentum is reduced compared

| **Mode** | $\Re(\epsilon_m)$ | $\Im(\epsilon_m)$ | **Nature of** $k_x$ | **Nature of** $k'_{z1}$ | | **Nature of** $k'_{z2}$ | |
|---|---|---|---|---|---|---|---|
| | | | | $\Re$ | $\Im$ | $\Re$ | $\Im$ |
| *Brewster Modes* | $> 0$ | $= 0$ | Real | $> 0$ | $= 0$ | $> 0$ | $= 0$ |
| | $> 0$ | $> 0$ | Complex | $> 0$ | $< 0$ | $> 0$ | $> 0$ |
| *Localised SPPs* | $0 > \Re(\epsilon_m) > -\epsilon_d$ | $= 0$ | Pure Imaginary | $< 0$ | $= 0$ | $> 0$ | $= 0$ |
| | $0 > \Re(\epsilon_m) > -\epsilon_d$ | $> 0$ | Complex | $> 0$ | $< 0$ | $< 0$ or $> 0$ | $> 0$ |
| **Propagating SPPs** | $\epsilon_d > \Re(\epsilon_m)$ | $= 0$ | Real | $= 0$ | $< 0$ | $= 0$ | $> 0$ |
| | $\epsilon_d > \Re(\epsilon_m)$ | $> 0$ | Complex | $> 0$ | $< 0$ | $< 0$ or $> 0$ | $> 0$ |

Table 4.1: The types of EM modes existing at a planar dielectric/metal interface, assuming $\epsilon_d > 1$. Adapted from [102].

to that of light in a vacuum [107]. SPPs follow dispersion relations governed by the following relationships, given here for directions both parallel ($k_{SPP_x}$) and perpendicular ($k_{SPP_z}$) to the surface [35]:

$$k_{SPP_x} = \frac{\omega}{c}\sqrt{\frac{\epsilon_m \epsilon_d}{\epsilon_m + \epsilon_d}} \tag{4.4a}$$

$$k_{SPP_{z,d}} = \frac{\omega}{c}\sqrt{\frac{\epsilon_d^2}{\epsilon_m + \epsilon_d}} \tag{4.4b}$$

$$k_{SPP_{z,m}} = \frac{\omega}{c}\sqrt{\frac{\epsilon_m^2}{\epsilon_m + \epsilon_d}} \tag{4.4c}$$

Here the dielectric constant of the metal, $\epsilon_m$, is a complex function of frequency, whose value can be approximated through implementation of the Drude model, as detailed in section 4.3.1.

As the exact nature of each SPP mode relies critically upon the complex dielectric properties of the conductor, all the relationships given in equation 4.4 can take on real or imaginary values. Table 4.1 summarises all the modes which can exist, given the numerous permutations of the dielectric properties of a conductor.

The region in table 4.1 corresponding to the 'Brewster modes', exist when $\Re(\epsilon_m) > 0$.

For the case of a real metal, i.e. when $\Im(\epsilon_m) > 0$, these modes can be regarded as true surface modes. These surface polaritons comprise of a mixture of surface charge waves and propagating photons. Strictly speaking, these modes are not conventionally described as surface plasmon polaritons; this classification is reserved for the case when $\Im(\epsilon_m) < 0$.

The modes corresponding to those labelled 'localised SPPs' indicate a non-propagating surface wave, highlighted by the pure imaginary value of $k_x$. For the case of an ideal metal, i.e. when $\Im(\epsilon_m) = 0$, these modes can be considered radiative as the evanescent energy of the surface wave is dissipated away from the surface via the real, propagating $k_z$ modes. Such modes become non-radiative for the case of a real metal as the $k_z$ modes become evanescent, meaning they can no longer radiate the evanescent surface wave.

Finally, and most importantly, we arrive at the case of 'propagating SPPs', existing when $-\epsilon_d > \Re(\epsilon_m)$. The pure imaginary nature of both $k'_{z1}$ and $k_{z2}$ display the evanescent decay of the field perpendicular to the surface, whilst the real value of $k_x$ highlights the propagating nature of the established surface wave. These non-radiative modes are known formally as propagating surface plasmon polaritons, and are fully trapped at the conductor-dielectric boundary. For the case of a real metal, the imaginary nature of $k_x$ results in these modes becoming pseudo-propagating - i.e. there is only a certain distance the SSPs can travel before damping induced losses imposed by the metal become overwhelming.

### 4.2.1 SPP Dispersion Relations

The dispersion relations given in equation 4.4 relate the wavevectors of propagation with the frequency of oscillation. When presented graphically, individual features of each mode can be readily identified, as shown in figure 4.2. The three different modes identified in table 4.1 are easily observed, namely the Brewster modes, along with the localised and propagating SPP modes.

The branch related to the Brewster modes can be identified at frequencies above the plasma frequency of the metal, $\omega_p$, a concept which will be discussed in more detail in

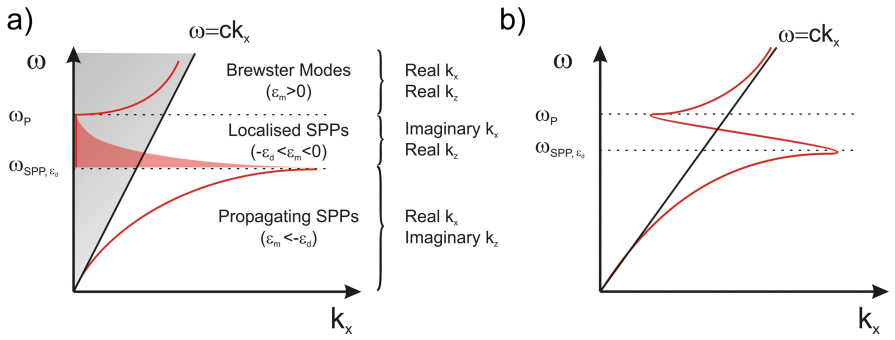


Figure 4.2: a) Dispersion relation for a lossless Drude metal. Free space photons lie in the shaded grey region, to the left of the light line. The broadening of the localised SPPs (indicated by the shaded red region) arises due to the strong evanescent nature of these modes. b) Dispersion relation when losses are included.

section 4.3.1. The propagating SPP branch can be seen to approach the limiting frequency $\omega_{SPP}$ as $k_x$ increases. For a perfect Drude metal, this frequency can be shown to be [35]:

$$\omega_{SPP} = \frac{\omega_p}{\sqrt{(1+\epsilon_d)}} \tag{4.5}$$

The asymptote which emerges as $k_{SPPx}$ approaches $\omega_{SPP}$ arises due to the dielectric constant of the metal approaching $-1$. At low frequencies, the propagating SPP mode approaches the light line, where the modes take on a more 'photon-like' appearance [102], behaving like a photon travelling at grazing incidence along the surface.

Between the Brewster and propagating modes reside the localised SPP modes. In this region, significant broadening of the mode is often observed due to the losses associated with metals. In the case of a real metal, a 'bending back' of the dispersion relation is often seen as the frequency is increased; a phenomenon observed experimentally using silver [108]. In the case of gold, inter-band transitions drastically increase plasmon losses for wavelengths shorter than 600 nm. For cases where extremely high losses exist, it becomes increasingly difficult to distinguish between the localised and propagating modes, as the latter become progressively more 'lossy' [102].

The back bending of the dispersion curve arises only when losses in the metal are taken into account, i.e. when $\Im(\epsilon_m) \neq 0$. When this condition arises, the dispersion relationship

given in equation 4.4 becomes complex, thus either $\omega$ or $k_x$ must be complex. For the case of a complex frequency (i.e. $\omega = \omega' + i\omega''$), the field decays in time as $\exp(\omega'' t)$, no back bending occurs, and $k_x$ becomes increasingly large as $\omega$ approaches $\omega_{SPP}$. On the other hand, for the case of a complex wavevector (i.e. $k_x = k_x' + ik_x''$ ), the field decays exponentially in space, and the wavevector for propagation is given by $\Re(k_x)$. In this instance, the imaginary part of the denominator in equation 4.4 never vanishes; thus $\Re(k_x)$ never becomes infinite, and the dispersion curve ($k_x'$ vs. $\omega$) exhibits a back bending as $\omega$ approaches $\omega_{SPP}$ [109].

### 4.2.2 Excitation of Propagating SPPs

There is an important issue related to the excitation of propagating SPPs. Careful analysis of figure 4.2a shows such modes lie on the right hand side of the light line, meaning they cannot be readily excited using free space photons. Modes which lie to the right of the light line have a momentum greater than those associated with free space photons of the same frequency. In order to overcome this momentum mismatch, a coupling medium must be used to excite propagating SPPs.

One of the most commonly used techniques to excite SPPs utilises the technique of attenuated total reflection (ATR). The two most prominent methods are the Otto [110] and Kretschmann [111] configurations, as depicted in figure 4.3. Upon the total internal reflection (TIR) conditions being met, an evanescently decaying wave is established in the medium of lower refractive index. In the Otto configuration, this decaying EM field is brought into close proximity with a metal surface. In doing so, SPPs are excited along the metal-dielectric interface.

The Kretschmann geometry uses a similar technique, however, in this instance, SPPs are excited on a thin film of metal evaporated on the surface of the prism. This technique solves many of the experimental problems associated with the Otto configuration, namely SPP-evanescent field coupling and reliable metal-prism separations. The use of the above

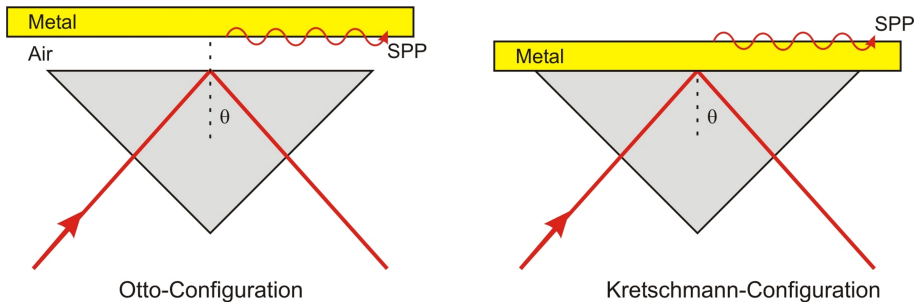


Figure 4.3: Diagram showing the Otto and Kretschmann configurations used to excite SPPs in the optical regime.

techniques eventually led to the creation of surface plasmon resonance (SPR) experiments, now used extensively in bio-sensing applications [103, 112].

The effectiveness of the above ATR techniques can be crudely described by means of a further dispersion relation diagram. Figure 4.4 shows that when light travels through a prism, its light line is lowered due to the higher refractive index of the prism over that of air. If a prism of the correct refractive index is used, the light line describing photons in the prism can be made to overlap with the branch associated with propagating SPPs, effectively solving the momentum mismatch problem.

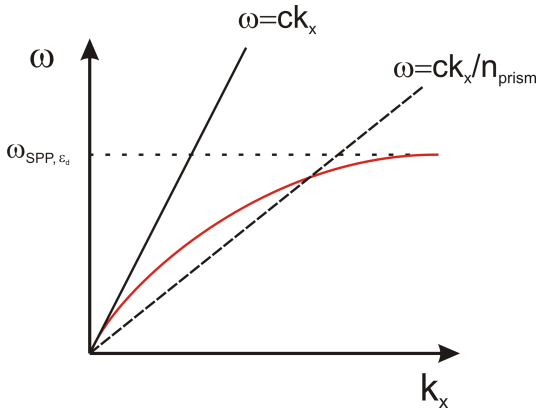


Figure 4.4: Dispersion relation showing the lowering of the light line when light enters a medium of high refractive index.

Further techniques used to excite propagating SPPs involve the use of point defects, surface roughness and diffraction gratings [35].

### 4.2.3 Losses and Decay Lengths

Once propagating SPPs have been excited, they remain bound to the surface and are strictly non-radiative. When absorption losses are neglected, SPPs will propagate indefinitely along the conductor-dielectric interface. When losses are included, SPPs will eventually dissipate by optical absorptions in the metal. These losses are usually resistive in nature, and can be described by the imaginary part of the dielectric constant of the metal. In real metals, as such losses do exist, the wavevector determining propagation along the interface becomes a complex value for all frequencies [35]:

$$k_x = k'_x + ik''_x \tag{4.6}$$

Here, the real part of the wavevector corresponds to the wavelength of the plasmon, $\lambda_{SPP} = 2\pi/k'_x$ , whilst the imaginary part represents the damping factor. Making the assumptions that $|\epsilon''_m| << |\epsilon'_m|$ (as is the case in the optical regime), and that the dielectric constant of the dielectric material is real, the wavevector components can be approximated to [35]:

$$k'_{SPP_x} \approx \frac{\omega}{c}\sqrt{\frac{\epsilon'_m\epsilon_d}{\epsilon'_m + \epsilon_d}} \tag{4.7a}$$

$$k''_{SPP_x} \approx \frac{\omega}{c}\left(\frac{\epsilon'_m\epsilon_d}{\epsilon'_m + \epsilon_d}\right)^{\frac{3}{2}}\frac{\epsilon''_m}{2\epsilon'^2_m} \tag{4.7b}$$

The inclusion of Ohmic losses results in a damping of the SPPs in the metal, causing the field intensity to decay as $\exp(-2k''_x)$ [102], thus, one can define the propagation length of SPPs as:

$$L_{SPP} = \frac{1}{2k''_x} \tag{4.8}$$

If the losses in the metal are small, the propagation distance, $L_{SPP}$, can be much greater than the wavelength. This is often the case when approaching the THz regime. Further-

more, as the frequency of the SPPs approaches $\omega_{SPP}$, the associated losses dramatically increase, owing to the fact a greater proportion of the SPP is located inside the metal due to the increased transverse confinement.

The decay lengths normal to the surface, either side of the interface are governed by the following equations [35]:

$$\delta_{m,z} = \frac{c}{\omega}\sqrt{\frac{\epsilon'_m + \epsilon_d}{\epsilon'^2_m}} \tag{4.9a}$$

$$\delta_{d,z} = \frac{c}{\omega}\sqrt{\frac{\epsilon'_m + \epsilon_d}{\epsilon^2_d}} \tag{4.9b}$$

This confinement is depicted in figure 4.1b, where the decay lengths in both the metal and dielectric are displayed. The decay length of the field in the dielectric, $\delta_{d,z}$, is of the order of $\lambda/2$, whilst the decay length in the metal, $\delta_{m,z}$, is governed by its skin depth. Both the propagation distance and the confinement are strong functions of frequency. At high frequencies, $k''_x$ becomes very large due the increased confinement of the SPP in the metal, greatly reducing the propagation length of the SPP. At lower frequencies (infrared), the propagation length increases dramatically due to the increase in $\delta_{m,z}$. In this regime, the spatial extent of the SPP is often greater than the free space wavelength.

## 4.3 Optical Properties of Metals

The optical response of metals is often described in terms of their dielectric properties, which are vastly different to those observed for standard dielectrics. Phenomena such as the efficient reflection of visible light, along with superb electrical and thermal conduction properties, can be attributed to the presence of free electrons residing in the conduction band. The movement of these electrons in a background of fixed positive charge, by definition, forms a free electron plasma. The manner in which this plasma reacts to external EM radiation governs the optical response of the metal. The Drude model,

detailed in the following section, is a simplistic model used to predict the optical responses of metals throughout the optical regime.

### 4.3.1 Drude Model

The well known Drude model of conduction electrons can be used to predict the dielectric function of both metals, and semiconductors, as a function of frequency. The model is based on the formulation of the Coulomb interactions experienced between the free electron plasma and the positive crystal lattice. The plasma frequency, $\omega_p$, describes the natural oscillation frequency of the free electron plasma in a volume metal:

$$\omega_p = \sqrt{\frac{ne^2}{\epsilon_0 m_e}} \tag{4.10}$$

Here, $e$ and $m_e$ are the charge and effective mass of an electron respectively, $n$ is the conduction electron density and $\epsilon_0$ is the permittivity of free space. The high electron densities in metals result in plasma frequencies residing in UV part of the spectrum. The Drude model describes the optical response of the plasma to an external EM source:

$$\epsilon(\omega) = \epsilon_\infty - \frac{\omega_p^2}{\omega^2 + i\gamma_0\omega} \tag{4.11}$$

Here, $\epsilon_\infty$ is the optical response of the positive crystal lattice, $\omega$ is the frequency of the incident radiation and $\gamma_0$ [rad $s^{-1}$], is a scattering rate (damping term) related to the collision of free electrons with the crystal lattice or other impurities, and is typically small compared to $\omega$. Dissecting equation 4.11 into its real and imaginary components allows us to gain further insight into the values of the dielectric constants of metals:

$$\Re(\epsilon(\omega)) = \epsilon_\infty - \frac{\omega_p^2}{\omega^2 + \gamma_0^2} \tag{4.12a}$$

$$\Im(\epsilon(\omega)) = \frac{\omega_p^2\gamma_0}{\omega^3 + \omega\gamma_0^2} \tag{4.12b}$$

For frequencies below the plasma frequency, it becomes clear that the real part of the dielectric constant is negative, i.e. $\Re(\epsilon(\omega)) < 0$. As we approach the plasma frequency, the scattering rate becomes increasingly insignificant ($\omega >> \gamma_0$), and the condition $\Im(\epsilon_m) \approx \frac{\omega_p^2}{\omega^3} << |\Re(\epsilon_m)|$ exists, satisfying the properties outlined in section 4.1 allowing for the efficient excitation of SPPs. For lower frequencies, approaching the THz regime, the scattering term begins to dominate ($\omega << \gamma_0$). In this region the real part of the dielectric constant is still negative, however the imaginary part begins to dominate over the real part, i.e. $\Im(\epsilon_m) >> |\Re(\epsilon_m)|$.

### 4.3.2 Perfect Electrical Conductors

For frequencies much lower than the plasma frequency, (i.e. in the microwave or THz regimes), the real and imaginary dielectric constants of metals are many orders of magnitude greater than those observed for visible frequencies. Throughout and below the THz region, metals can be regarded as perfect electrical conductors (PECs). The skin depth is a measure of how the electric field from an external EM source is attenuated inside the metal. In the THz regime, this can be approximated as:

$$\delta_{skin}(\omega) \approx \frac{c}{\omega}\sqrt{\frac{2}{\Im(\epsilon_m(\omega))}} \tag{4.13}$$

As the frequency of radiation incident upon on a metal is increased, the skin depth decreases, meaning any induced oscillations of the conduction electrons exist only in ever decreasing volumes in a region close to the surface of the metal. It should be pointed out that although these oscillations exist close to the surface, they are strictly not SPPs, they are merely confined volume plasmons. Such induced oscillations do not require a metal-dielectric interface to exist, and do not propagate along the boundary. Guided waves (or SPPs) can exist at these frequencies, though excitation becomes increasingly difficult due to the increased value of $\Im(\epsilon_m(\omega))$. The properties of such guided effects

at THz frequencies (and below) will be discussed in greater depth in section 4.6, where the concept of 'spoof' SPPs will be presented. This novel approach allows the dielectric properties of a metal to be engineered using sub-wavelength surface modifications.

### 4.3.3 Semiconductors at THz Frequencies

The presence of unfilled valence and conduction bands in semiconductors allows electrons to transfer between these two states, ultimately altering the electron density. Photo-excitation, application of external electric fields, and sample doping are all examples of how this electron density can be controlled in semiconductors. By varying the electron density, the frequency dependent conductivity of the sample is altered, which, in turn, affects the optical response of the material. Above a doping density of $1 \times 10^{17}$ cm$^{-3}$, the real part of the dielectric constant of silicon becomes negative, displaying the metallic properties of the material [113]. For highly doped silicon samples (n $\approx 1 \times 10^{19}$ cm$^{-3}$), the plasma frequency of the sample is lowered into the THz region. This metallic like behaviour allows for the existence and confinement of SPPs at THz frequencies [114]. Before a discussion of THz SPP effects is presented, the experimental and theoretical work documenting their discovery will be explored.

## 4.4 Light in Sub-wavelength Apertures

The theory of optical transmission through sub-wavelength apertures dates back to the work of Bethe in 1944 [115]. The idealised structure used in this formalism was of a sub-wavelength aperture existing in an infinitely thin, perfectly conducting substrate. Bethe derived an expression for the transmission efficiency, $\eta_B$, of such an aperture:

$$\eta_B = \frac{64(\frac{2\pi r}{\lambda})^4}{27\pi^2} \tag{4.14}$$

Here, $\lambda$ is the wavelength of the incident light and $r$ is the radius of the aperture. One can clearly see from this expression that the transmission efficiency is proportional to $(r/\lambda)^4$, showing that as $\lambda$ becomes larger than $r$, a rapid decrease in intensity is predicted. Although the work of Bethe provides an elegant relationship, the neglect of an apertures finite thickness is a distinct failing of this model. Apertures of a finite depth have associated waveguide properties which determine the transmission of light, and ultimately modify the dispersion relation of the EM field [116]. Waveguides have associated cut-offs, $\lambda_c$, related to the aperture dimensions, which determine the maximum wavelength of light permitted to propagate through the aperture:

$$\lambda_c = 4r \tag{4.15}$$

When radiation is incident upon an aperture with $\lambda > \lambda_c$, the field will become evanescent in nature, decaying exponentially with aperture depth. The approximation given above for an aperture cut-off fails to take into account the finite conductivity and the skin depth of real metals, along with the excitement of localised SPP modes existing around the aperture edge. These failings lead to a large discrepancy arising between the amount of light actually transmitted, and the amount predicted by Bethe. This discrepancy has become known as 'extraordinary optical transmission' (EOT), and has been the subject of a great deal of experimental and theoretical work over the past decade since the work of Ebbesen in 1998 [37].

## 4.5 Extraordinary Optical Transmission

In 1998, Ebbesen reported upon the extraordinary transmission of light through two-dimensional arrays of apertures in silver films [37]. The startling results revealed intense transmission peaks throughout the spectral range, even for incident wavelengths much greater than the aperture or period dimensions. In this instance, the array becomes an

active element as opposed to a passive geometrical element in the path of the incident beam. The enhanced transmission was attributed to the coupling of light with the SPPs, induced by the presence of the two-dimensional array of sub-wavelength apertures. Such 'anomalous' activity has been observed when analysing gratings previously, the first instance, dating back to 1902.

### 4.5.1 Historical Context of EOT

The observations of R. W. Wood discussed the dark bands in the reflection spectrum of a metallic grating were, although unknown at the time, arguably the first experimental evidence for the presence of SPPs induced by metallic gratings [117]. Wood observed that the dark bands not only shifted as a function of incidence angle, but that they were heavily dependent upon the polarisation of the incident light also. These minima have become known as 'Woods anomalies' in modern literature.

Lord Rayleigh provided the first theory explaining both the presence and shifting behaviour of Wood's minima, attributing the anomalies to diffraction effects [118]. Rayleigh deduced a formula giving the positions of maximum intensity for a given wavelength at normal incidence:

$$a\sin(\theta_m) = m\lambda \tag{4.16}$$

Here $a$ is the line spacing and $\theta_m$ is the angle of the $m^{th}$ diffraction order. Taking an example of $a = 1$ $\mu$m and $\lambda = 600$ nm, it becomes clear that above the first diffraction order, the angles become complex (see table 4.2).

Rayleigh concluded that the orders which appear at complex angles (non-reflected orders), are responsible for the observed intensity minima. The work of J. Strong in 1936 was the first to study Wood's anomalies as a function of both the metal used to fabricate the grating, and the width of the rulings [119]. Strong found that the narrowest rulings resulted in the strongest minima, with anomalies becoming stronger as the width of the

| $m$ | $\frac{m\lambda}{a}$ | $\sin^{-1}(\frac{m\lambda}{a})$ |
|---|---|---|
| 0 | 0 | 0 |
| 1 | 0.6 | 36.7 |
| 2 | 1.2 | $90 - 35.7i$ |
| 3 | 1.8 | $90 - 68.4i$ |
| 4 | 2.4 | $90 - 87.2i$ |

Table 4.2: Diffraction angles for a 1 $\mu$m grating with an incident wavelength of 600 nm.

ruling approached the wavelength of light. Strong also found differences in the observed minima as he altered the metal used to make the grating.

It was not until 1973 that the first connection between the presence of Wood's anomalies and the excitation of SPPs was introduced. Hutley and Bird [120] drew upon the similarities between experiments conducted by Teng and Stern [121], who used 10 keV electron beams to excite surface plasmons on metal gratings, to the classical experiments performed by Wood. Hutley and Bird were able to match the theoretical predictions for the angles of SPP excitation to experimental values within 3 °, attributing the difference to the existence of a 'tarnish layer' on the metal surface. Since the work of Hutley and Bird, it is now well accepted that the occurrence of Wood's anomalies can be attributed to the excitation of SPPs.

Since the initial work of Ebbesen, there has been an explosion of research surrounding both the experimental and theoretical aspects of EOT. This work has encompassed single apertures, the one-dimensional case of sub-wavelength slits, two-dimensional arrays of sub-wavelength apertures and single apertures flanked by periodic corrugations (bulls-eye structures). These studies have not only covered a wide range of the EM spectrum (from the microwave to the visible), but have employed analysis techniques in both the time and

frequency domains. The transmission properties of such systems are governed, in part, by the following properties: aperture dimensions, aperture shape, array periodicity, ratio of basis to lattice, material of array, material of supporting substrate, angle of incident radiation, frequency of incident radiation and the thickness of the array. As one can gather from the number of variables mentioned in this paragraph, the literature regarding EOT is vast. Literature reviews for the case of bulls-eye apertures and sub-wavelength two-dimensional aperture arrays, at THz frequencies, can be found in sections 5.1 and 4.6.4.3 respectively.

## 4.6 Surface Modes at THz frequencies

Two-dimensional aperture arrays or 'metallic mesh' structures have been studied in great depth in the far-infrared (terahertz) region of the EM spectrum over the decades. This section will detail some of the early work on metallic meshes, discuss the 'similarities' between Zenneck waves and propagating SPPs, explain the fundamental theory surrounding so called 'spoof' SPPs and present an overview of recent work studying SPPs in the lower realms of the EM spectrum.

The use of metallic mesh structures as optical elements dates back to the early 1960's, where researchers utilised the cut-off characteristics of these devices to produce filters and beam splitters for far-infrared spectrometers [122]. Ulrich was the first to recognise that these devices, along with their complementary structures, could be described as capacitive or inductive grids, using single element equivalent circuits to describe their behaviour [123]. His work in 1974 however, was arguably the first to recognise the effects of SPPs on metallic meshes [124, 125]. Ulrich recognised the presence of surface waves on these structures, attributing the effects to so called Zenneck waves (discussed in section 4.6.1). Not only did Ulrich demonstrate how to couple to the fundamental (0, 0) SPP modes by use of a prism grating (a mode he calls 'non-leaky'), but he also recognised the presence

of higher order 'leaky' modes - now attributed to higher order, dispersive ($\pm$i, $\pm$j) modes detailed in section 4.6.4.1. Ulrich also recognised that: the dispersion of the fundamental mode was modified by the presence of the periodic mesh, a coupling existed between the 'leaky' and 'non-leaky' modes, and that the coupling could be established either side of the mesh in symmetric and asymmetric forms. This was neatly surmised by Ulrich, stating the surface waves "can be understood as Zenneck waves propagating on both sides of the mesh, being coupled and perturbed by the periodic perforation" [125].

Metallic meshes continued to be investigated for their uses as high-pass and dichroic filters in the terahertz region for many years [126, 127], however, since the advent of the work by Ebbesen, focus has been turned to the study of the fundamental properties of SPPs as opposed to potential applications.

### 4.6.1 Fano modes, Zenneck waves and SPPs

Ulrich was the first to state the role of surface waves in the reflection and transmission properties of two-dimensional sub-wavelength aperture arrays in the far-infrared; referring to these as 'Zenneck waves'. Surface waves (otherwise known as guided waves) can exist in many guises, with nomenclature nuances often being the distinguishing factor, as opposed to any real physically defining differences. Surface waves exist at the interface between two dielectrics whose real parts of the dielectric constant are of opposite signs. Fano modes [126] exist only for the case where no losses exist (i.e. both dielectric constants are purely real). Zenneck waves exist when one of the dielectrics exhibits strong absorptions. In this regime, the propagation distances of the surface wave are much greater than the wavelength used to excite them, thus they are extremely applicable to the case of very low frequency (radio) waves [128–130]. Although the propagation distances of Zenneck waves are large, the field is loosely coupled to the surface, with these waves resembling photons at a grazing angle to the metal.

For frequencies close to $\omega_{SPP}$, the frequency dependent dielectric constant of met-

als exhibits strong resonances. Conventionally, such EM surface waves are described as 'coupled modes' - a hybrid mixture of EM fields and surface excitations in the medium sustaining the resonance. To encapsulate the dependence on the surface excitations, these coupled modes are often referred to a surface plasmon polaritons (SPPs). Zenneck modes, and the idealised Fano modes, are physically the same as SPPs. All such modes rely upon the coherent oscillation of conduction electrons in the surface of a metal neighbouring a dielectric. Low frequency SPPs are interchangeably referred to as Zenneck waves due to the historical origins of such phenomena lying in radio wave propagation. Literature neglects such terminology in the visible region, where all surface waves are referred to as SPPs.

One interesting experiment rarely quoted in the literature, examined the existence of surface waves on corrugated, high-$T_c$ superconducting surfaces [131]. Above the critical temperature, the superconducting material had a dielectric constant of $\epsilon(\omega) = -8+750i$; the real part being smaller than the imaginary, i.e. $|\Re(\epsilon(\omega))| << \Im(\epsilon(\omega))$. In this regime, the dielectric constant of the material resembles that of a PEC, a consequence of which is any surface waves will be loosely coupled to the surface - displaying Zenneck wave behaviour. This was confirmed in the experiment by a pronounced reflection minimum residing close to the light line. Below the critical temperature, the dielectric constant became $\epsilon(\omega) = -1250 + 150i$, such that the real part was greater than the imaginary, i.e. $|\Re(\epsilon(\omega))| >> \Im(\epsilon(\omega))$ . In this regime, the surface waves are much more confined to the surface, and are notionally labelled as SPPs; displayed in the experiment by a broad resonance, far from the light line. This elegant experiment displayed the transition between SPPs and Zenneck waves, highlighting the loosely confined nature of the latter, the more localised nature of the former, and the complimentary existence of both. The dielectric properties of metals in the THz region lend themselves to the existence of Zenneck waves as opposed to SPPs due to their PEC classification. The following section will document how SPP activity can be induced at THz frequencies through engineering of the dielectric

properties.

### 4.6.2 'Spoof' Surface Plasmons

The idea of increasing the confinement of a surface wave dates back to the work of Goubau in 1950 [132], where details of a corrugated wire were presented in relation to transmission lines. Pendry revisited the idea of structuring a surface to increase the confinement (or permit the existence) of surface waves in the limit of a PEC in 2004, where he introduced the concept of 'spoof' SPPs [38]. He postulated that by structuring a surface with sub-wavelength corrugations, the material could be described with metamaterial analogies; metallic surfaces with dielectric apertures could be described as an 'effective medium', whose optical properties are governed by an *effective* dielectric constant. One startling property of this theory is that the plasma frequency of the effective medium is at a much lower frequency than that observed for the unstructured metal. A direct consequence of this is that surface waves can be made to exist with increased confinement at much lower frequencies. Pendry described this phenomenon by stating the structured surface may "spoof surface plasmons".

In modern literature, the presence of low frequency surface waves is often referred to as the existence of 'spoof' surface plasmons. In a simplistic view, such geometrically induced surface waves are permitted to exist thanks to the increased penetration of the surface wave into the metal, thus increasing their confinement. Physically, spoof plasmons are the same as SPPs - they require the presence of a metal-dielectric boundary, at which a coherent oscillation of the conduction electrons in the metal exists. Incident radiation with a wavelength greater than that of the dimensions of the dielectric structures cannot resolve these features, meaning the radiation sees an effective medium with a low plasma frequency.

At this point, one should highlight the two-fold importance of the periodic nature of these structures. Firstly, surface modes can only be initiated on the surface thanks to the

presence of the periodic structure providing the necessary in-plane momentum - as detailed in section 4.6.3. Secondly, the 'effective medium' which is produced as a consequence of the periodic structures, permits the tight confinement of these established modes. As one moves from the two extremes of an array of tiny apertures to a metallic wire mesh, the sub-wavelength nature of these structures can often be lost. Fundamentally however, the further decreasing plasma frequency of the effective medium, combined with the ever present periodic structure, allows SPPs to exist on meshes at increasingly lower frequencies.

As to what actually constitutes a true 'spoof' surface is still undecided in the literature. Any formal definition would require a recognition of the aperture dimensions in relation to the wavelength of the radiation used for excitation. The majority of works in the THz region have exploited only slightly sub-wavelength apertures [39, 133–135], thus a true 'metamaterial' classification cannot be justified. This, however, has not stopped references to both 'spoof' plasmons, and the work of Pendry, in the THz literature [106, 136]. Further complications arise when THz SPPs are observed using doped semiconductor substrates (whose $\omega_p$ typically reside in the THz region), structured with sub-wavelength features [133]. As planar doped semiconductor substrates can support standard SPP modes, the effect of the sub-wavelength apertures serves to create a 'spoof-like' surface, leaving an ambiguity as to what the true nature of these SPPs are. Ultimately, SPP effects rely critically on the overriding dielectric properties of the material. As it is not currently possible to establish the dielectric properties (and $\omega_p$) of a structured material, it is difficult to arrive at a formal definition. Any such statement should seek to involve the dielectric properties of the structured (or unstructured) material, whilst also involving the relative dimensions of the features to the wavelength of the radiation. Until a formal definition is arrived at, the literature will continue to paint an incoherent picture of the nature of these surfaces and their associated effects.

The implications of Pendry's work are undoubtedly far reaching, and allow not only for

SPPs to exist in regions below that of the THz, but also permit them to be controlled by the geometrical structure of the metal, as opposed to the dielectric properties of the metal itself.

### 4.6.3 Generation of THz SPPs

For the successful generation and utilisation of THz frequency SPPs, two features must be present; a launch mechanism which can impart the necessary in-plane momentum to excite SPP modes, and a surface decorated with sub-wavelength features to increase the confinement of SPPs. A variety of launch mechanisms have been reported previously in the literature, the simplest being that of a metallic cut-off (razor blade) placed in the vicinity of a metal surface [106, 137]. This technique, although initially demonstrated in the optical regime [36], lends itself well to THz experiments due to the wavelength-scale separations required for efficient excitation of SPPs. The cut-off acts as a diffraction point for incident radiation and scatters the beam, providing a substantial proportion with the necessary in-plane momentum. The inverse mechanism can be used to de-couple SPPs into free space radiation.

Sub-wavelength periodically structured materials serve as extremely efficient plasmonic substrates due to their ability to both excite and confine SPPs. One of the simplest examples of these is a bulls-eye aperture, where a single aperture is flanked by sub-wavelength periodic corrugations [138, 139]. Each corrugation serves as a diffraction point at which free-space radiation can couple to SPP modes, whilst the sub-wavelength nature of the corrugation ensures that an 'effective-medium' is established, increasing the confinement of the established SPP. The periodic nature of these structures results in an enhanced frequency transmitted through the aperture, the wavelength of which is commensurate with the period of the corrugations.

Two-dimensional periodic structures provide further mechanisms to excite and support surface plasmons. Periodic 'pitted' structures have been shown to sustain and confine SPP

modes, however, as the features are sub-wavelength in two dimensions, they no longer serve as efficient diffraction points and cannot excite SPPs effectively. In this scenario, external coupling mechanisms are required either using prisms [140] or knife edges [106]. The case of two-dimensional aperture arrays are of significant interest, mainly due to their ability to excite, sustain and confine SPP modes, whilst maintaining high levels of transmission and being relatively easy to fabricate. The following section will explore the theory, and review the work previously demonstrated for these structures in the THz regime.

### 4.6.4 Two-Dimensional Aperture Arrays

The discovery of EOT through two-dimensional sub-wavelength aperture arrays at optical frequencies [37] initiated an explosion of research surrounding this phenomenon. Such work has spanned the EM spectrum, however, a unified theory detailing the nature of EOT in metal aperture arrays still does not exist. Whilst most work has reached a general consensus that SPPs play a vital role in this observed 'anomaly', the precise nature of transmission through the array is a hotly debated topic [141–150], with some still arguing that SPPs play no role whatsoever in the process [151, 152].

Here, background theory detailing how the presence of a two-dimensional array effects the dispersion relation of SPPs will be presented. An overview of the factors currently thought to affect the transmission process will be given, with a strong emphasis on experiments conducted in THz and microwave regimes (where a PEC regime is applicable). Finally, an important point will be made concerning the wavelength of radiation compared to the dimensions of both the period of the array and aperture size, where two distinct regimes exist.

#### 4.6.4.1 Theoretical Description

When light is incident upon a two-dimensional metal aperture array with sub-wavelength apertures and periodicity, each aperture edge serves as a diffraction point at which p-polarised light can couple to SPPs. The two-dimensional lattice provides in-plane momentum in integer multiples of $2\pi/L$ in both the x and y directions. This increased in-plane momentum allows the freely propagating light to couple to SPP modes, which are subsequently initiated along the metal-dielectric boundary. The wavevector of the SPP can thus be expressed as:

$$k_{SPP} = \frac{2\pi}{\lambda} \sin\theta \pm iG_x \pm jG_y \tag{4.17}$$

Here, $\lambda$ is the wavelength of the incident radiation, $\theta$ is the angle of incidence of light on the array, $i$ and $j$ are integers whilst $G_x$ and $G_y$ are the lattice vectors in the x and y directions respectively. For the case of a square array, $G_x = G_y = 2\pi/L$, where $L$ is the period of the array. After propagating on the metal, the established SPPs are subsequently re-emitted into free space light upon arrival at another diffraction point.

The spatial periodicity of the array results in a periodicity for the wavevector of the SPP modes, which allows for Bloch wave and Brillouin zone analogies to be drawn. The folding of the Bloch wavevector at the Brillouin zone boundary results in resonant frequencies at the $\Gamma$ point that are a function of the lattice constant. Ultimately, for normal incidence, the transmission peak resonances are approximated by the following relationship, confirming the strong dependence on the lattice constant and the dielectric properties of the neighbouring dielectric [145]:

$$\lambda_{peak} = \frac{L}{\sqrt{(i^2 + j^2)}} \sqrt{\epsilon}_d \tag{4.18}$$

#### 4.6.4.2 Dispersion Curves

Dispersion curves for SPPs on a two-dimensional aperture array display transmitted resonant frequencies as a function of incident angle. The standard $(i, j)$ nomenclature corresponds to integer steps taken along the reciprocal lattice, and serve as a label for the resonances. Taking such steps in reciprocal space ultimately maps out diffraction spots, allowing an equivalence to be drawn for the observed resonances - the wavelengths responsible for a particular transmission resonance correspond to missing diffraction spots due to the wave being 'trapped' along the surface [153]. The two-dimensional nature of the periodicity results in momentum gained from the y component being projected onto the x diagram. A typical dispersion curve for a two-dimensional metal aperture array for the $\Gamma - X$ orientation can be seen in figure 4.5.

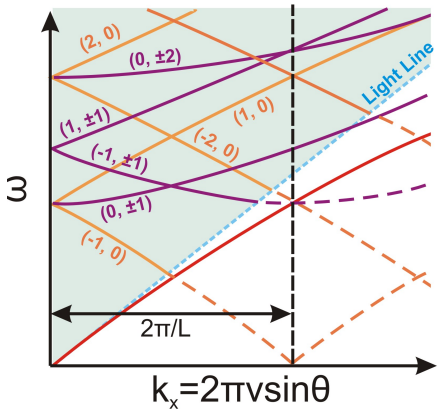


Figure 4.5: Typical dispersion curve for a two-dimensional metal aperture array for $\Gamma - X$ orientation. Orange curves correspond to momentum contributions from x periodicity, whilst purple curves display y projected momentum. Adapted from [124].

The orange curves in figure 4.5 are similar to those found for a periodic array of sub-wavelength slits, and display p-polarised characteristics only. The purple curves correspond to the momentum gained from y periodicity, which is projected onto the $\Gamma - X$ orientation. These curves display a mixture of p and s polarisation characteristics, highlighted by their flatter appearance and lack of splitting with increasing angle. At 0 ° incidence angle, multiple resonance peaks are observed highlighting how transmission can be enhanced

over a wide frequency range, even for perpendicular illumination. Clearly apparent is the fact all the higher order modes lie to the left of the light line; such modes can be excited without the need for prism coupling, i.e. they can be excited using free space light.

Two-dimensional gratings are an extremely elegant tool for both the study and exploitation of SPPs; not only does the physical structure of the array generate SPPs without need for a further coupling mechanism, but the 'dilution' of the metal with dielectric filled apertures acts to increase the confinement of the SPPs to the metal surface. The following section will examine experiments undertaken on two-dimensional aperture arrays at THz frequencies, detailing the current proposed theories for EOT and the other associated observations.

#### 4.6.4.3 Literature Review of Previous THz Studies

The first demonstration of EOT with a two-dimensional sub-wavelength aperture array at THz frequencies was undertaken by Gomez Rivas et al. [133]. From a doped silicon substrate with a plasma frequency in the THz region, aperture arrays were created using perpendicular cuts of a wafer saw on both sides of the wafer. Strong resonant peaks were observed not only at the cut-off frequency for the apertures, but more unexpectedly, for frequencies much lower than the cut-off. The position of the resonant peaks was ultimately correlated to the period of the array, whilst thinner substrates were shown to dramatically improve overall transmission. Although this work clearly demonstrated THz SPPs, the substrate would typically be expected to support standard SPP modes due to the plasma frequency residing in the THz region. The presence of sub-wavelength apertures suggests a 'spoof' surface has been created, however, the dielectric properties of the silicon, combined with the only slightly sub-wavelength nature of the apertures would suggest that the observed effects are from standard SPPs, not 'spoof' SPPs.

The work of Qu et al. however was the first to display enhanced transmission through a metallic sub-wavelength aperture array at THz frequencies [134], a regime in which

metals should classically not be able to support SPP modes due to their PEC properties. Lithographically patterned aluminium aperture arrays on high resistivity silicon substrates displayed SPP resonances for both the metal-silicon and metal-air interfaces, with rectangular apertures showing increased transmission and phase shift over their circular counterparts. Much sharper resonances have been observed for the case of free-standing metal foil aperture arrays [154], owing to the increased coupling between SPPs on the front and back of the array, as previously observed in the optical regime [146]. Here, resonances continued out to 100 ps in the time domain, displaying a long SPP lifetime and ultimately a long propagation distance. This work was also the first to test the dependence of the metal on the SPP modes by sputtering optically thick silver on the original aluminium foil. Resonances were found to appear at the same frequencies for each metal, with only a change in the magnitude of the transmitted resonance being observed. This has been confirmed in further work, where even poor conductors such as lead were found to support THz SPPs, with the transmitted intensity being dominated by the ratio of the real to imaginary parts of the metals dielectric constant [155]. Interestingly, SPP resonances have also been found to exist on metals whose thickness is less than the skin depth, with the strength of the SPP resonance increasing with increasing thickness [156].

Much work has been undertaken to find the optimum conditions for SPPs in two-dimensional aperture arrays at THz frequencies. With factors such as aperture dimensions, shape, orientation, area, period and thickness of the array all playing important roles, the degrees of freedom for such a catalogue of experiments are vast. Janke et al. were the first to analyse the effect of varying aperture shape, where square apertures of varying sizes were made in a doped silicon array [40]. Increased transmission was observed for apertures of increasing size, however the resonances became broader, alluding to a decreased surface lifetime for the SPPs with increasing aperture width. The resonances observed in this experiment differed from the predictions calculated using equation 4.18, due to the channelled grooves on the substrate, formed as a consequence of the fabri-

cation process. The presence of these grooves will dramatically alter the coupling and decoupling of SPPs and subsequent transmission through the apertures. The importance of aperture orientation has also been demonstrated [135], with elliptical aperture arrays in ultra-thin, doped silicon wafers. When the long axis of the ellipses was aligned perpendicular to the polarisation of the E-field, strong transmission was observed for frequencies well below that of the cut-off. Rotating the sample through 90° shifted the position of the resonance to higher frequencies, whilst also drastically reducing the transmission. The vast transmission for the initial orientation was attributed to the greater preservation of beam polarisation, as confirmed in [157].

Further detailed studies investigating how the aperture shape affects the transmission have been carried out using free standing metal foils [154]. Greater transmission was found to occur for non-symmetric apertures over the symmetric case. This work also displayed that as the aspect ratio of a rectangular aperture (aligned with the long axis perpendicular to the polarisation of the E-field) was increased, the relative transmission was decreased. Furthermore, results found in the optical regime, where a decreasing aperture width redshifts the resonant frequency [158, 159], were not replicated here, with the frequency remaining almost constant. Importantly, this work was the first to recognise the onset of the SPP resonance occurring after that of the direct (non-resonant) transmission. Such an analysis is only possible using time-domain techniques, where a single bipolar pulse irradiates the sample. The time-domain analysis of this resonance also serves as a measure of the lifetime (and ultimately propagation distance) of the SPPs on the surface of the metal, via either an exponential fit to the decaying oscillation in the time-domain, or the width of the resonance in the frequency domain.

Further work has analysed the effect of aperture diameter on the lifetime of SPPs [158, 160]. Miyamaru et al. [160] were the first to provide fits to the lifetimes of SPPs, showing a decrease in lifetime as the diameter of the aperture was increased. Neglecting ohmic losses due to the high conductivity of metals at THz frequencies, this decrease in

lifetime was attributed to the increased scattering cross section with increasing aperture diameter, i.e. SPPs were scattered more frequently as there was less distance between the apertures. It is interesting to point out that similar effects observed in the optical regime, where time-domain data can not be obtained, explains these observations in terms of localised surface plasmons or shape effects [143, 159, 161].

A further complication regarding the variation of aperture size is the magnitude of the coupling which is believed to exist between the SPPs and the non-resonant transmission. A detailed study by Han et al. [162] measured the transmittance of rectangular apertures with varying widths. This study confirmed the results of previous work [163] in that the normalised peak transmission decreases with increasing aperture width, however the results were found also to differ in that a redshift in peak frequency was observed with decreasing aperture width, in line with results observed in the optical regime [158, 159]. Further analysis revealed that the peak transmission initially increases, and subsequently decreases, with increasing aperture width, suggesting the existence of an optimal width. These results were interpreted using a Fano analysis. Typically, a Fano analysis provides a method to describe the coupling between a resonant and a non-resonant process, as is perceived to be the case for two-dimensional aperture arrays. Fano models have been used to effectively model experimental results in the optical regime, matching the asymmetrical resonance peaks often observed [164]. Han argues that with increasing aperture width, the degree of coupling to SPPs increases, whilst both the cut-off frequency and metal-filling fraction decreases; the latter two cases enabling a greater degree of non-resonant (direct) transmission. Furthermore, Han calculates that the coupling constant between the two regimes is found to increase with increasing aperture width. Han concludes his analysis by stating that as the aperture width is increased, the combination of the increased direct transmission, the increased excitation of SPPs and the increased coupling between these two states leads to damping of the SPPs, broadening their resonance and shifting their peak to higher frequencies. This onset of the negative impact of the direct transmission

through increasingly broader apertures offers an explanation to the 'optimum' aperture width.

There exists only one experiment in which the length of the aperture is varied whilst the aperture width and two-dimensional period remain constant [165]. With the long axis of the aperture being aligned perpendicularly to the polarisation of the E-field, as the length of the aperture is increased, a redshift of the resonant frequency is observed. The authors attribute this shift to changing resonance regimes; for short aperture lengths standard SPP modes are thought to dominate, whilst localised SPPs govern the transmission for longer aperture lengths. This classification was supported by analysing the same arrays with two differing beam diameters. The arrays with the longest apertures, where localised SPPs are thought to dominate, displayed very little change in transmission between the two beam diameters. A much greater dependence was observed for the shorter apertures, where a vast difference in transmission was observed due to the effective collecting area of the array being reduced with the smaller beam diameter.

Further confirmation of this theory was presented by observing the change in peak transmission frequency when paper was placed next to the array. The theoretical work of Bravo-Abad et al. suggests apertures of larger dimensions have a greater proportion of the E-field residing in the apertures, whilst smaller apertures have a greater proportion residing on the metal surface [166]. This suggests larger apertures should be much less sensitive to a change in the neighbouring dielectric for two reasons: firstly, any established SPP is less dependent on the surface of the metal as a smaller proportion resides there; whilst secondly, if the observed resonance is truly a localised SPP and only occurs due to the specific geometry of a single aperture, it should be almost independent of the metal surface. This was observed to be the case as the paper was introduced - the smaller apertures saw a clear redshift in frequency whilst the larger apertures saw no shift.

Miyamaru et al. investigated the finite size effect for the transmission of aperture arrays, finding that arrays with more than 20 apertures produced a good quality band pass

filter, whilst only ten apertures were enough to observe EOT [167]. The work of Matsui et al. investigated the transmission properties of random and aperiodic arrays [168]. Random arrays were found only to produce broad resonances which red shifted to lower frequencies when aperture diameters were increased, suggesting waveguide cut-off was the dominant transmission factor. This ruled out the existence of so called 'shape resonances' thought to exist for individual apertures. Aperiodic arrays, with 5, 12, and 18 degree rotational symmetry were found to produce strong, sharp resonant features with 'Fano' asymmetrical appearances. One final work of merit is that by Qu et al., who observed so called 'fractal' surface plasmons [157]. An abundance of resonances in the frequency domain was attributed to the interference between SPPs propagating in all directions on the metal aperture array. This work not only highlights the long propagation distances involved with SPPs at THz frequencies, but the unrestricted propagation directions of these excitations.

In conclusion, even with the great deal of research investigating the transmission properties of two-dimensional metal aperture arrays in the THz region of the EM spectrum, no single theory has been found which allows resonances to either be explained or predicted. THz-TDS provides an elegant method to study the lifetime and properties of SPPs, including how they are strongly affected by aperture and lattice geometries. The Fano interaction goes someway to matching the asymmetry of the resonances, yet offers no real explanation as to the mechanisms involved with the coupling interaction on which it is based. Any theory looking to explain the EOT anomaly must be able to explain, amongst other factors, the observed blueshift and broadening of a resonance with increasing aperture width parallel to the polarisation, the redshift and broadening observed as aperture length perpendicular to the polarisation is increased, the change in frequency associated with a change in period and the reason random arrays of apertures produce no resonance. An elegant theory encompassing all of these occurrences will be presented in chapter 6.

# Chapter 5

# Near-Field Imaging with Plasmonic Apertures

## 5.1 Introduction

Since its first demonstration in 1995 [169], THz imaging has rapidly become a popular analysis tool for a variety of applications, ranging from chemical identification [29] to the analysis of industrial processes [170]. One of the major drawbacks of the technique is the relatively poor resolution one can achieve as a result of the wavelength scales involved. In a constant battle against the Abbe diffraction limit ($d \approx \lambda/2$), a variety of methods have been adopted to improve or enhance spatial resolution, including the use of wire and parallel plate waveguides [171, 172], polarisation imaging [173] and a range of near-field microscopy techniques. The latter, commonly referred to as scanning near-field optical microscopy (SNOM), can be divided into two separate techniques: apertureless SNOM, where a small tip scatters the incident radiation and acts as a near-field probe [174], and aperture SNOM, where a small hole acts as a sub-wavelength source. A variety of aperture SNOM approaches have been explored, including micromachined waveguides [175], dynamic apertures [176] and computational differential techniques [177].

As detailed in section 4.4, the transmitted intensity through sub-wavelength apertures

decreases as $(r/\lambda)^4$, limiting the dimensions of structures designed for aperture SNOM. With the continued strive towards greater spatial resolution, the benefits of using smaller apertures to improve image quality are heavily outweighed by the poor signal to noise one can achieve in practice. The use of surface plasmons as an aid to enhance THz imaging has been previously displayed in the literature, where SPPs have been used to increase transmission through sub-wavelength apertures [44, 139, 178, 179] and to improve spatial resolution through localised SPP activity [180]. The former exploitation of SPPs will form the focus of this chapter.

The realisation of 'bulls-eye' apertures, a single sub-wavelength aperture surrounded by periodic corrugations, was first demonstrated in the optical regime in 2001 [181]. The first demonstration in the THz region focussed on the time-domain properties of the transmission process, rather than exploring the potential enhanced transmission applications [138, 182, 183]. Collaborations between a selection of Japanese universities have led to the use of bulls-eye apertures at THz frequencies, with a view to improve signal to noise and spatial resolution for THz imaging purposes. These studies are based on the idea that by increasing transmission through a single sub-wavelength aperture, it is possible to move to smaller aperture dimensions, thus increasing spatial resolution whilst maintaining good signal to noise. The first of the studies reported on the transmission properties of a bulls-eye aperture with, and without, the presence of a Bragg structure to reflect SPP modes back towards the aperture [44]. In 2005, the first demonstration of the achievable spatial resolution of plasmonic apertures was presented, where resolution was improved when corrugations featured on the exit side of the aperture only [179]. Here, an average spatial resolution of 58 $\mu$m was achieved for a wavelength of 205 $\mu$m, demonstrating the validity of the technique. Further work has presented the use of bow-tie apertures to provide field enhancements, with no apparent sacrifice to spatial resolution [139].

The work presented in this chapter shows the development of bulls-eye structures for THz frequencies using a novel, versatile fabrication technique, much improved from

the chemical etching of steel plates previously demonstrated [179]. A THz QCL source is used for the experiments, chosen for the spectrally pure, intense output qualities associated with such devices. The characterisation of the beam profile exiting individual plasmonic apertures is presented, followed by THz images of a drug dispersed in a pharmaceutical drug coating, acquired using the apertures.

## 5.2 Fabrication of Initial Devices

As demonstrated in chapter 3, standard micromachining techniques can be used to fabricate devices with dimensions that are comparable to the wavelength of THz radiation. Here, a unique fabrication method employing the negative epoxy-based photoresist 'SU-8 10' was developed. SU-8 is commonly used for the creation of high aspect ratio structures [184], with one of the most common applications being microfluidic systems [185]. SU-8 becomes moderately absorbing above 1.6 THz [186], hindering its ability to create effective THz devices. Those devices which do exist, utilise the material's high aspect ratio properties to create structures which are subsequently coated in metal, negating any absorptions which would otherwise be incurred. Typical examples of these structures demonstrate applications ranging from passband filters [187] to two-dimensional photonic crystals [188]. With photoconductive antennas only producing a few $\mu$W of power, SU-8 is rarely used as a 'transparent' substrate in THz-TDS arrangements. The high powers associated with QCL sources, however, allow for large signals to be detected after transmission through relatively thin layers ($\approx 10$ $\mu$m) of SU-8.

A novel fabrication process was proposed to create the bulls-eye structures using SU-8. The design consisted of concentric SU-8 rings on a resistive (THz transparent) silicon substrate. A sputter coating of metal applied to the structure would allow an aperture to be defined, and for SPP modes to be generated and sustained due to the corrugated structure. Figure 5.1 displays how the device is designed to be used for near-field imaging.

The THz beam is focussed onto the silicon wafer, passes through the SU-8 layer, and arrives at the metal surface where SPPs will be excited.

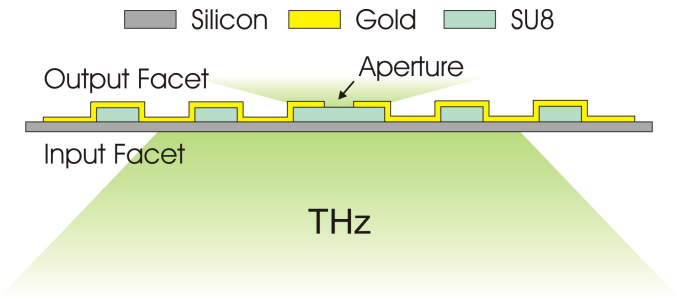


Figure 5.1: Schematic of the initial bulls-eye apertures.

Transmission through the aperture occurs via direct transmission, and secondary SPP transmission. Although relatively simple to fabricate, these structures have three main drawbacks; the THz beam has to pass through the moderately absorbing SU-8 layer, a different metal-dielectric boundary exists on both sides of the aperture, and the corrugations exist with an aperiodicity either side of of the device. These final two drawbacks lead to reduced front-to-back SPP coupling, reducing the efficiency of the SPP transmission. Despite the above deficiencies, the ease of fabrication of the devices with SU-8 offers a cheap alternative to costly deep reactive ion etching (DRIE) which would be required to fabricate the devices solely out of silicon.

Devices featuring 11 concentric corrugations with a period commensurate with the wavelength of the 2.75 THz QCL source (109 $\mu$m) were designed. A range of devices were fabricated with apertures being defined in the metallic layer, located in the central corrugation. Aperture diameters ranging from 110 to 20 $\mu$m were used for the initial experiments. To create the devices, a 10 $\mu$m thick layer of SU-8 was spin-coated on a resistive, 300 $\mu$m thick silicon substrate (3000 rpm, 30 s). A two step bake consisting of 2 minutes at 65 °C followed by 5 minutes at 95 °C was carried out prior to UV exposure, where a constant energy of 150 mJ cm$^{-2}$ was used. A UV filter was placed above the mask to minimise the exposure of the SU-8 to UV radiation with a wavelength less than 350 nm. Such filtering reduces the occurrence of negative sidewalls and alleviates 'T-topping'

of the resist. A post-exposure bake of one minute at 65 °C followed by two minutes at 95 °C was carried out prior to development in EC (Ethylene Glycol) solvent for three minutes. After development, a metal coating consisting of 20 nm of titanium (seed) and 150 nm of gold was sputter coated onto the devices. A final lithography step allowed the apertures to be defined in the metal, situated at the centre of the devices. A selection of SEM images of one of the final devices can be seen in figure 5.2. This lithographic technique provides many benefits over previously demonstrated fabrication methods, allowing bulk production of arrays of apertures, integration with other machined elements and straight forward tuning of the corrugation period by changing a single mask.

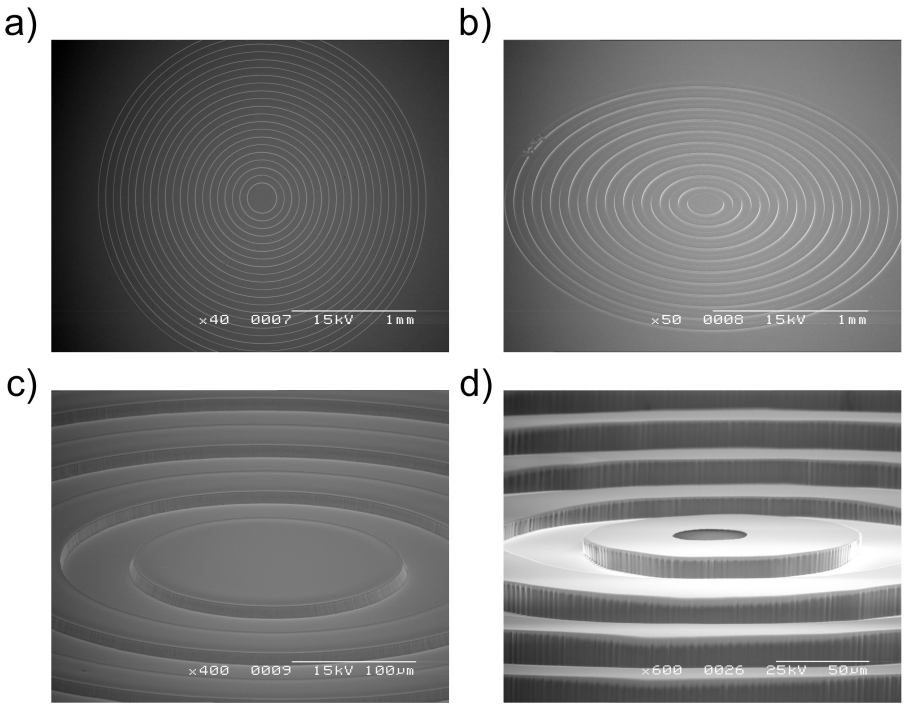


Figure 5.2: SEM images of the initial bulls-eye apertures featuring corrugations on both the input and output facets of the device. a) to c) show the SU-8 structures, whilst d) shows the final device, sputter coated in gold, with an aperture defined in the centre.

## 5.3 Spatial Distribution Tests

To assess the intensity and spatial distribution of the beam exiting the apertures, an optical arrangement, as depicted in figure 5.3, was constructed. A 90 °, 3 inch, F/2 off-axis parabolic mirror was used to collect and collimate the output from the QCL, and a 45 ° F/3 mirror was used to focus the radiation through a long focal length, whilst also ensuring a narrow beam diameter. A 2.75 THz, single-plasmon waveguide QCL was used for the experiments [189]. Single-plasmon waveguide QCLs produce well confined output beams, unlike the often divergent metal-metal waveguide designs [190]. After coarse alignment of the parabolic mirrors to a fibre optic source, the cryostat housing the QCL was moved into position. The precise location of the QCL was carefully adjusted until a spatially uniform beam profile was achieved, verified from the results of scanning a Golay cell, fitted with a macro aperture, across the focussed beam in both axes. An array of apertures with varying diameters (both plasmonic and plain) was mounted on a customised mirror mount, and attached to a 3-axis translation stage, granting 5 degrees of spatial freedom (3-axis translation, 2-axis tilt) for precise alignment of the apertures at the beam focus.

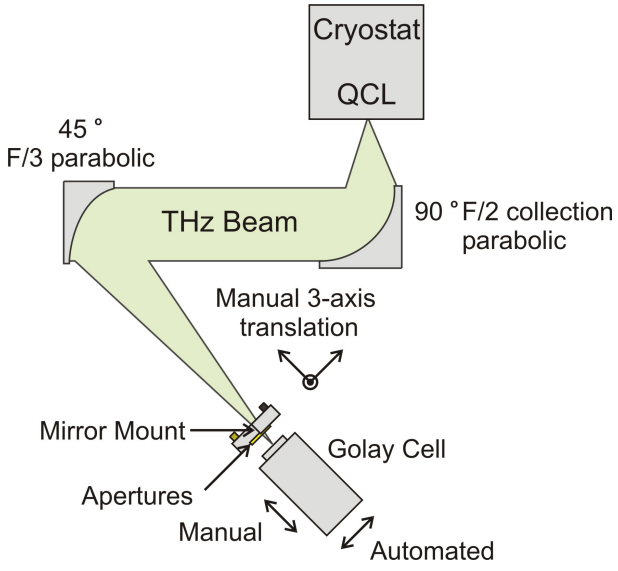


Figure 5.3: Diagram of the optical arrangement used to assess the spatial distribution of the beam exiting the aperture.

A fixed aperture-Golay separation of 5 mm was used to assess the beam intensity profile. The Golay was mounted on an automated translation stage and scanned in 20 $\mu$m steps across the exit of the aperture. Intensity readings were taken as a direct reading from the Golay cell, measured via a lock-in amplifier. The results obtained for both 65 $\mu$m diameter plain and plasmonic apertures can be seen in figure 5.4.

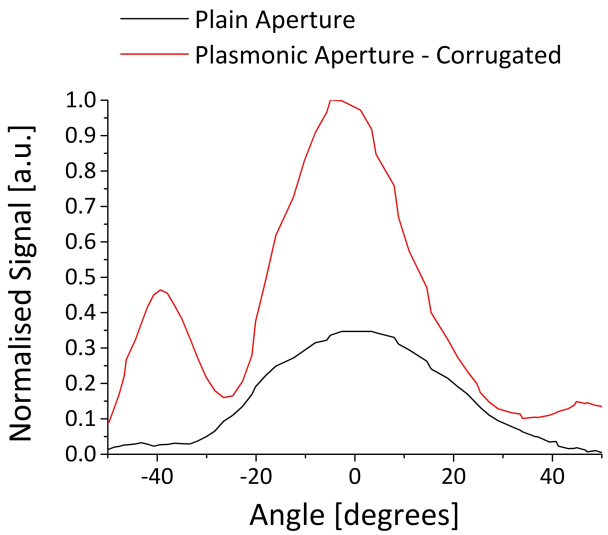


Figure 5.4: Spatial distribution of beams exiting 65 $\mu$m diameter plain and plasmonic apertures.

The results of figure 5.4 clearly show the three-fold intensity increase obtained for the sub-wavelength apertures when the plasmonic structures are present, confirming the correct choice of corrugation periodicity for the QCL source. Interestingly, the plain aperture produced a uniform intensity profile, whilst the plasmonic aperture featured two large side lobes at an exit angle of $\approx \pm 40$ °. The exact origin of these side lobes is uncertain, however it was postulated the presence of corrugations on the output facet may have led to decoupling of SPPs, fundamentally acting as further point sources. It is known that structuring of the output facet of a plasmonic aperture can be used advantageously for beam conditioning purposes [191], however, the simple fabrication procedure adopted here does not allow for such configuration. The decision was taken to adopt a 'planarised' design, adapting the previously created structures such that corrugations were only present

on the input facet of the structures.

## 5.4 Fabrication of 'Planarised' Devices

The results displayed in the previous section highlighted the possible need to remove the corrugations present on the output facet of the device. By planarising the initial devices with a further SU-8 layer (and coating in gold) however, corrugations would only exist on the input facet. Such a device would seek to improve on the beam profile demonstrated in figure 5.4, by eliminating the possible decoupling of SPPs by the corrugations on the output facet. Furthermore, the planarising layer would reduce the possible out of phase interference from front-to-back coupling of SPPs which will undoubtedly have occurred on the initial devices, hindering their performance.

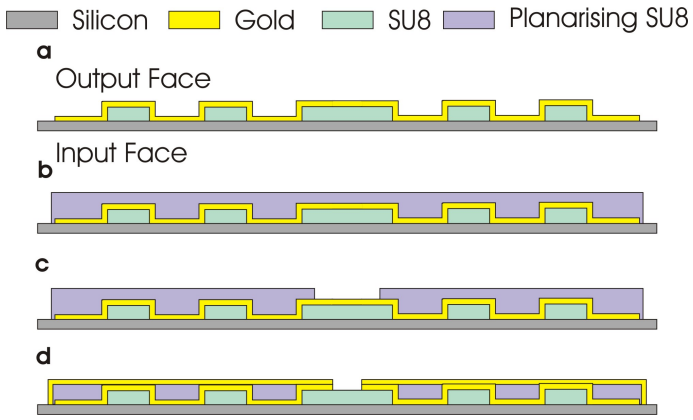


Figure 5.5: Fabrication process for the planarised bulls-eye apertures.

To create the planarised devices, the same processing was used to create the corrugated SU-8 structures as before, without defining the apertures (fig. 5.5a). A process trial was undertaken to find the best method of planarising the corrugations. A layer of SU-8 was spin coated over the devices (3000 rpm, 30 s), and left to rest for one minute, before a further layer was deposited and spun (fig. 5.5b). Initial spin conditions of 3000 rpm, 50 s, were found to produce a planarised layer with substantial thickness (figs. 5.6 a & b). Increasing the spin speed to 3500 rpm greatly reduced the layer thickness whilst

maintaining a flat, uniform layer (figs. 5.6 c & d). If the spin speed was increased further however, the layer no longer remained flat, sagging in the regions between corrugations. It was decided that spin conditions of 3500 rpm would be used in conjunction with an RIE etch to thin the layer down to match the topography of the original corrugations.

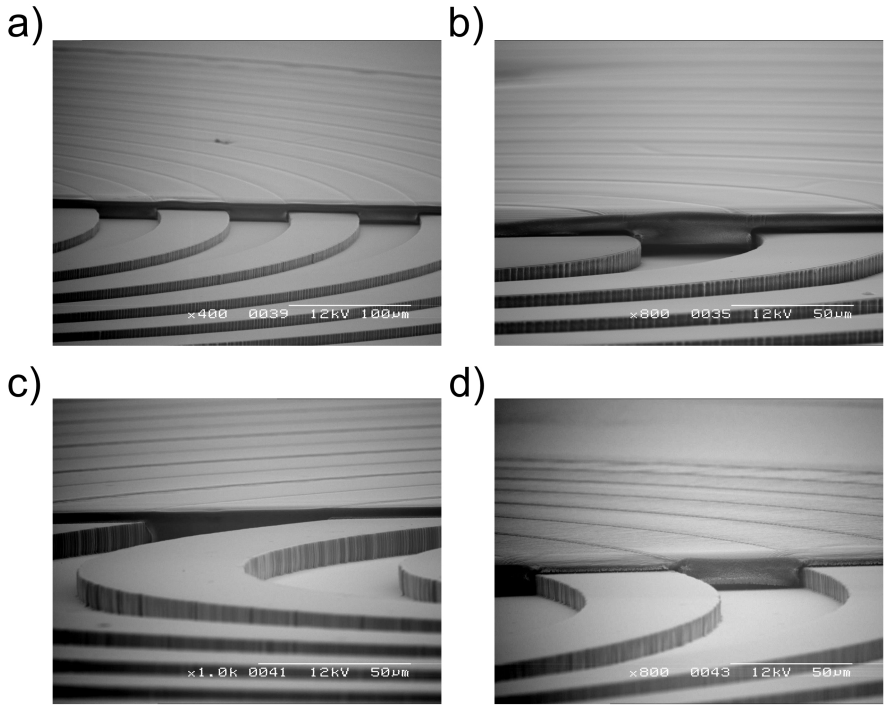


Figure 5.6: SEM images of the planarisation layer. a) and b) show the layer using a spin speed of 3000 rpm. c) and d) show the reduced thickness of the layer when a spin speed of 3500 rpm was used.

After the same pre-exposure bake conditions, the SU-8 was exposed such that a 150 $\mu$m diameter region, large enough to define an aperture, was removed from the centre of the structures (figs. 5.5c and 5.7a). After developing as before, the planarised layer was thinned down to meet the height of the initial corrugations using an $O_2$, $SF_6$ plasma etch. A further process trial was undertaken to find the correct etch duration and parameters. Conditions of 150 mTorr, 200 W, 50 sccm $O_2$, 2 sccm $SF_6$, 20 °C for 4 min were found to reduce to layer to $\approx$ 1 $\mu$m above the height of the initial corrugations (fig. 5.7a). Increasing the etch to five minutes was sufficient to meet this height, effectively planarising the device (fig. 5.7b). This process introduced an unavoidable surface roughness on the

exit facet of the device, though the extremely sub-wavelength nature of this roughness is not thought to hinder the device operation. After sputter coating the metals on the planarisation layer, the apertures were redefined using two subsequent etch steps (fig. 5.5d). An SEM image of the planarisation layer with a defined aperture can be seen in figure 5.7b.

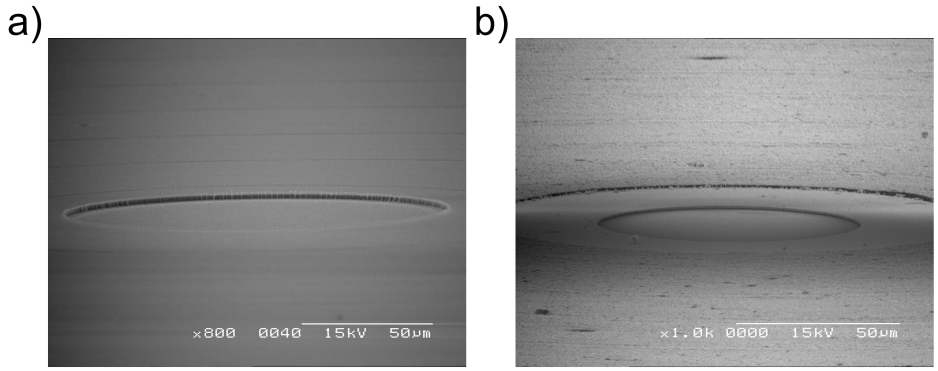


Figure 5.7: SEM images of the planarised bulls-eye apertures. a) shows the layer after a 4 min RIE etch. b) shows the planarised layer after a 5min RIE etch, sputter coating of metals and creation of an aperture.

## 5.5 Beam Profiles of 'Planarised' Devices

An identical optical arrangement as used in section 5.3 was adopted to test the beam profile of the planarised devices. Figure 5.8 shows a typical result, with comparison to the plain and corrugated devices presented previously.

The benefits of the planarisation layer are clearly evident. Transmission is seen to increase for the planarised devices when compared to both the corrugated and plain apertures. Clear detectable signals could be achieved with apertures as small as 30 $\mu$m diameter, compared to 60 $\mu$m for the plain. The result that the planarised devices displayed greater transmission than the corrugated structures conflicts with data previously presented in the literature, where double corrugated devices showed an overall increase in transmission [179]. This discrepancy is thought to arise from the periodicity of the

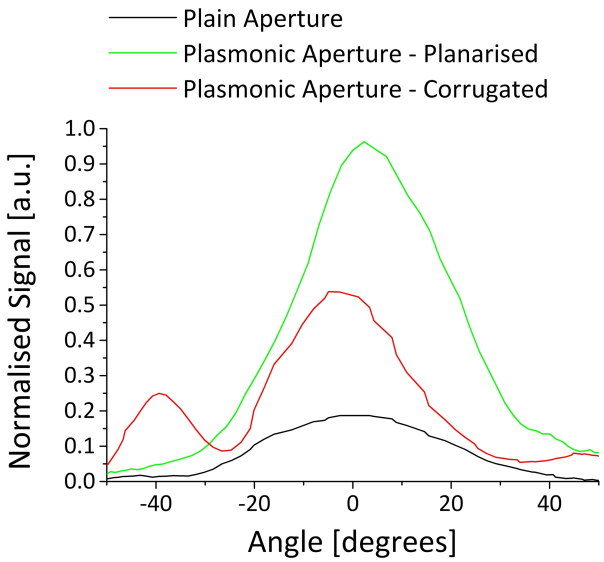


Figure 5.8: Spatial distribution of beams exiting 65 $\mu$m diameter planarised, corrugated and plain apertures.

corrugations either side of the aperture in the corrugated devices. Here, aperiodic corrugations exist either side of the device. Destructive interference from out of phase SPP activity will undoubtedly occur, reducing front-to-back SPP coupling and overall transmission [138, 192, 193]. The devices presented in [179] however, feature identical periodicities either side of the device, supporting the observed increase in transmission due to strong front-to-back SPP coupling.

A clear Gaussian like distribution was demonstrated with the planarised devices, with no evidence of side lobes. The comparable beam waist of the planarised device compared with the plain aperture shows the validity of this technique; transmission through an aperture of equal size is dramatically increased by the periodic corrugations, with no sacrifice to the beam quality.

To assess the achievable spatial resolution of the apertures, simple knife-edge experiments were conducted. A knife-edge aperture separation of 60 $\mu$m was achieved, this distance being verified by the image from a CCD mounted directly above the arrangement. The knife-edge was scanned in front of the aperture in 1 $\mu$m steps until no further signal could be detected. A 10 % - 90 % criteria was used to quantify the spatial resolution.

A typical example of the results from the knife-edge experiments can be seen in figure 5.9. Spatial resolutions of 5 to 10 $\mu$m greater than the diameter of the aperture were routinely achieved. Worthy of note is the field enhancement which occurs prior to the knife-edge impinging on the aperture. Similar features have been reported previously in the literature [179, 194], however, the exact cause of this feature is unknown. Possible explanations are a reflection of the beam by the metallic knife-edge, or a decoupling of SPPs caused by the near-field proximity of the blade.

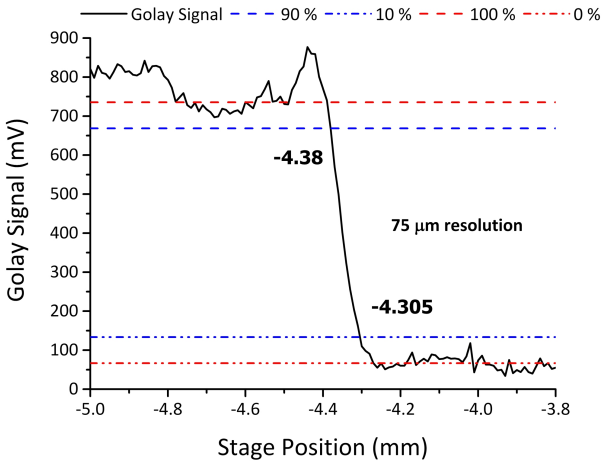


Figure 5.9: An example of the results obtained from knife-edge experiment displaying 75 $\mu$m resolution from a 70 $\mu$m diameter aperture.

## 5.6 Imaging Results

With the apertures fully characterised, a series of imaging experiments were undertaken. THz images of a series of commercial pharmaceutical drug coatings (Opadry II Clear), fabricated under a variety of drying conditions, were taken. Free standing films were fabricated by casting the polymer at 43°C for 2 hours, before mounting on metallic washers. Further samples featured quartz carrier substrates, half of which were covered with spray deposited films of the polymer. Finally, a cast sample mixed with a crystalline drug compound was also imaged, with a view to highlight absorption differences related to the crystalline/amorphous regions present in the sample. Absorption coefficients of 55

and 100 $cm^{-1}$ at 2.75 THz were measured for the drug and polymer respectively using a THz-TDS arrangement. The final cast films had a typical surface roughness of 5 $\mu$m, measured using a Talystep profilometer. A modified optical arrangement was used for the imaging experiments, where a four parabolic system was adopted (as seen in figure 5.10). This layout increased the space available to mount and raster scan the samples in the near-field of the aperture, negating the spatial constraints associated with Golay positioning experienced with the two parabolic arrangement. The longer optical path length, combined with the fact the QCL emitted on a known water vapour absorption line [195], resulted in the whole arrangement being encased in a nitrogen purged, metallic dry box, to negate these absorptions as much as possible.

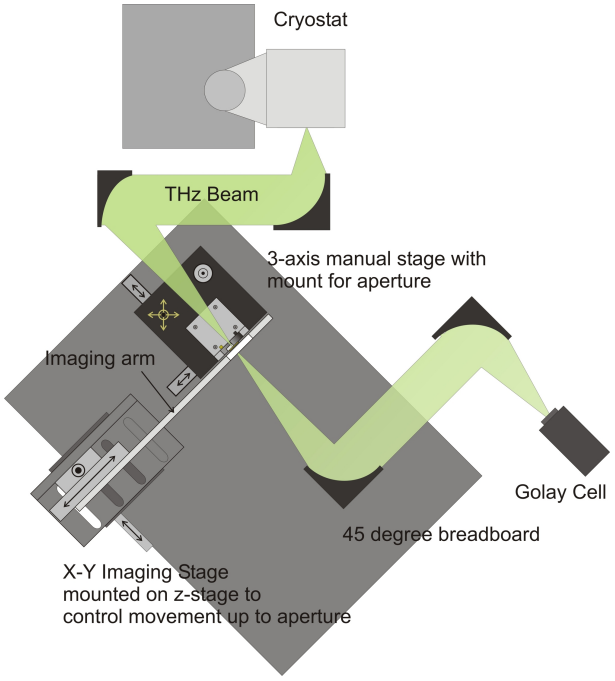


Figure 5.10: Diagram of the optical arrangement used for the near-field imaging experiments.

Samples were mounted on an aluminium plate fastened to a vertically mounted automated X-Y translation stage arrangement. Images from a CCD mounted over the arrangement allowed the sample-aperture distance to be measured accurately; the separation being controlled by a manual translation stage positioned underneath the X-Y stages.

Aperture-sample separations of 80 $\mu$m were typically used for the experiments, whilst an 80 $\mu$m diameter aperture was used for all the results presented below. A LabView program was written to automatically raster scan specified areas with user controlled step sizes. The Golay signal was recorded at each point and outputted to a data file which was subsequently read by a custom MATLAB code to plot the intensity data. Each data point took $\approx$ 3 seconds to acquire. This time period, combined with the time associated with stage movement, meant large area scans were time consuming.

The circular nature of the metallic washers used for mounting the samples was sharply reproduced in each image, providing ideal reference points for the THz images. Figure 5.11 shows an example of the type of image obtained for the samples, showing the reproduction of the washer confines. The large region of high intensity corresponds to where no film was present, demonstrating the absorbing nature of the samples. A scaled version of this image allows the slight inhomogeneities in the cast samples to be identified (figure 5.12).

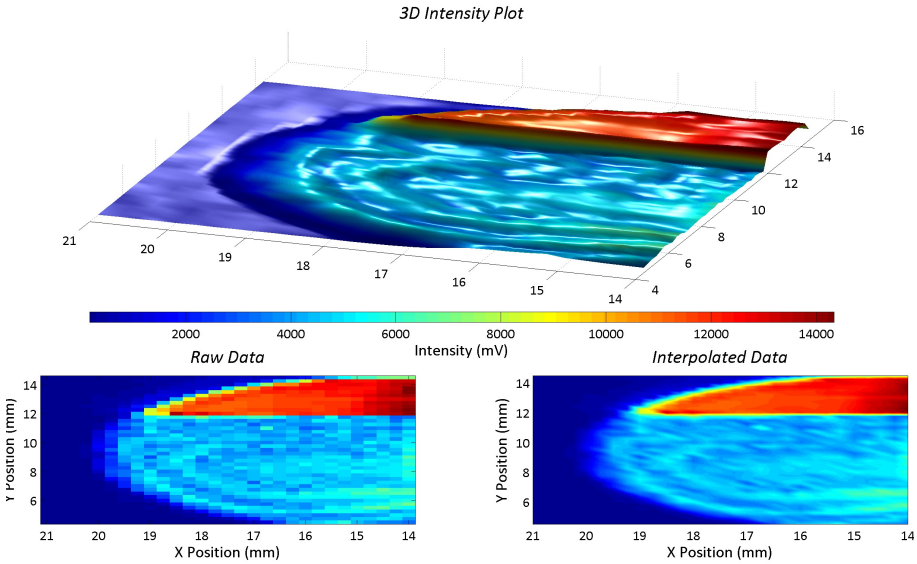


Figure 5.11: Typical THz image obtained for a cast sample using 80 $\mu$m diameter planarised plasmonic aperture.

The THz image shows the film to be moderately homogeneous in nature, with only small variations in the detected signal over the whole area. Regions of higher transmission can be seen to follow circular paths, mimicking the shape of the washer. This is thought

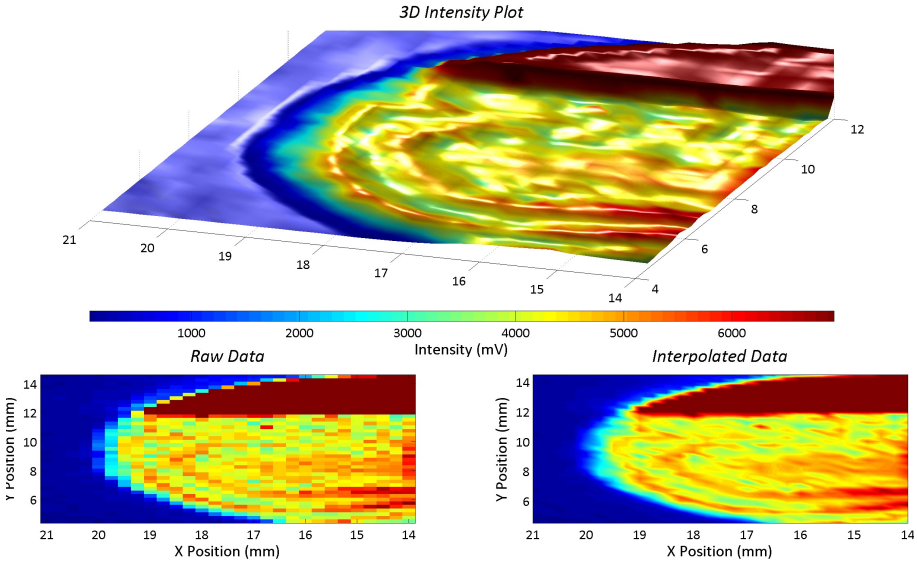


Figure 5.12: Intensity scaled version of figure 5.11, highlighting slight inhomogeneities in the cast sample.

to arise from slight damage to the film during mounting, where the sample will more than likely have been stretched by pressure being applied in the unsupported region. The ability to image using the plasmonic apertures with high resolution however, was clearly demonstrated.

Results from the spray deposited sample can be seen in figure 5.13. Signal is much reduced for this sample when compared to that in figure 5.11 due to Fresnel reflections from the quartz substrate. Besides this, the signal to noise still allows for some interesting features to be observed. One can clearly see the separation between the coated and uncoated regions, along with the circular nature of the washer. The intensity variations over the scanned area show distinct absorption differences, especially when taking into account the reduced dynamic range of the detected intensities. Such variations arise from the inhomogeneous thickness associated with the spray deposition technique. With spray-coating techniques being commonplace in the pharmaceutical industry, and the growing use of time-controlled drug delivery coatings, film homogeneity and analysis has become increasingly necessary [196]. The technique demonstrated above provides an alternative method for spray deposited film analysis, with higher spatial resolution than typically

available with current methods.

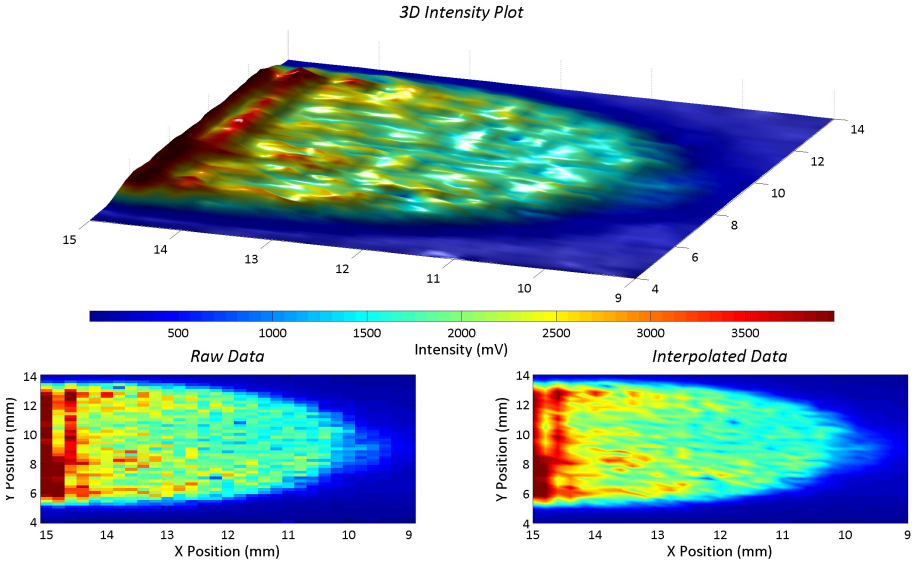


Figure 5.13: THz image obtained for spray deposited sample on quartz substrate.

A further image, featuring a cast polymer sample with a dispersed crystalline drug, was also acquired. The innate ability of THz radiation to detect differences between amorphous and crystalline samples is often exploited, in both chemical [7] and biological systems [77]. Absorption coefficients of 55 and 100 $cm^{-1}$ at 2.75 THz were measured for the drug and polymer, respectively, using a THz TDS arrangement. Only broadband absorption was observed for the crystalline drug, with no frequency specific activity. The absorption differences observed in figure 5.14 can be attributed to the distribution of the crystalline drug, and amorphous polymer regions in the sample. An optical microscope image of the same region suggests a fairly homogeneous layer should exist (figure 5.15a). When the THz image is overlaid, the validity of this technique is clearly evident; only with the THz image can the crystalline drug and the amorphous polymer regions be identified (figure 5.15b). Furthermore, such detail is only achievable with the sub-wavelength spatial resolution achieved using the plasmonic apertures. Finally, figure 5.16 shows the results from a 50 $\mu$m step size scan of a region of high intensity (top left of fig. 5.14), displaying the extremely fine detail which can be achieved if small step sizes are taken. With lengthy acquisition times (of the order of one hour for fig. 5.14 for example), large area scans on

such scales are unfortunately not feasible.

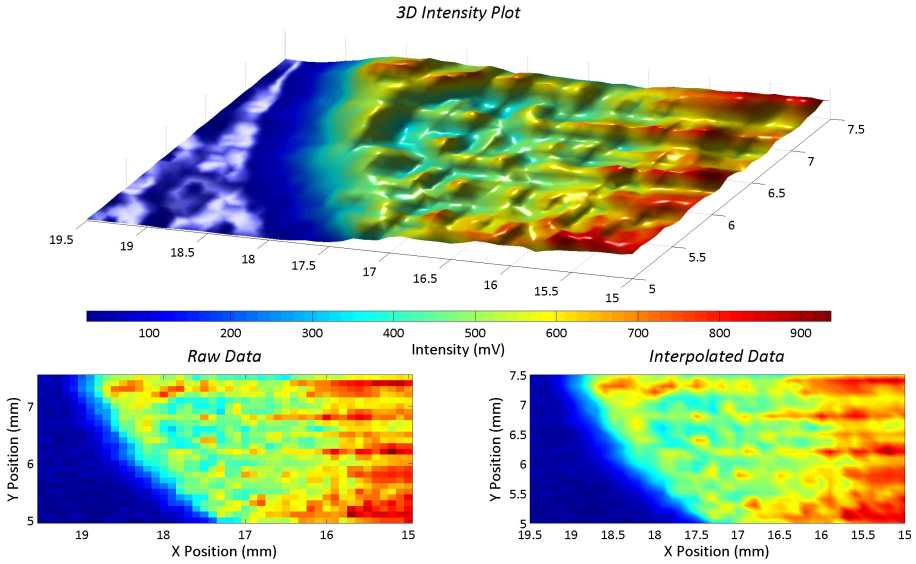


Figure 5.14: THz image obtained for a cast sample with dispersed crystalline regions, identified by the areas of low transmission.

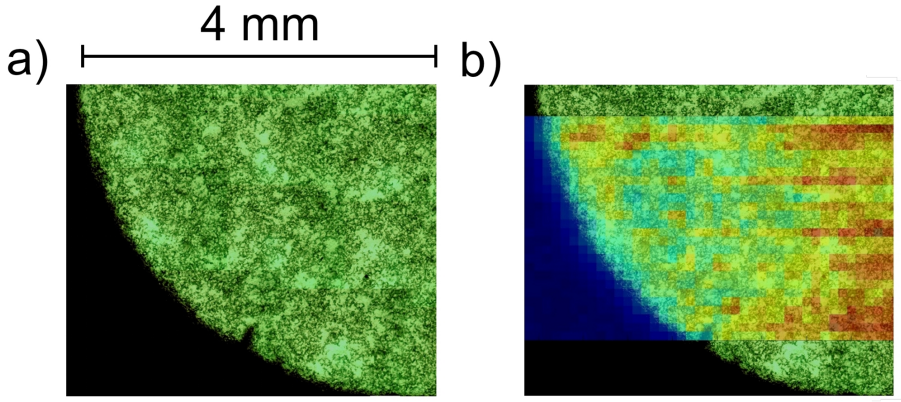


Figure 5.15: a) Optical microscope image of sample used in figure 5.14. b) Overlay of THz and optical images, highlighting the crystalline and amorphous regions not visible in the optical image.

In summary, the design and characterisation of plasmonic apertures for near-field THz imaging purposes has been presented. The technique proved to be reliable and robust, with little fluctuation in signal over the course of a full scan. While the raster scanning technique used did produce some minor 'streaking' due to noise fluctuations, the main source of the intensity fluctuations were clearly due to the sample. Spray deposited samples were found to produce inhomogeneous layers, whilst cast samples are, on the

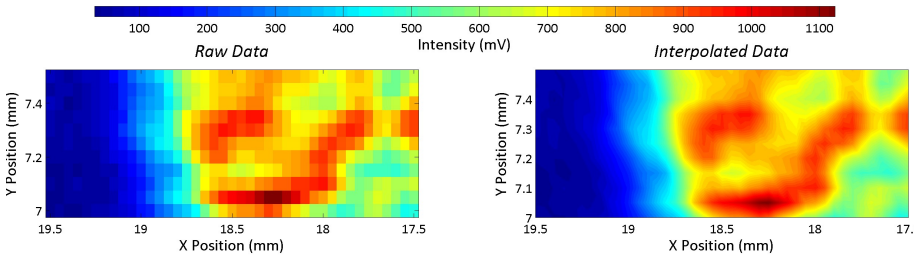


Figure 5.16: Detailed THz image acquired using 50 $\mu$m steps displaying the fine detail which can be achieved with this technique.

whole, uniform in nature. The inclusion of a crystalline compound in the amorphous polymer is clearly evident in the THz image, although indistinguishable under an optical microscope.

# Chapter 6

# Two-dimensional Aperture Arrays

## 6.1 Introduction

The mechanisms and equations describing the EOT of radiation through two-dimensional aperture arrays were presented in chapter 4. Studies of these structures in the THz (or FIR) region date back to the work of Ulrich in 1966 [123]. As detailed in section 4.6.4, further work by Ulrich in 1974 was the first to point towards the existence of surface modes to explain the transmission properties of such structures [125]. More recent literature supports the view that the extraordinary transmission is surface plasmon assisted, confirmed by the temporal waveforms acquired by THz-TDS studies [133, 134]. The review of THz studies on two-dimensional aperture arrays presented in section 4.6.4.3, found that the literature still upholds a range of theoretical interpretations describing the transmission process. Surface plasmon lifetime considerations [160] and Fano-type interpretations [162] are the two predominant contesting theories, however neither can be used to explain all the observed effects. Any unified theory must be able to explain: the blueshift observed with increasing aperture width, the observed redshift with increasing aperture length, the broadening of resonances as aperture area is increased, and the preferential alignment of apertures - in which the long axis of the aperture being aligned perpendicular to the beam polarisation produces the strongest resonances. It is strikingly

| Reference | Period ($\mu$m) | Aperture Shape | Aperture dimensions ($\mu$m) | Array | Material | Observed Metal-Air Resonance (THz) |
|---|---|---|---|---|---|---|
| J. G. Rivas et al., [133] | 400 | Square | 70 × 70 | Square | n-type silicon | 0.75 |
| Qu et al., [134] | 160 | Rectangle, Circle | 80 ×, 100 ⊘ | Square | Aluminium on silicon | 1.88 |
| Qu et al., [157] | 60 | Rectangle | 15 × 30 | Square | Aluminium on silicon | 5.00 |
| Yoshida et al., [197] | 254 | Square | 180 × 180 | Square | Free-standing metal | 1.18 |
| Yoshida et al., [198] | 120 | Square | 85 × 85 | Square | Free-standing metal | 2.50 |
| Miyamaru et al., [199] | 1130 | Circle | 680 ⊘ | Hexagonal | Free-standing metal | 0.27 |
| Miyamaru et al., [200] | 1000 | Circle | 500 ⊘ | Hexagonal | Free-standing metal | 0.30 |
| Miyamaru et al., [167] | 1130 | Circle | 680 ⊘ | Hexagonal | Free-standing metal | 0.27 |
| Miyamaru et al., [165] | 500 | Rectangle | 150 x 190, 210, 260, 310, 450 | Square | Free-standing aluminium | 0.59 - 0.35 |
| Yoshida et al., [41] | 76.3 | Square | 53 × 53 | Square | Free-standing metal | 3.93 |
| Miyamaru et al., [160] | 1130 | Circle | 500 - 800 ⊘ | Hexagonal | Free-standing aluminium | 0.288 - 0.252 |
| Azad et al., [156] | 160 | Rectangle | 100 × 80 | Square | Metal on silicon | 1.88 |
| Azad et al., [135] | 160 | Ellipse | 75 × 45 | Square | n-doped silicon | 1.60 |
| Han et al., [162] | 160 | Rectangle | 120 × 40 - 140 | Hexagonal | Aluminium on silicon | 0.49 - 1.63 |
| Han et al., [42] | 160 | Rectangle | 80 × 100 | Square | Aluminium on silicon | 1.95 |
| Tian et al., [201] | 500 | Circle | 250 ⊘ | Hexagonal | Free-standing stainless steel | 0.6 |
| Janke at al., [40] | 400 | Square | 45 × 45 - 130 × 130 | Square | n-doped silicon | 0.58 - 0.60 |

Table 6.1: Selection of two-dimensional arrays used for THz studies.

obvious how aperture dimensions and orientations govern the transmission process. Table 6.1 displays a selection of the wide range of aperture dimensions that have been studied in the literature, demonstrating the tuning abilities of the structures.

Very few examples exist in the literature which systematically investigate the effects of aperture dimensions on the transmission properties of these structures. Those which do exist only vary one aspect at a time, for example aperture width [162], length [165] and shape [163]. This approach does not allow for complete descriptions to be formed, demonstrating why the combined effects of changing aperture dimensions are not understood.

The work featured in this chapter was motivated by the need to understand the *combined* effects of varying all aspects of two-dimensional arrays, including aperture shape, area and aspect ratio, with the ultimate aim of providing a unified model to describe the behaviour. Such a model would allow resonances to by engineered from an array design perspective, allowing devices to be fabricated with sharper resonances. Sharp resonances are desirable if these devices are to be exploited for sensor applications [42, 197, 201]. Systematic THz-TDS studies of free-standing two-dimensional electroformed copper ar-

rays has led to the development of a qualitative model which allows resonance shifts and broadening effects to be predicted. The model is based on a time-of-flight analogy, previously demonstrated for bulls-eye apertures [183]. The time-domain measurements presented below have also allowed the SPP dependence on the single-cycle THz pulse to be identified for the first time.

## 6.2 Fabrication of Free-Standing Arrays

Free-standing arrays are known to produce sharper resonances, due to increased front-to-back coupling of SPPs either side of the array [146,154]. A single metal-dielectric interface not only makes recognition of resonance modes in the frequency domain a much simpler task, but eliminates the possibility of Wood's anomalies overlapping with resonance peaks - an event possibly observed in [198]. For these reasons, free-standing metallic arrays were used for the systematic experiments. A novel fabrication technique using electroformed copper, combined with standard lithographic techniques was devised to create the arrays. To begin, a 30 nm titanium seed was evaporated onto a silicon wafer, on top of which a 80 nm gold layer was evaporated (fig. 6.1a). This metallic layer provided the electrical contact necessary for the electroforming process. A three layer photoresist process was used to patten 50 $\mu$m high isolated islands of resist (fig. 6.1b), around which copper would be electroplated to create the arrays. Resist AZ9260 was spin coated at 500 rpm for 10 seconds, followed by 50 seconds at 1500 rpm. After waiting for two minutes, the resist was baked at 95 °C for seven minutes before a one minute cooling step. This spin/bake process was repeated twice, after which an edge bead removal step was undertaken prior to a one hour bake at 95 °C. The resist was then left for 24 hours before further processing to ensure all solvents were removed from the resist. After exposure through a light field mask for 215 seconds, the resist was developed in 3:1 $H_2O$:AZ400K developing solution for approximately five minutes (until clear).

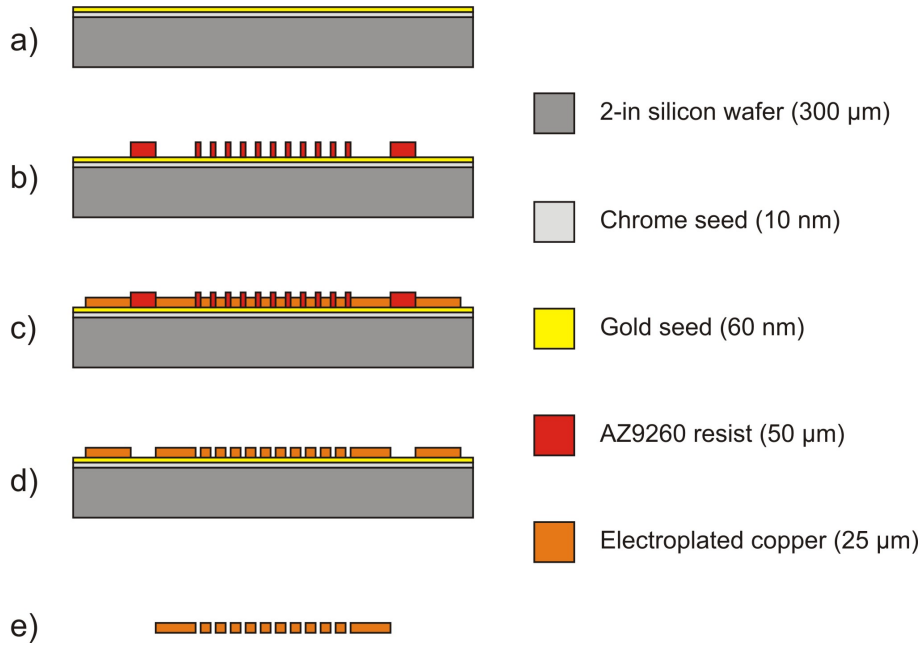


Figure 6.1: Fabrication process for the copper foil sub-wavelength aperture arrays.

Copper electroforming using a commercial copper plating solution (Via-fill 3000), sacrificial copper anode, and constant current of 45 mA created a copper foil on the gold surface of the wafer (cathode), which, after 45 minutes, was $\approx 30$ $\mu$m thick (fig. 6.1c). After removing the photoresist in acetone (fig. 6.1d), the copper foil could be peeled directly from the gold seed due to the poor adhesion between the two metals. This produced free-standing, copper foils featuring sub-wavelength aperture arrays (fig. 6.1e). Metallic regions as small as 10 $\mu$m could be fabricated between apertures, allowing a vast range of aperture aspect ratios to be created. Nine individual 1 cm$^2$ arrays could be arranged on each individual two-inch foil. SEM images showing typical examples of the foils can be seen in figure 6.2.

For the systematic experiments, it was decided that the period of the apertures would be kept constant at 300 $\mu$m, corresponding to a frequency of 1 THz, the peak frequency of the THz-TDS arrangement used. Rectangular and elliptical apertures would be studied as a function of aperture area and aspect ratio. Throughout the following sections, aperture width refers to the short axis, whilst aperture length refers to the long axis. If dimensions of apertures are quoted, the nomenclature *width* $\times$ *length* will be used. To

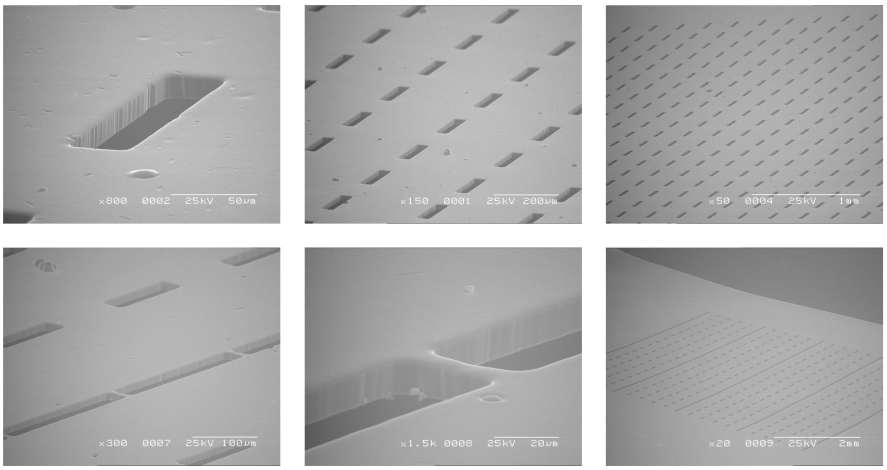

Figure 6.2: SEM images of the copper foil sub-wavelength aperture arrays.

compare results for aperture area, the total open area of each array was kept constant, i.e. arrays with larger apertures would feature fewer apertures. Aperture areas of 6400, 8100, 10000 and 14400 $\mu$m$^2$ were investigated. To compare the aspect ratio results, each individual aperture area was kept constant, with the aspect ratio changing accordingly. A typical example of the results for these structures can be seen in figure 6.3. Clearly evident is a well defined oscillation in the time domain, characteristic of a transmission at a specific frequency. This is confirmed when looking at the FFT of such a trace, where a sharp peak is observed in the frequency domain. This peak corresponds to the SPP mediated transmission, which occurs at a wavelength close to the periodicity of the array, as theoretically described in equation 4.18.

The following section will outline a proposed time-of-flight model to explain the comprehensive results of the systematic experiments presented in section 6.4. This model can be applied to square, triangular and hexagonal lattice arrangements, however, the model will be presented for a square lattice type to help to visualise and explain the effects. The experimental results presented in section 6.4 will demonstrate the effects for a triangular lattice arrangement.

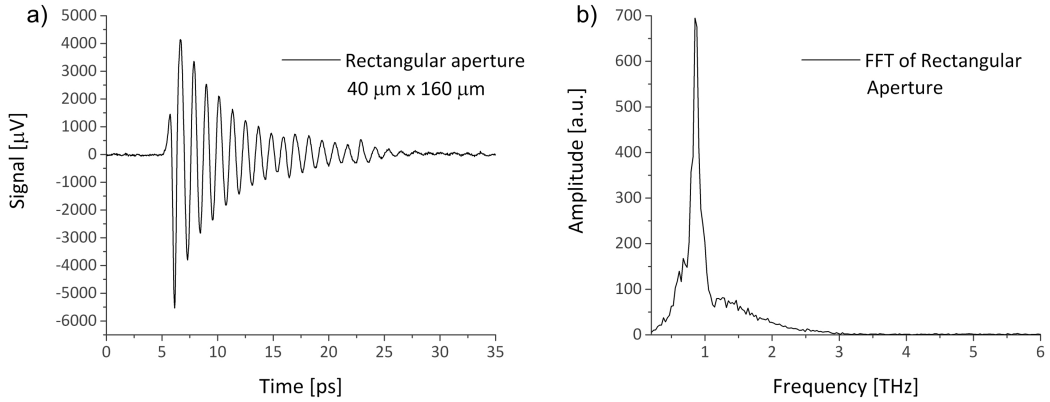


Figure 6.3: Time (a) and frequency (b) domain results from a typical copper foil array, displaying the sharp resonance obtained with the free-standing devices.

## 6.3 Time-of-Flight Model

Here, a qualitative time-of-flight (TOF) model will be outlined as a possible explanation of the observed EOT through two-dimensional arrays of sub-wavelength apertures. A similar theory has been presented for the case of bulls-eye apertures [138, 182, 183]. This model suggests the periodic oscillations observed in the time-domain are not from a coherent oscillation of the electron plasma at the metal-dielectric boundary. The authors argued the periodic oscillations occur due to periodic decoupling of SPPs at the aperture. As SPPs are initiated by the presence of the sub-wavelength periodic corrugations, those further away from the aperture will undoubtedly take longer to reach the aperture and decouple, hence, they have a longer TOF. In the same manner, SPPs initiated by corrugations residing closer to the aperture have less distance to travel and therefore have a shorter TOF. The successive decoupling of SPPs initiated by corrugations at ever increasing radii leads to the periodic oscillations in the time domain, resulting in an observed resonance in the frequency domain.

To introduce our description, knowledge of the coupling and decoupling mechanisms of SPPs is required, as well as an understanding of their propagation direction. Aperture edges act as points at which incident radiation can initiate SPPs, and conversely, SPPs can be decoupled into free space radiation. Once initiated, SPPs propagate radially away

from an aperture, with their preferential direction being parallel to the polarisation of the electric field [202]. When the SPPs arrive at an aperture edge, they decouple from the metal-dielectric boundary, and continue to propagate as free space radiation. A small proportion of this radiation is transmitted through the aperture, allowing for subsequent detection, whilst the remaining majority re-couples as an SPP on the far side of the aperture. The SPP continues along the metal-dielectric boundary, losing a fraction of its intensity from decoupling events at each aperture edge. The initiation and decoupling process is depicted in figure 6.4a.

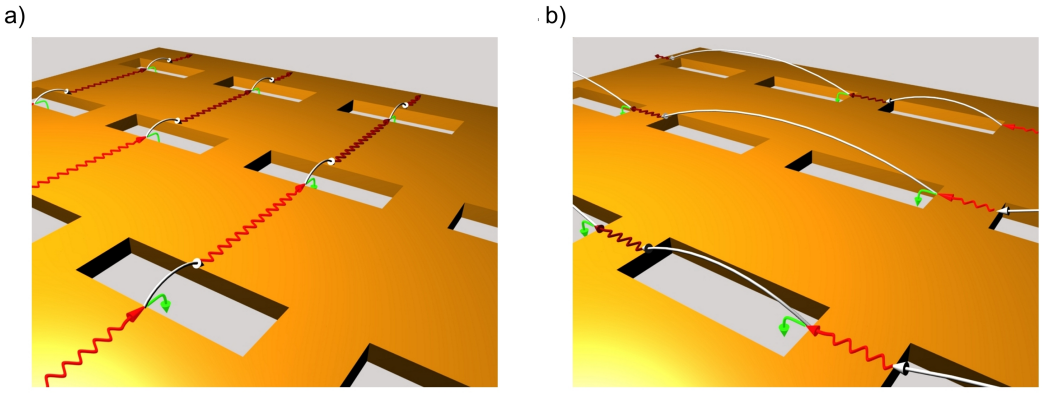


Figure 6.4: Graphical representation of the initiation and decoupling of SPPs. SPPs are represented by red arrows. Free space radiation from the decoupling of an SPP is represented by white arrows. Such radiation initiates further SPPs at subsequent aperture edges. Free space radiation from an SPP decoupling event which is transmitted through an aperture is represented by green arrows. a) SPPs travelling along their preferential direction. Successful decoupling occurs at each aperture edge, converting the SPP into free space radiation. b) SPPs travelling along their less favoured direction. As the metallic regions between apertures are so sub-wavelength compared to decoupled free space radiation, re-coupling of SPPs at nearest neighbour apertures is not guaranteed. Radiation travels to a mixture of nearest and next-nearest neighbours for re-coupling, producing multiple times of flight.

The periodic nature of the aperture array will produce periodic decoupling events, thus leading to a periodic signal in the time-domain. Furthermore, the amplitude of this signal can be expected to decay in time as the intensity of the SPPs is decreased due to multiple decoupling events along the array. The periodic signal detected in the time domain leads to a transmission peak in the frequency domain.

Aligning apertures such that their long axis lies perpendicular to the polarisation of the electric field ensures effective SPP generation in their preferential direction. This alignment also increases the chances of successful decoupling events, as SPPs propagating in the preferential direction have a greater aperture length along which to decouple. Small apertures lead to inefficient coupling of SPPs due to their extremely sub-wavelength nature, whilst decoupling is also affected as there is less chance of a successful decoupling event due to the small aperture lengths. If apertures are made too large, however, the metallic regions between the apertures become extremely sub-wavelength compared to the decoupled free space radiation. These regions no longer act as efficient points at which free space radiation from a previous decoupling event can re-couple to SPPs. In this regime, radiation travels to a mixture of nearest and next-nearest neighbours before a successful re-coupling event occurs. This process is displayed in figure 6.4b.

Having established the mechanisms required for efficient coupling and decoupling of SPPs, we can now introduce our TOF model which can be used to describe the significant effects observed when aperture dimensions are changed in both dimensions. The time taken for an SPP to decouple is determined by the distance of metal between apertures, namely $(period - width)/v_{SPP}$ where $v_{SPP}$ is $\approx$ 0.94c [107]. If the width of an aperture were to be increased, the distance between aperture edges would be decreased; thus, SPP decoupling events would be expected to occur more frequently - i.e. they have a shorter TOF. This shorter TOF will produce more frequent oscillations in the temporal waveforms, leading to a blueshift in the observed resonant frequency. For example, an increase in aperture width of 10 $\mu$m with a 300 $\mu$m period would correspond to a blueshift of $\approx$ 0.047 THz.

If the width of the aperture is increased too much however, the metallic regions between apertures become extremely sub-wavelength compared to decoupled free space radiation, thus leading to next-nearest neighbour events (fig. 6.5). This process leads to longer times between the initiation and subsequent decoupling of further SPPs, increasing its

TOF. The mix of nearest- and next-nearest neighbour events leads to a broadening of the resonant frequency with increasing aperture width due to the two competing times of flight. Such effects have been displayed previously in the literature [162], where as nearest neighbour events remained the dominant decoupling mechanism, an overall blueshift was observed as aperture width was increased. Significant broadening of the resonance was observed as the aperture width was increased further, owing to the existence of next-nearest neighbour events.

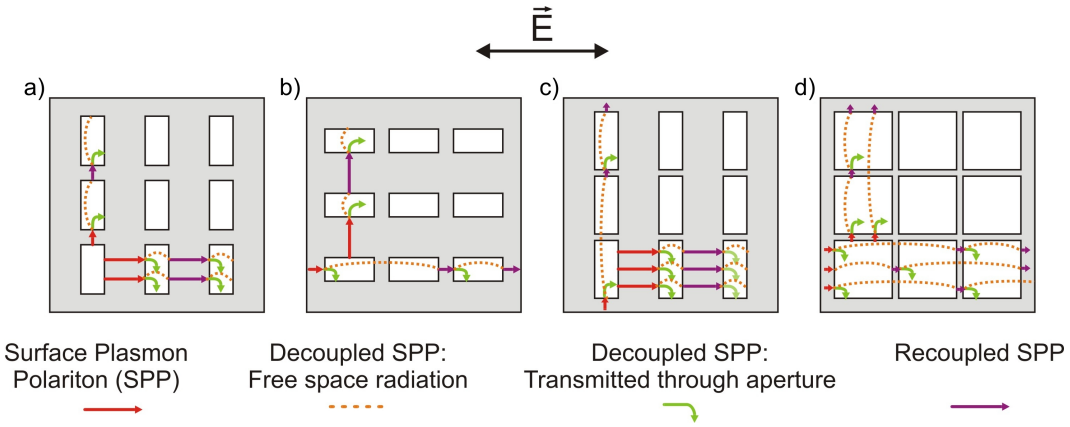


Figure 6.5: Graphical representation of the decoupling of SPPs. a) Ideal scenario where nearest neighbour events exist in both axes with good decoupling of SPPs in the preferential direction due to the large aperture length. b) Incorrect aperture orientation reduces likelihood of SPP re-coupling in the preferential direction due to small aperture lengths. Next-nearest neighbour events are also observed in the preferential direction. c) High aspect ratio apertures increase SPP decoupling in preferential direction, however only next-nearest neighbour events exist in the vertical axis, leading to a red-shift and broadening of the detected resonance. d) For extremely large apertures, next-nearest neighbour events exist in both axes leading to multiple times of flight and a distinct red-shift and broadening of the detected resonance.

As detailed above, it is essential to align the long axis of apertures perpendicular to the polarisation of the electric field. If aligned in the orthogonal direction (short axis perpendicular to E-field) SPPs travelling in their preferential direction suffer from two problems: there is only a small width on which decoupling can occur (an aperture's short axis) and the metallic regions between apertures are more likely to be sub-wavelength (fig. 6.5b). With correct alignment, if an aperture length is increased, next-nearest

neighbour events become increasingly common in the vertical direction, increasing the TOF of SPPs (fig. 6.5c). This causes both a redshift and broadening of the resonant frequency. Precisely these effects have been demonstrated previously in the literature [165]. For the case where an aperture width and length are increased simultaneously, a trade-off is established. An increase in width will result in a blueshift (and slight broadening of the resonance), whilst an increase in length will produce both a redshift and greater broadening. To engineer resonances from an array design perspective, the aspect ratio of the apertures must be altered. To produce sharp resonances, an optimum aspect ratio will exist; the aperture's width must be small enough such that nearest neighbour decoupling is guaranteed. The length however must provide the aperture with sufficient asymmetry such that SPPs travelling in the preferential direction have a large length on which to decouple, without being so long that it causes a strong redshift, and broadening of the pulse, due to next-nearest neighbour events in the transverse direction.

## 6.4 Experimental Results

The extensive experimental results presented below provide evidence to support the time-of-flight model for the case of two-dimensional aperture arrays. The results confirm those previously displayed in the literature, studying the combined effects of changing aperture shape, area, aspect-ratio and lattice arrangement on the THz-TDS temporal waveform. The detailed study serves as a design point for the THz community wishing to engineer specific resonances from such structures.

### 6.4.1 Symmetric and Asymmetric Apertures

Square, circular and regular hexagonal aperture shapes, with 6400 $\mu m^2$ areas, were tested in both square and triangular lattice arrangements. In all cases, no evidence of enhanced transmission was observed for these symmetrical apertures, even in asymmetric lattice

arrangements. The frequency domain data shows the apertures act as waveguide cut-offs, allowing less low frequency radiation through (fig. 6.6).

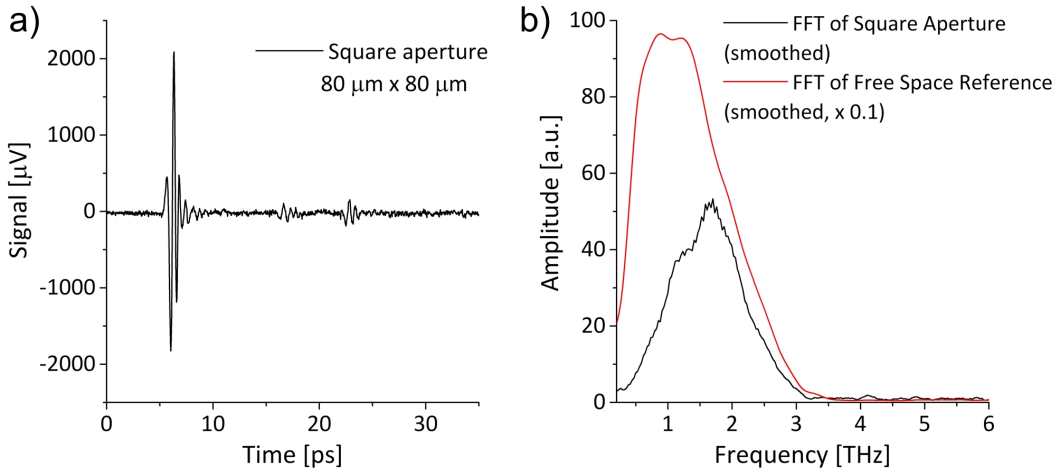


Figure 6.6: a) Temporal waveform and associated FFT recorded for the case of an 80 $\mu$m $\times$ 80 $\mu$m square aperture in a triangular lattice arrangement. b) FFT of temporal waveform with comparison to FFT of free space reference, highlighting the low frequency cutoff effect of the square apertures. Such behaviour was replicated for all symmetrical aperture shapes, irrespective of lattice arrangement.

Although not observed here, strong resonances have been displayed previously for both square [163] and circular [160] apertures in the THz regime. These studies, however, used much larger apertures than those described here (when scaled to the wavelength). Larger apertures increase the probability of SPP decoupling events, explaining the results of previous investigations. The small apertures used in this demonstration highlight the points made in section 6.3: small apertures serve as poor coupling points for SPPs due to their sub-wavelength nature; furthermore, the reduced aperture dimensions result in less common SPP decoupling, leading to poor (or even zero) SPP transmission.

Introducing asymmetry into an aperture with the same area, produced strong SPP transmission. Figure 6.3a displays a typical example of enhanced transmission exhibited by a 40 $\mu$m $\times$ 160 $\mu$m rectangular aperture array in a triangular lattice arrangement, residing on the same foil as the square aperture array displayed above. One can immediately observe a pronounced temporal oscillation, attributed to the successive decoupling of

SPPs, producing the transmission peak shown in figure 6.3b.

The exemplary resonances can be attributed to the sub-wavelength thickness of the foils, the smooth surface of the metal from the electroforming process (therefore reducing ohmic and scattering losses) and strong front-to-back coupling of SPPs due to the free standing nature of the arrays. A transmission peak is observed at 0.85 THz, with a FWHM of 0.14 THz. A characteristic Wood's anomaly can be observed at 1.14 THz, evident from the reduced transmission at this frequency. An eight-fold increase in transmission is observed for the peak frequency over that which would be assumed by taking the ratio of aperture area to array area, assuming 100 % transmission through each aperture. Realistically, the transmission increase is greater than this as 100 % aperture transmission is not achieved in practice, and instead scales with $(radius/\lambda)^4$ [115]. Furthermore, when one considers the fact that the width of the apertures is well below the cut-off for a standard waveguide, this enhancement is even more astonishing.

SPP transmission is clearly apparent with these asymmetric apertures, even though the aperture area was the same as that used in the symmetric case. The increased length of the long axis serves as an efficient point to both couple and decouple SPPs in their preferential direction. This result highlights the importance of aperture dimensions and alignment if SPP transmission is to be observed. Furthermore, this result emphasises the effect is not simply due to aperture cutoff. The square apertures presented in figure 6.6 were sub-wavelength in both dimensions, meaning any effects relating to aperture cutoff should still be evident. Instead, no enhanced transmission was observed. As EOT is only observed for the case of asymmetric apertures (where cutoff only exists in one dimension), an SPP mechanism, not cutoff effect, can be concluded.

### 6.4.2 Effects of Changing Aperture Area

The effects of changing aperture area were investigated for three different areas (8100, 10000 and 14400 $\mu m^2$) with a fixed array periodicity (300 $\mu$m), the results of which

can be seen in figure 6.7. As the aperture area is increased, the overall transmission can be seen to increase. Peak transmission can be seen to redshift with increasing area, with peaks observed at 0.79, 0.76 and 0.70 THz for the 8100, 10000 and 14400 $\mu m^2$ respectively. Broadening of the resonant peak is also observed as the area is increased, with FWHM results of 0.12, 0.16 and 0.20 THz being recorded. Considering these results from a TOF perspective, an increase in aperture width would be expected to produce a blueshift in peak transmission. Conversely, as the aperture length is increased, next-nearest neighbour events occur due to the sub-wavelength nature of the metallic regions, leading to a redshift and broadening of the peak transmission. As the aspect ratios of the apertures were kept similar, the aperture lengths were increased more than the aperture widths with increasing area. Thus, the effects of increasing aperture length outweighed those of increasing the width, explaining the observed redshift and broadening of the peaks.

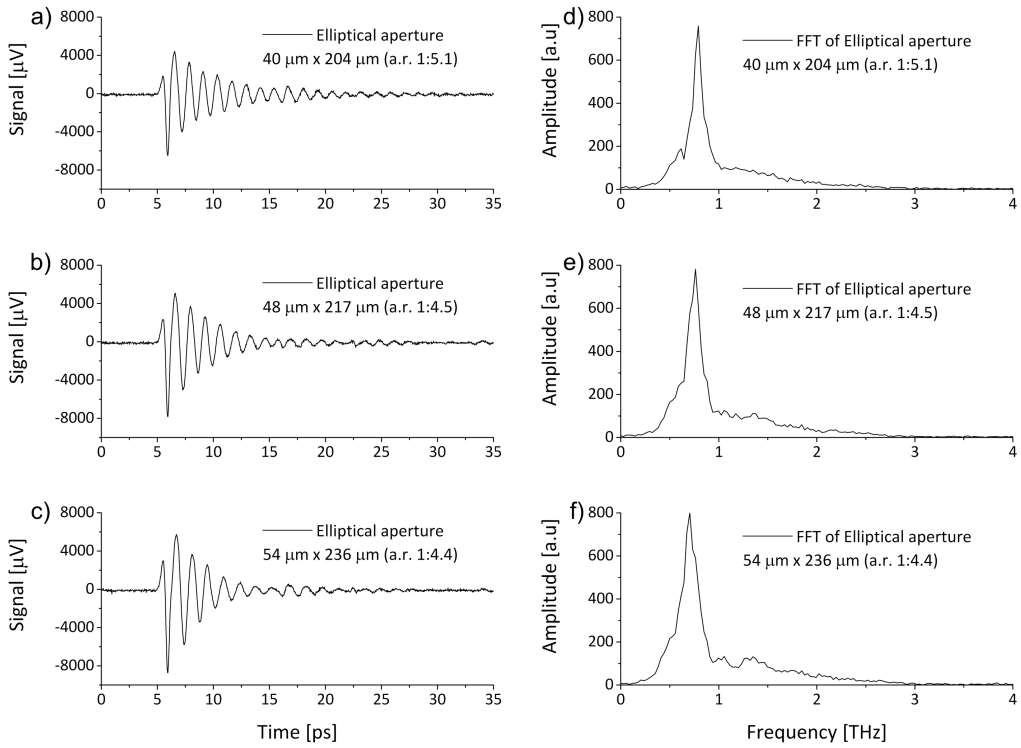


Figure 6.7: Temporal waveforms recorded for elliptical apertures in a triangular lattice arrangement with three different areas - 8100, 10000 and 14400 $\mu m^2$ (a, b and c respectively), with associated FFTs. The acronym a. r. denotes aspect ratio.

As the sum of the aperture areas was kept constant between arrays, those featuring larger apertures featured fewer apertures. This fact can be observed in the temporal waveforms. Many more oscillations are observed using smaller apertures (fig. 6.7a) compared to those with larger apertures (fig. 6.7c). Arrays with fewer apertures have less points at which decoupling can occur, hence one would expect to see fewer temporal oscillations. Furthermore, if only next-nearest neighbour events occur, there will be even less transmitted radiation, resulting in fewer oscillations in the temporal waveform.

### 6.4.3 Effects of Increasing Aperture Aspect Ratio

Further investigations were carried out to study the effects of changing the aspect ratio of an aperture whilst maintaining a fixed aperture area and array periodicity (300 $\mu$m). Elliptical apertures arranged in a triangular lattice with aperture areas of 6400 $\mu m^2$ were investigated. Aspect ratios of 1: 2.3, 3.3, 5.1, 6.7 and 9.1 were used, with the latter having just 28 $\mu$m of copper between apertures parallel to the long axis. The results are displayed in figure 6.8. Immediately apparent is the large increase in amplitude observed as the aspect ratio is increased. Peak transmission frequencies of 1.03, 0.97, 0.79, 0.76 and 0.67 THz are seen to redshift with increasing aspect ratio, further supporting the TOF model: increasing aspect ratio decreases the widths of the aperture, broadening the metallic region between apertures parallel to the short axis. This increased distance leads to greater time between successive decoupling events, and an observed redshift in the peak transmitted frequency. Furthermore, increasing the aspect ratio increases the likelihood of next-nearest neighbour events along the direction parallel to the long axis, enhancing the observed redshift.

These results display the same characteristics as those in section 6.4.2 with respect to the number of oscillations from successive SPP decoupling events. Fewer oscillations are observed with increasing aspect ratio, with the exception of figure 6.8a. Here, poor transmission is achieved with very few evident oscillations. The reason for such poor

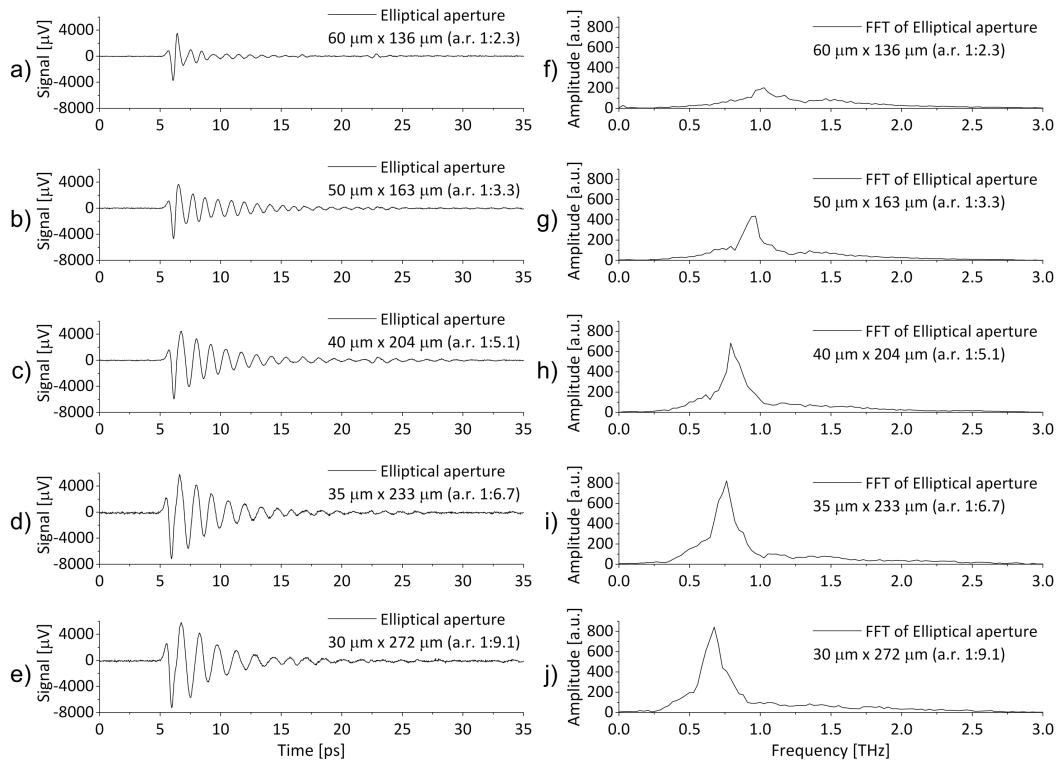


Figure 6.8: Temporal waveforms and associated FFTs recorded for 6400 $\mu$m$^2$ area elliptical apertures in a triangular lattice arrangement featuring different aspect ratios.

SPP activity is three-fold. Firstly, the apertures are extremely sub-wavelength in both dimensions meaning the apertures no longer serve as good coupling mechanisms to initiate SPPs. Secondly, SPPs which are initiated along the preferential direction have less chance of successfully decoupling due to the short aperture length. Finally, if a successful decoupling event does occur, the sub-wavelength nature of the aperture will restrict the transmission of the decoupled radiation. This result shows that a minimum size does exist for apertures when tuning resonances for a specific frequency.

## 6.5 Onset of SPP Decoupling and Dependence on Pulse Polarity

The onset of SPP decoupling has been previously identified in the literature, and is seen to occur in time after the direct transmission of the initial pulse through the apertures

[154, 160, 203]. However, such work has failed to explain why SPP transmission occurs after the main pulse, why such transmission is observed as a bipolar oscillation and how the polarity of the THz pulse dictates the propagation direction of SPPs. Analysis of the temporal waveforms and their derivatives allow the onset of SPP activity to be clearly identified. Figure 6.9 shows the temporal waveform acquired for a hexagonal array of elliptical apertures. The highly symmetrical nature of the hexagonal array was adopted to emphasise the observed effects. As in previous work, two clear regions can be identified; an initial direct transmission of the THz radiation through the aperture, followed by an oscillation from SPP transmission. The oscillatory nature of this transmission provides insight into how the polarity of each half cycle of the initial THz pulse dictates SPP propagation, analogous to how an A.C. signal demonstrates a current direction. It is argued the first half cycle of the THz pulse initiates SPPs across one direction of the array (labelled $SPP^{+}$), whilst the second half cycle, of opposite polarity, initiates SPPs in the opposing direction ($SPP^{-}$) later in time, the process being depicted in figure 6.10. When the SPPs arrive at an aperture edge, decoupling occurs, leading to a re-radiation of the THz pulse; the first half cycle of the pulse is re-radiated by $SPP^{+}$ decoupling events, whilst the second half cycle is re-radiated later in time by $SPP^{-}$ contributions. This constant decoupling from $SPP^{+}$ and $SPP^{-}$ events across the array produces the characteristic oscillatory signal in the temporal waveform.

Analysis of the first and second derivatives of a temporal waveform (fig. 6.9b), allows the onset of SPP activity to be clearly identified through its convolution with the initial THz pulse. Time $t_1$ identifies a peak in the second derivative of the temporal function, corresponding to a change in its gradient. This point in time is the onset of the first decoupling event of an $SPP^{+}$, convolved with the direct transmission of the second half cycle of the initial THz pulse. The convolution of these two processes produce the change in gradient observed in the temporal waveform. Time $t_2$ corresponds to the main decoupling of an $SPP^{+}$. Time $t_3$ identifies a further peak in the second derivative, arising from

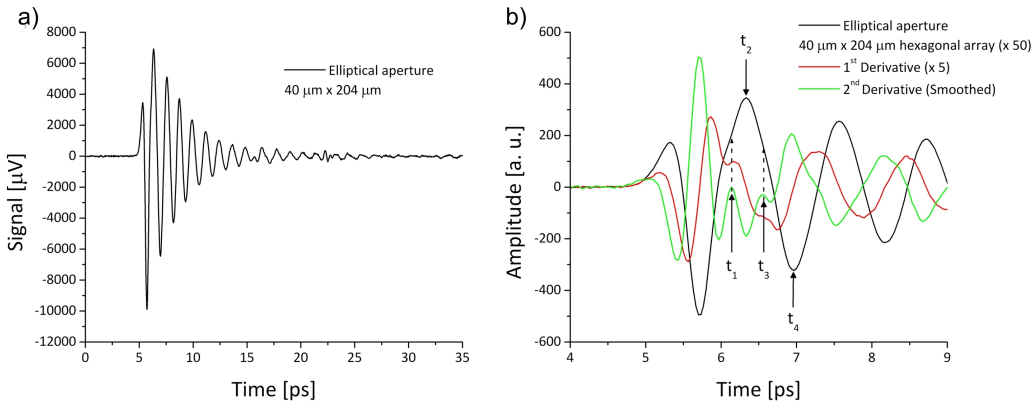


Figure 6.9: a) Temporal waveform for elliptical apertures arranged in a hexagonal lattice. b) 1st and 2nd derivatives of (a) (red and green respectively). The arrows identify the onset of SPP decoupling ($t_1$ and $t_3$), and the times of the main decoupling from $SPP^+$ and $SPP^-$ contributions ($t_2$ and $t_4$ respectively).

the convolution between the end of the first $SPP^+$ decoupling event, and the onset of the first decoupling event from $SPP^-$. Finally time $t_4$ corresponds to the main decoupling of an $SPP^-$. Subsequent re-radiation from alternate $SPP^+$ and $SPP^-$ decoupling events at apertures across the array cause the oscillatory signal in the temporal waveform.

### 6.5.1 TOF Summary

A qualitative time-of-flight model has been presented for the case of two-dimensional sub-wavelength aperture arrays at THz frequencies. This model is supported by systematic investigations into the effects of changing an aperture area, aspect ratio and shape. Oscillations observed in the temporal waveforms lead to transmission peaks in the frequency domain. Such activity can be explained as successive SPP decoupling events, not an inherent oscillation of the surface conduction electrons. This model, combined with knowledge of SPP propagation, can be used to explain all observed effects on the peak transmission frequency when changing aperture dimensions. Increasing the width of an aperture serves to reduce the propagation time of a SPP, as it requires less time to reach an aperture edge and decouple. Doing so, produces a blueshift in the peak transmitted frequency. Increasing the length of an aperture leads to next-nearest neighbour events

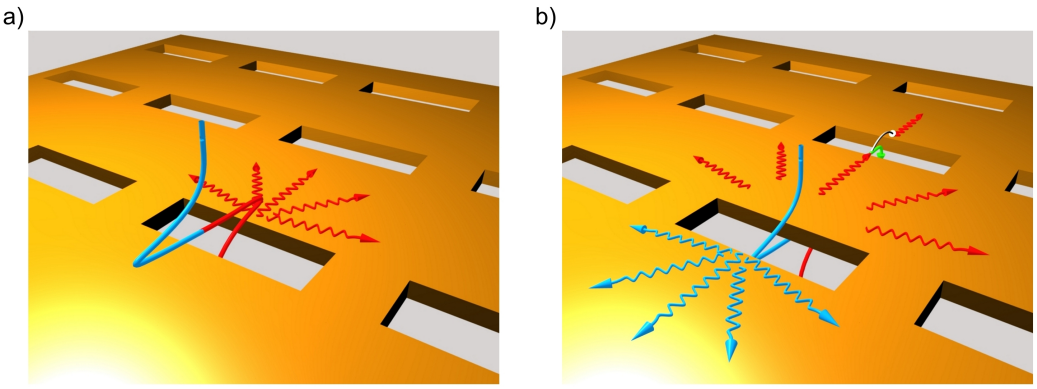


Figure 6.10: Graphical representations of the SPP contribution from a single aperture showing the propagation direction dependence on the THz pulse polarity. The red half of the THz pulse represents the first, positive half cycle, initiating $SPP^{+}$s, represented by red beams. The blue half of the THz pulse represents the second, negative half cycle, initiating $SPP^{-}$s, represented by blue beams. a) $SPP^{+}$ excitation from the positive half cycle of the THz pulse. The green beam in b) shows the first decoupling event of an $SPP^{+}$, occurring whilst the second half cycle of the THz pulse is directly transmitted.

along this direction. Such activity results in a longer time between successive decoupling events, producing an observed redshift and broadening of the peak transmitted frequency. The same line of argument also serves to explain why aperture alignment is essential; if the short axis of an aperture is aligned perpendicular to the preferred SPP direction, the SPPs have less chance of undergoing successful decoupling, next-nearest neighbour events are also induced, and minimal SPP transmission is observed. For small area apertures, correctly aligned asymmetric shapes display the best SPP transmission due to the greater decoupling of SPPs along their preferential direction. Larger apertures exhibit increased SPP transmission due to greater decoupling of SPPs in both directions along their longer aperture edges. If the aperture area is increased too much however, next-nearest neighbour events occur leading to a broadening of the transmission peak. Although this model fails to take into account any diffraction effects, which undoubtedly have a great influence on the transmission properties of these arrays, the model provides a successful analogy which correctly predicts all aspects of EOT, and its dependence on aperture geometry.

The temporal properties of SPP propagation direction and the dependence on the

polarity of the single cycle THz pulse have also been displayed. Each half cycle of the incident THz pulse initiates SPPs in opposing directions across the array. Opposing polarities are observed in the temporal waveforms due the successive decoupling of the SPPs with opposite propagation directions.

Ultimately, the thorough experimental investigation presented above, has enabled sharp resonances to be engineered for sensor applications. The copper foils may have further applications as calibration substrates for THz-TDS systems. The use of fast optical delay lines does not typically allow for the extraction of frequency specific information due to the non-linear velocity of the mirror arrangements. By determining the exact frequency response of an aperture array using standard THz-TDS techniques, placing the same array in a THz-TDS arrangement featuring a fast optical delay line may allow data extraction techniques to be calibrated to enable precise frequency domain data to be obtained.

## 6.6 Hybrid SPP Device

Extraordinary transmission has been presented for the case of periodic corrugations flanking a single, sub-wavelength aperture (chapter 5) and the work presented above demonstrated the same phenomena for a two-dimensional array of apertures. Here, a hybrid device featuring a single row of sub-wavelength apertures surrounded by periodic corrugations is presented. It was hypothesised that the commensurate periods of the apertures and corrugations would ensure that SPPs generated by either mechanism would combine in phase, demonstrating high transmission efficiencies. Such a structure is not known to have been demonstrated previously in the literature, either in the optical or the THz regimes.

To fabricate the device, a two stage electroforming process was devised, developing the process presented in section 6.2. After electroforming a single row of apertures (fig. 6.11b), a further three layer resist was spun and baked as before (fig. 6.11c). The

resist was exposed, such that isolated islands remained in the previously defined apertures, whilst also defining the corrugations (fig. 6.11d). A further electroforming step (fig. 6.11e) created the structures displayed in figure 6.12. The further bake step associated with the second resist process caused an annealing of the copper and gold layers, meaning the foil could no longer be simply peeled off the wafer. For this reason, a copper-chrome electroplating seed was used, with the device being left in 85°C KOH to dissolve the silicon wafer. A nitrogen gun was then used to remove the copper and chrome layers remaining in the apertures.

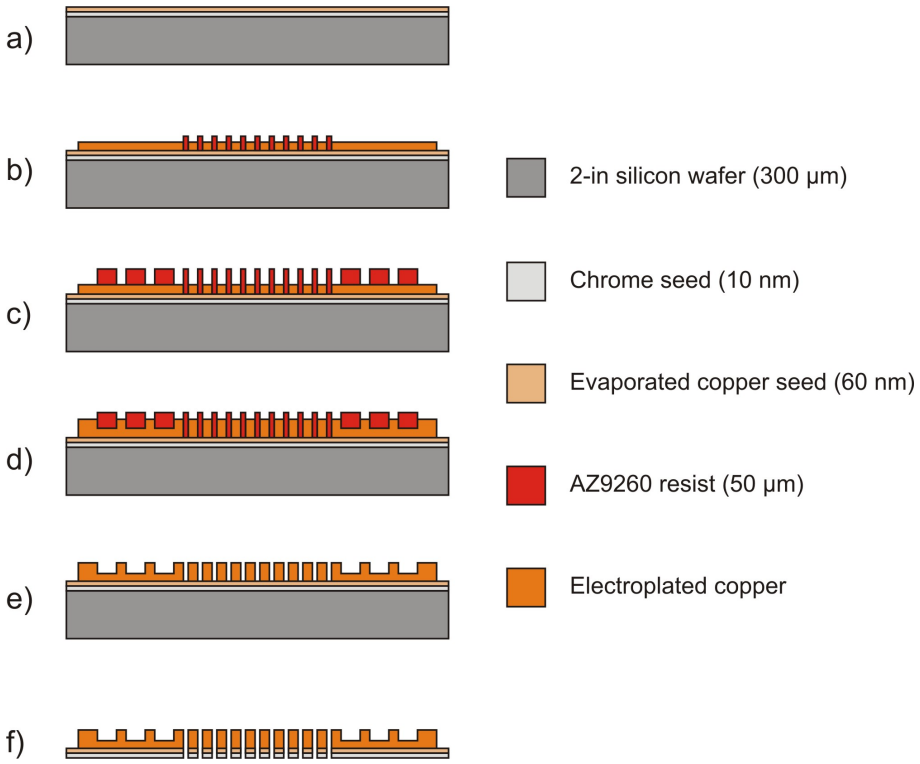


Figure 6.11: Fabrication process for the hybrid aperture array-corrugated device.

To test the devices, a single row of apertures without corrugations was placed in the THz-TDS system. Enhanced plasmonic transmission was observed, as displayed in the oscillatory green trace in figure 6.13. Although only a very small signal was detected, the transmission through this small number of apertures is astonishing considering their sub-wavelength nature.

The temporal oscillations produced a peak in the frequency domain at 0.85 THz. With

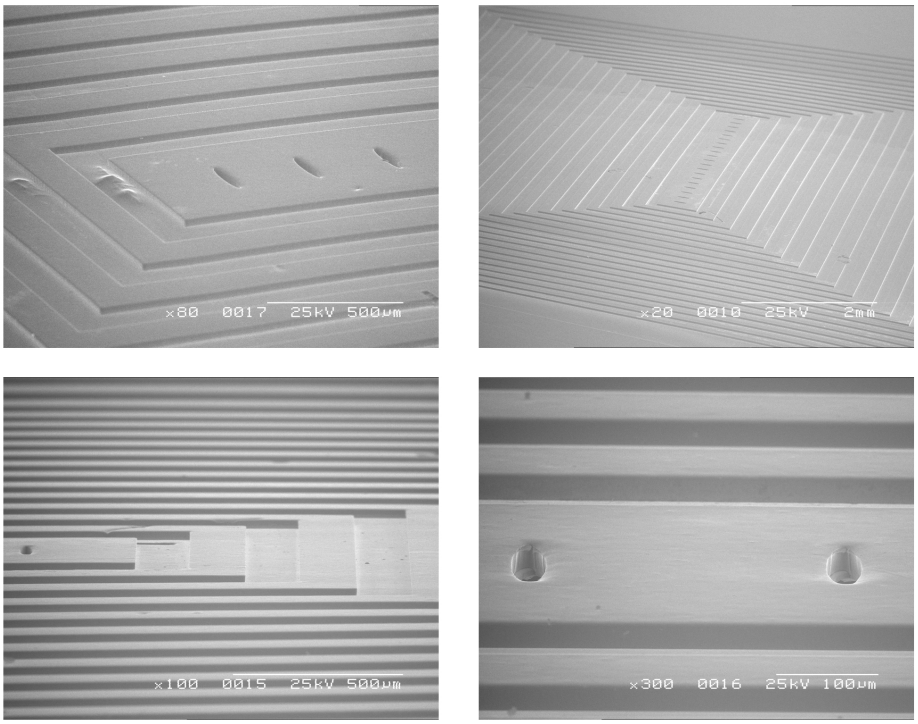


Figure 6.12: SEM images of the hybrid aperture array-corrugated device.

a total beam area to aperture area ratio of 1:0.00025, 35 times greater transmission was observed than that classically expected from direct transmission. The black and red traces show the 'super' extraordinary transmission displayed with the hybrid device - caused by a combination of the SPPs from the corrugations and the one dimensional periodic aperture array. Here, 400 times greater transmission was observed at 0.85 THz than that classically expected from the beam area to aperture area ratio. Thus, by simply surrounding the apertures with periodic corrugations, a 13-fold increase in transmission was induced. The transmission figures quoted above assume 100 % transmission through sub-wavelength apertures. Such transmission actually scales with $(r/\lambda)^4$, as described by Bethe [115], meaning the quoted transmission values are therefore underestimates. Interestingly, comparable transmission is achieved when the corrugations faced away from the THz source, demonstrating the importance of SPPs on the far side of devices. Such activity has been observed previously for the case of bulls-eye apertures [138], demonstrating that if periodic corrugations could be made on both sides of this hybrid device, even greater transmission

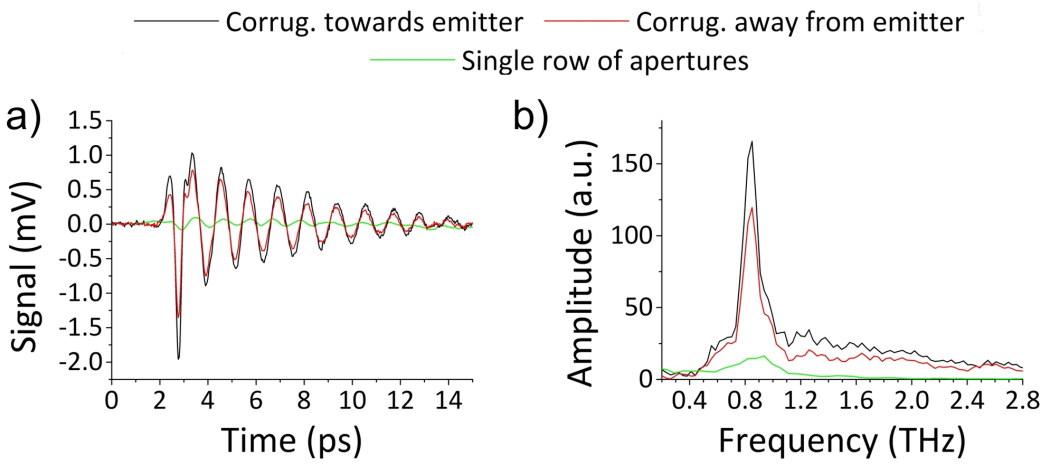


Figure 6.13: a) Time-domain results showing the magnitude of SPP activity, clearly demonstrating EOT. b) Corresponding FFT.

should be observed.

The exceptionally strong transmission is termed 'super' EOT. These vast transmission efficiencies can be attributed to the combined effects of SPP modes due to the commensurate periodicity of the apertures and corrugations. Two-dimensional aperture arrays are known to exhibit a redshifted frequency response from that predicted by the periodicity [39]. Further enhancements in transmission may be possible by matching the actual frequency response of both the apertures and the corrugations, as opposed to presuming an identical response from the periodicity alone.

This structure opens up the possibility of THz plasmonic sensing platforms. A powdered sample could be placed in the corrugations, modifying the SPP behaviour in this area. SPPs would continue towards the apertures and decouple as usual. The out of phase recombination of modified SPPs from the corrugations, and those initiated by the apertures, would lead to a resonance shift in the frequency domain. However, as no sample would have been placed in the apertures, overall transmission should not be affected, allowing strong signals to still be detected. It is unknown whether the combination of two different SPP modes is more sensitive than a simple modification of a single SPP mode. With the device presented above, the SPPs initiated by the single row of apertures may be

overwhelmed by the SPPs initiated by the corrugations. Thus, if a combination of SPPs turns out to be more sensitive, a more refined device featuring a two-dimensional array of apertures surrounded by periodic corrugations with commensurate periods, could prove to be an extremely sensitive device.

# Chapter 7

# Embedded Plasmonic Sensor

The intimate relationship between surface plasmons and the neighbouring dielectric has been exploited for gas, chemical and biological sensing in the IR region since the late 1970s [103, 112, 204]. These arrangements typically adopt Kretschmann or Otto optical configurations, where small changes in the surface plasmon resonance (SPR) angle can be related back to a change in the metal-dielectric interface. Commercial products have combined traditional SPR arrangements with microfluidic aspects [205], enabling greater control over sample delivery, whilst improvements in optical detection methods allow angular shifts of 0.0001 $^{\circ}$ to be reliably detected [112]. SPR experiments fundamentally measure a change in the refractive index of a dielectric due to binding interactions occurring close to the metal surface. Ultimately, the sensitivity of the technique relies on the spatial sampling of the surface plasmon in the dielectric layer. Greater sensitivity is achieved when the spatial extent of the change in refractive index matches the spatial extent of the SPP in the dielectric of interest. When refractive index changes occur very close to the metal surface, on a distance smaller than the spatial extent of the SPP, the sensitivity of the technique is reduced, as only a fraction of the SPP can probe the change in refractive index [204]. This fact becomes even more important when dealing with surface plasmon sensors in the THz regime, where SPPs are known to be loosely coupled to the surface, often extending over many wavelengths above the surface [206]

into the dielectric layer. As detailed in chapter 4, SPPs can be increasingly confined to the surface by entering the so called 'spoof' plasmon regime, where an effective refractive index can be engineered by decorating the metal surface with sub-wavelength structures. The devices presented in chapters 5 and 6 featured metal surfaces structured on the scale of $\approx \lambda/2$, too large to be considered truly spoof (although, as discussed, no strict definition as to when a material can be thought of as a 'spoof' surface currently exists). The sub-wavelength nature of the features will go some way to increase confinement to the surface however [106], opening up the possibility of plasmonic sensors at terahertz frequencies.

## 7.1 Previous THz Plasmonic Sensors

The effect of a dielectric layer on the transmission properties of a metal aperture array was first displayed in 2005 using a free standing array [136]. Here, the transmission peak was seen to redshift as the thickness of the dielectric (polypropylene) layer was increased, with the shift being attributed to a change in the resonant frequency of the SPP modes. Variations in thickness as small as 50 $\mu$m could easily be detected, even with the $\approx 1$ mm wavelength of the observed resonance. The authors correctly identified the fact that as the layer was only applied to one side of the array, coupling between SPPs either side of the array would be vastly reduced, hindering the sensitivity of the device. Similar free standing arrays have been demonstrated elsewhere, with the detection of 1 $\mu$m changes in polyethylene terephthalate films [197], whilst further applications have displayed the ability to detect the difference between blank and printed paper [199]. These devices are also found to work equally well in reflection geometry, as opposed to transmission [200]. Free standing arrays have also been used for the detection of different proteins, including horseradish peroxidase [41] and avidin [207]. Sharper resonances in the frequency domain ultimately allow smaller shifts to be recognised, incurred from small changes in dielectric

constant. Work by Yoshida et al. investigated the properties of a unique metallic mesh, whose resonance peak featured a sharp dip in the centre - an anomaly attributed to a diffraction effect [198]. This sharp feature could be exploited for use as a SPP sensor, however, no results are presented demonstrating this application. If the frequency of the dip is seen to shift non-linearly with the peak frequency as the neighbouring dielectric layer is modified, the validity of this technique is brought into question.

Metallic aperture arrays on silicon substrates allow dielectric layers to be easily applied using spin coating techniques, as demonstrated by Han et al. using photoresist layers [42]. Here, two resonances are observed due to SPP contributions from the metal-silicon, and metal-photoresist interfaces. The higher frequency metal-photoresist resonance is relatively broad, however, resonance shifts could be observed with thickness variations of $< 3$ $\mu$m when using thin layers. The limitations of this technique are demonstrated through the application of thicker layers, where no differences can be observed for the SPP resonances between thicknesses of 173 and 293 $\mu$m. Although not concluded by the authors, these figures may offer some information regarding the spatial extent of the SPP into the dielectric layer; refractive index changes occurring at a distance greater than the spatial extent of the SPP will have very little (if any) effect on the detected resonance.

Terahertz SPP sensors for gaseous samples have been theoretically described [208], though, to date, no practical devices have been realised. There exists only one example in the literature where an SPP sensor has been used to distinguish between liquid samples [201]. Here, a free-standing stainless steel aperture array was placed in a standard 1 mm thick quartz cuvette, and immersed in different isotopes of liquid methanol. Using standard THz-TDS measurement techniques, clear differences could be observed between the SPP resonances when different isotopes were present. Furthermore, these shifts were much more apparent than the differences in refractive index recorded using standard transmission THz-TDS. The often fragile nature of free-standing metal aperture arrays suggests they may be better suited for applications in liquid sensing as opposed to the analysis of solid

films. This single demonstration proves the viability of the technology, displaying distinct advantages over current techniques.

## 7.2 THz-SPP Microfluidic Sensor

A greater understanding of SPP behaviour in two-dimensional aperture arrays was gained from the work undertaken in chapter 6. This knowledge ultimately allowed sharp resonances to be engineered in the frequency domain (figure 6.3) - a desirable feature for sensor applications. As a proof of principle experiment, a standard copper aperture array (160 $\mu$m x 40 $\mu$m apertures, 300 $\mu$m period) was placed in a 1 cm diameter PTFE sample cell. A THz-TDS reference scan produced the black traces observed in figure 7.1. When IPA was added to the sample cell, a slightly delayed, longer oscillatory temporal trace was observed, producing a red-shift of the resonant frequency (red traces in fig. 7.1). Emptying the cell of liquid such that only a small amount of IPA remained on the surface of the array produced the green curve in figure 7.1b. Interestingly, this peak frequency is identical to that observed for when the array was fully immersed, displaying the surface sensitive nature of the technique. Fully drying the array shifted the resonance back to its original position (blue trace in fig. 7.1b).

Even with this relatively crude arrangement, the sensitivity and robustness of the technique could be easily demonstrated. The large path length associated with the PTFE sample cell meant that only a low absorbing sample such as IPA could be used. Ideally, a more controlled arrangement featuring a much reduced path length would allow for optically dense samples, such as water, to be analysed. Ultimately, a device featuring a combination of the microfluidic work presented in chapter 3, with the SPP sensor capabilities displayed above, would create an immensely sensitive, versatile device. Not only could such a device be used to distinguish between samples, but it could be used to detect real-time binding events on a functionalised surface, interrogated on a pico-second

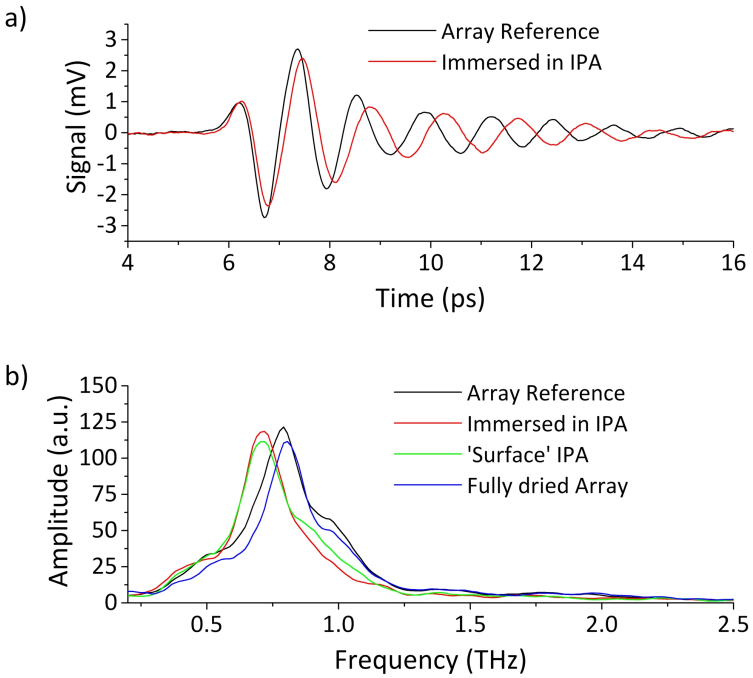


Figure 7.1: a) Temporal waveforms for the array reference and the array when immersed in IPA b) Frequency domain results displaying the shift in resonance as the IPA is introduced. When only a small amount of IPA is on the surface, the resonant frequency is the same as the fully immersed array, displaying the surface sensitive nature of the technique. Finally, by fully drying the array, the resonance can be switched back to that of the original reference.

timescale.

A simple method to integrate a plasmonic sensor into the microfluidic environment demonstrated in chapter 3 would be to lithographically define an aperture array on the blank silicon wafer used to seal the chamber. This solution would suffer from poor sensitivity due to the reduced coupling of SPPs either side of the array from the two different metal-dielectric interfaces. A free-standing suspended array is therefore much more desirable. The design and fabrication of a free-standing metallic array contained within a microfluidic arrangement is however, far from trivial. Suspended membranes are common in MEMS devices, and feature in a variety of applications [84]. Any technique adopted here would have to leave a region of silicon on which to bond a further chamber over the top of a suspended membrane. An initial design was devised, which utilised a silicon-on-insulator (SOI) wafer, as detailed in the following section.

### 7.2.1 SOI Device Design

An initial design for an embedded device involved the use of an SOI wafer, as depicted in figure 7.2. The design of the device hinged upon the use of a 15 $\mu$m thick, $p^+$ boron doped silicon layer. Boron is commonly implanted into silicon to act as an etch stop for KOH etches [209]. To begin, the aperture array is created in the device layer using an RIE vertical etching of silicon (fig. 7.2b). The buried oxide is subsequently undercut using a buffered HF etch (fig. 7.2c), after which a KOH etch is used to create a chamber underneath the doped layer, effectively suspending the membrane (fig. 7.2d). By bonding a further chamber over the top of the device, a suspended array in a microfluidic environment could be realised (fig. 7.2e).

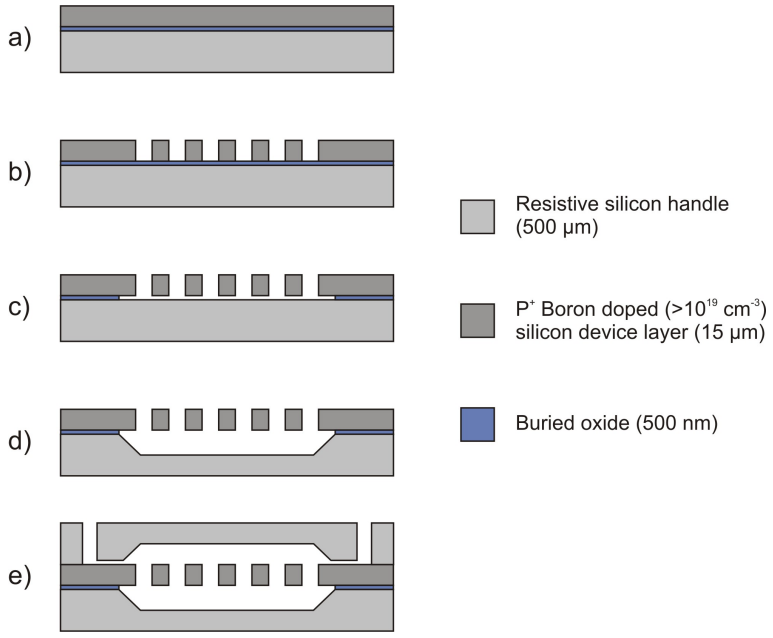


Figure 7.2: Initial fabrication process for the embedded device using an SOI wafer

In this design, the $p^+$ device layer would not only act as an etch stop (such that it would not etch when etching the chamber in KOH), but the high doping density ($1\times10^{20}$ - $3\times10^{19}$ $cm^{-3}$, 0.001 - 0.003 $\Omega$cm) would result in metallic like behaviour at terahertz frequencies, allowing SPP modes to be established [40]. A further advantage of this design is that boron doped silicon exhibits tensile stress [210], such that the released membrane

would pull itself tight, reducing the risk of membrane stiction.

To begin the fabrication, a gas chemistry had to be found which resulted in vertical etching of silicon in a standard RIE, to enable the creation of the aperture array. Typically, deep reactive ion etching (DRIE) by either cryogenic [211] or Bosch [212] techniques are employed for this process. Using fluorine based plasmas, and carefully controlled gas chemistries, deep vertical etching of silicon can be achieved using a standard RIE (often called the 'black-silicon' method) [213–217]. With factors such as pressure, power, temperature, feature size, mask material, length of etch, exposed area, platter type, position on stage, doping level and chamber contamination all playing a role, a range of controlled experiments was undertaken to find desirable parameters. Prior to each etch, a chamber clean was undertaken with the following parameters: 100 sccm $O_2$, 5 sccm $CF_4$, 600 mTorr, 400 W, PE mode, 10 minutes. Parameters for the $O_2$ and $SF_6$ flow rates, pressure and power were initially chosen with guidance from the work of Jensen et al. [218]. Initial conditions of 200 mTorr, 160 W, 11.5 sccm $O_2$, 12 sccm $SF_6$, 20 °C, graphite platter for 15 minutes, produced the etch profile in figure 7.3a. Although a substantial etch depth was achieved, significant undercutting of the mask was observed, along with a very rough surface profile. Through a combination of increasing $O_2$ flow rate, decreasing the power and reducing the temperature, deep, almost vertical trenches with smooth side walls and little undercut was eventually achieved (fig. 7.3d).

After developing the deep etching method, the remainder of the fabrication process could be trialled. It was soon discovered the process suffered from many unforeseen problems. The HF etch of the buried oxide took 24 hours to complete due to the relatively large distances between the apertures. In this time, bubble formation on the surface of the silicon device layer caused a 'pitting' of the surface, a factor which would become a major issue in the final bonding step. When undertaking the KOH etch of the chamber, a more evident problem arose from the fact that the device layer was found to etch at a substantial rate, as displayed in figure 7.4, where an etch ratio of 1:3 was observed for the

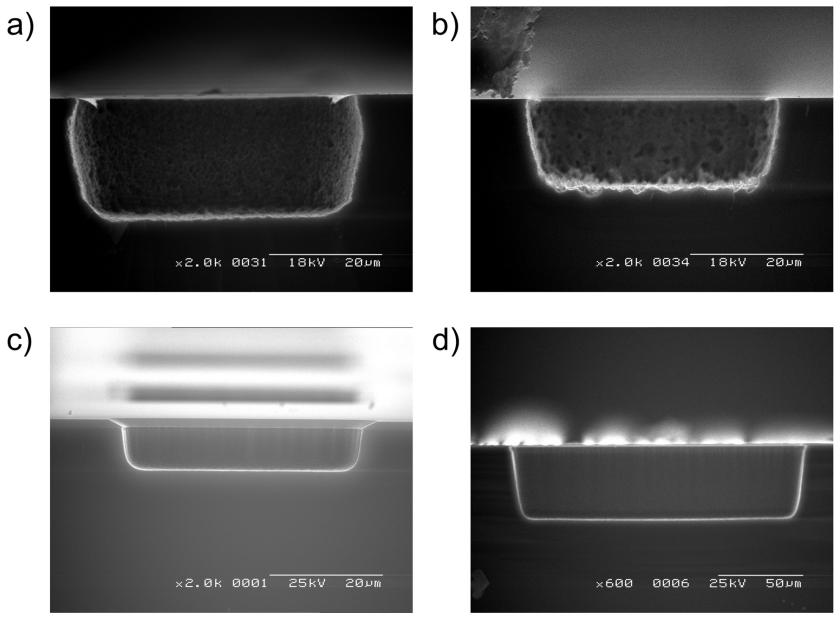


Figure 7.3: Selected SEM images of results from RIE etching of silicon with the following conditions a) 200 mTorr, 160 W, 11.5 sccm $O_2$, 12 sccm $SF_6$, 20 °C, 15 mins. Figures b) to d) varied from a) using: b) 11.5 sccm $O_2$, c) 14.75 sccm $O_2$, 100 W and d) 13 sccm $O_2$, 87 W, 5°C table temperature.

doped, to undoped wafer. It was initially thought that the choice of an oxide mask may have have been to blame, with the boron dopant being driven into the oxide layer during the oxidation process, as detailed in [219]. The same effect however was observed when an un-oxidised wafer was placed in the KOH, with similar etch rates being observed. It was later discovered that for boron doping to act as a substantial etch stop (etch ratios in excess of 1:10), the doping density needs to be greater than $1\times10^{20}$ $cm^{-3}$ [220]. The tolerance on a wafer used here was quoted as 0.001 - 0.003 Ωcm, corresponding to a doping density of $1\times10^{20}$-$3\times10^{19}$ $cm^{-3}$, lower than that required for an effective etch stop. For this reason, a gold electroplated mask was used to protect the device layer. This mask introduced further problems from the fact that the silicon was attacked during the HF etch - thought to be due to a galvanic reaction [221].

A much simpler approach was then adopted. As the etch ratio of the device layer was found to be substantial, a KOH etch was used to create the aperture array using an oxide mask. Buffered HF was used to release the membrane, after which the device was spin

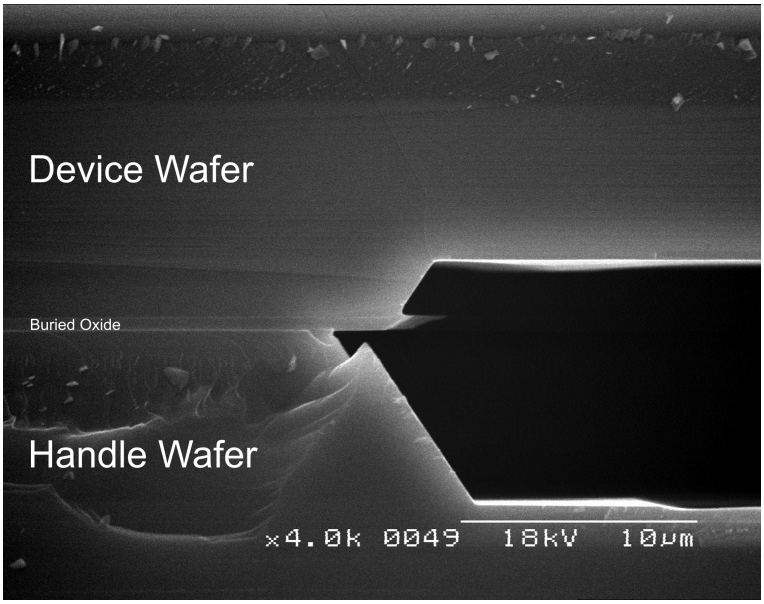


Figure 7.4: SEM image displaying a 1:3 etch ratio for the doped device layer to the handle wafer.

coated with photoresist, and exposed through a light field mask, such that resist remained at the bottom of the apertures. After evaporating a 100 nm layer of gold, a lift-off process removed any gold which had been deposited on top of the resist. This lift-off process was then repeated for a gold electro-plating step, designed to protect the front of the device layer during the KOH etch for the chamber (fig. 7.5a).

A large proportion of the etched chamber featured highly non-uniform etch characteristics, as displayed in figure 7.5c. Large area suspended membranes 8 $\mu$m thick could be created (fig. 7.5d), with the membrane visibly pulling itself tight when any liquid placed on the array was dried off. If the device layer was etched too thin, the membrane would eventually fracture, setting a limit to the membrane dimensions which could be achieved. Surface roughness was a major issue, and ultimately the stalling point of this design. The gold plated layer suffered pinhole defects, occurring from the 'pitting' of the silicon surface during the HF release. With no other route to undercutting the array through etching the oxide, an alternative design was adopted.

One final question was also raised over the THz-TDS results obtained when a suspended array was placed in the beam. No evidence of SPP activity was observed for

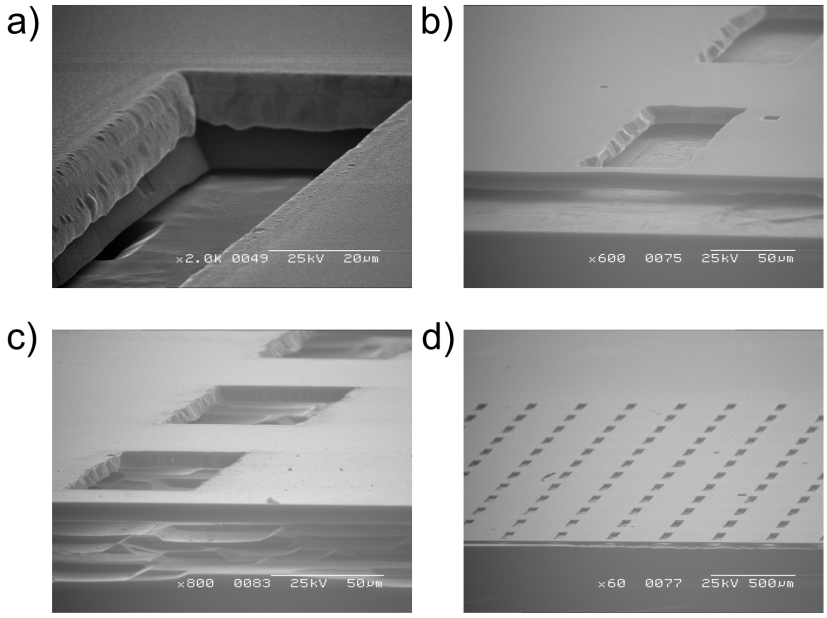


Figure 7.5: SEM images displaying a) Plated gold mask protecting the front of the device layer during the KOH etch of the chamber. b) Aperture with uniform etch of chamber underneath. c) Non-uniform etch of chamber underneath aperture. d) Large area view of the suspended membrane.

the semiconductor array, unlike previous results in the literature featuring similar doping densities and aperture dimensions [40, 135]. The only major difference was the choice of semiconductor; the array displayed above used p-type silicon, whilst all aperture array results in the literature use n-type. P-type materials have been used to demonstrate THz SPPs for the case of a sub-wavelength slit flanked by periodic corrugations [222]. However, with no evidence in the literature, this raises the interesting question as to whether p-type silicon aperture arrays can be used to observe SPPs in the terahertz region.

### 7.2.2 Revised Device Design

Following the failings of the initial SOI design, a different approach was adopted using a sacrificial device layer on an SOI wafer. To begin the process, a standard SOI wafer featuring a 500 $\mu$m thick resistive silicon handle, a 40 $\mu$m thick resistive silicon device layer and a 500 nm buried oxide, was oxidised to provide a 500 nm mask layer. A 1 cm$^2$ square region was etched in the oxide layer in the centre of the wafer using an RIE

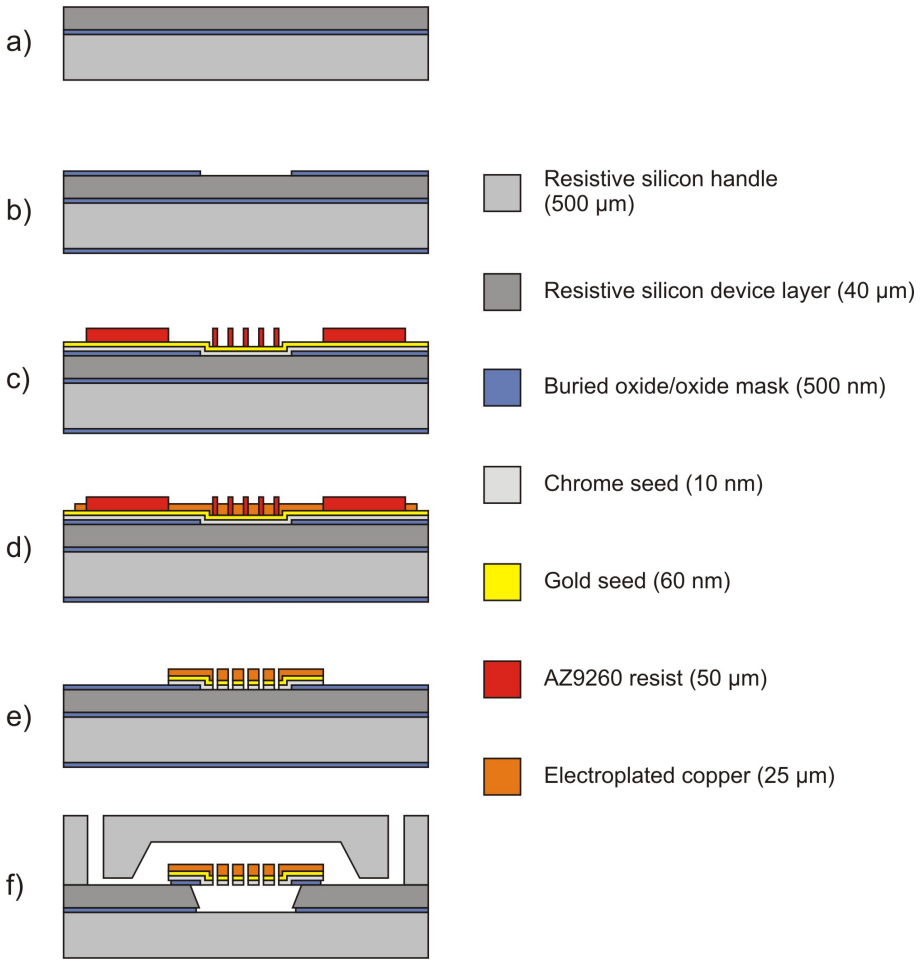


Figure 7.6: Fabrication process for the embedded device using a sacrificial device layer on an SOI wafer, allowing a suspended metallic array to be created.

etch (fig. 7.6b). A 10 nm seed layer of chromium and a 60 nm layer of gold were then evaporated onto the wafer, after which the three layer resist process detailed in section 6.2 was carried out. A 20 $\mu$m thick copper foil was then electroformed around the resist, producing a metallic aperture array of 4 mm$^2$ (fig. 7.6c). After removing the resist in acetone, and etching the gold ($I_2$:KI:$H_2O$, 1:4:40) and chromium (HCl) seed layers (fig. 7.6e), the exposed silicon region underneath the array was etched using an isotropic $XeF_2$ etch. The buried oxide acted as an etch stop in the vertical direction, allowing a chamber with a flat bottom to be produced. The etch was carried out until the horizontal undercut ensured no vertical pillars remained masked underneath the array (fig. 7.7). The device was then placed in KOH to remove any remaining silicon, producing a fully suspended

metallic aperture array (fig. 7.8a), above which a further chamber could be bonded to encapsulate the sensor (fig. 7.6f).

By electroforming a relatively thick copper array, little to no deflection could be observed from capillary forces acting on the suspended membrane when immersed in IPA. Once bonded, the fully encapsulated nature of the device would ensure any such forces would act equally either side of the array, ruling out membrane stiction as a potential problem. This was confirmed by taking a cross-section of the device (fig. 7.7b). Bonding of the device was completed using a hand alignment step, with a successful bond being verified using an infrared camera (fig. 7.8b).

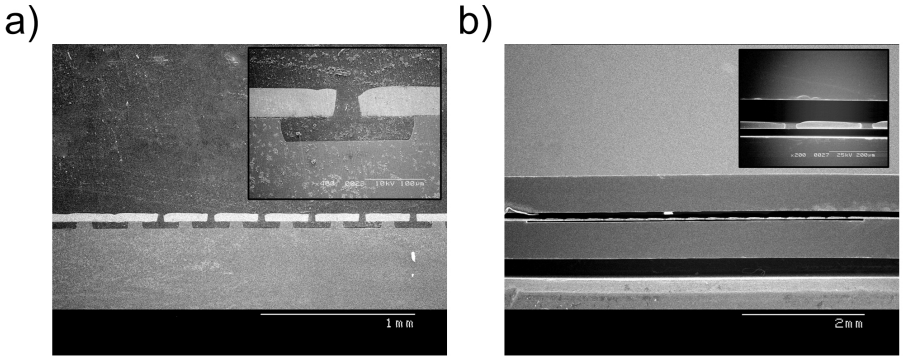


Figure 7.7: a) SEM image of device cross-section displaying a copper array not fully released by $XeF_2$ etch. b) SEM image of device cross-section showing the fully released, embedded copper array, where no signs of membrane stiction can be observed.

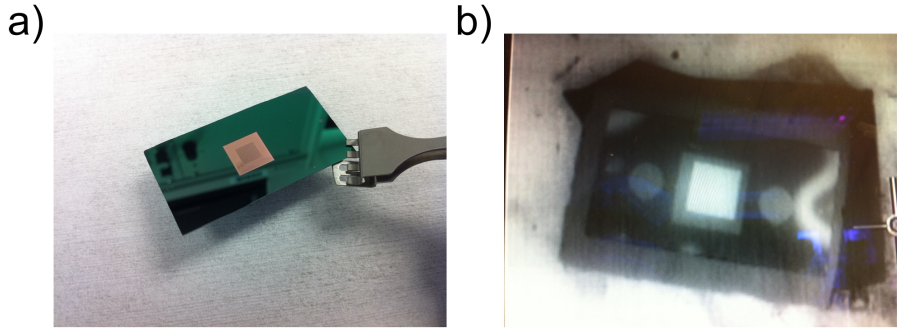


Figure 7.8: a) Photograph of a fully suspended copper aperture array on an SOI wafer. b) Photograph of the IR camera image used for inspecting the wafer bond. The embedded copper array is clearly visible in the centre of the larger area top chamber.

## 7.3 Results

The success of this device hinged on two key aspects - absolute transmission and a strong plasmonic resonance. The results presented in section 3.3 demonstrated the reduction in transmission associated with using a silicon based device. Here, an extra reduction in transmission could be expected from the presence of the sub-wavelength aperture array. Furthermore, the temporal properties of multiple interface reflections, both from non-resonant direct transmission and resonant SPP transmission, were another potential problem. It was unknown whether a coherent temporal oscillation from SPP transmission could be observed, given the potential for destructive temporal interference.

### 7.3.1 Empty Chamber Reference

The device was positioned with the copper aperture array at the focus of the THz-TDS system. A long temporal scan (80 ps) was taken, revealing the temporal properties of the device (fig. 7.9a). Overall transmission of $\approx 4$ % was achieved compared to a free space reference, allowing a strong signal to be detected, well above the background noise of the system. Temporal activity could be observed as far out as 65 ps in time, as a result of strong Fresnel reflections at each air-silicon boundary. SPP transmission, characterised by distinct, periodic temporal oscillations could be easily recognised (regions 2, 3 and 4 in fig. 7.9a), each preceded by non-resonant, direct transmission. A Fourier transform of the complete temporal trace (fig. 7.9b) produced a distinct peak in the frequency domain at 0.8 THz, related to the enhanced transmission through the array. A range of other peaks were also clearly evident, arising from artefacts in the FFT due to the non-periodic nature of the multiple pulses. By windowing the FFT, selecting just the first 12 ps of the scan, conventional transmission properties of the aperture array could be easily identified, with a pronounced peak at 0.8 THz, followed by broadband transmission at higher frequencies from direct transmission through the aperture array (fig. 7.9c). Although windowing the

temporal traces allows for adequate FFTs to be obtained, a more thorough approach may look to utilise wavelet transforms [223, 224] or spectrochronography [225].

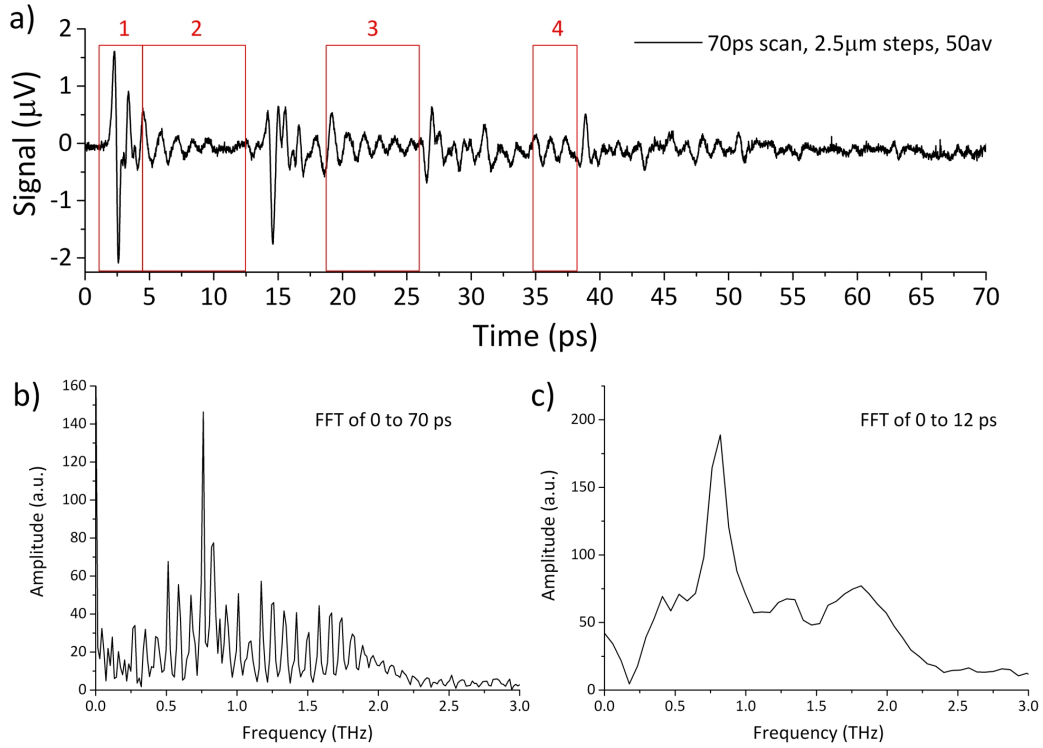


Figure 7.9: a) Time domain reference scan of empty device. Distinct SPP resonances can be observed in the highlighted areas 2, 3, and 4. b) FFT of complete time domain trace with evident FFT artifacts. c) FFT of region 0 - 12 ps displaying conventional transmission properties of a free standing array.

The position of the transmission peak (0.8 THz) matches that achieved using a free standing array with the same aperture dimensions, as shown in figure 6.3. This identical frequency response demonstrates two important facts about the embedded array. Firstly, it can be concluded the array does not suffer from stiction issues and is not in contact with the silicon chamber. Any contact, however intimate, would result in a redshift of the expected resonance. Secondly, it can be assumed that the spatial extent of the surface plasmons is less than 50 $\mu$m, the depth of the chamber either side of the array. If the surface plasmons were to extend into the silicon substrate, a different frequency response would be expected, resulting from the plasmons sensing an air-silicon dielectric medium.

The introduction of fluid into the chamber would undoubtedly drastically alter both the

temporal response of the SPP transmission and the multiple boundary reflections, making the temporal waveform beyond 15 ps extremely complicated, changing unpredictably each time a different fluid was introduced. From an experimental perspective, it was decided that for the proof of concept experiments, only the first 12 ps of temporal information would be recorded. This region displays the highest intensity SPP resonance, with the greatest temporal window before a successive reflection appears.

### 7.3.2 IPA-$H_2O$ Series

To test the sensitivity of the device in a fluidic environment, an IPA-$H_2O$ series was analysed. A 2 $\mu$m step size (0.013 ps) and 100 averages allowed detailed time-domain traces to be recorded. After taking a chamber reference, samples were pumped through the device in turn, each sample differing by 20 % IPA concentration. The time-domain results are displayed in figure 7.10.

The empty chamber reference clearly shows a single cycle main pulse arising from broadband non-resonant transmission, followed by a decaying temporal oscillation resulting from successive SPP transmission. When IPA is introduced into the chamber, three characteristic changes can be observed: the main pulse is delayed with respect to the reference due to the higher refractive index of IPA over air, a reduction in signal is observed due to dielectric losses in the liquid, and the temporal oscillations following the main pulse occur on a much longer timescale. As the water content is increased, these effects become much more pronounced, with a distinct broadening and reduction in intensity of both the primary pulse and SPP oscillations. The 100 $\mu$m chamber depth used for this device is close to the maximum limit if water is to be analysed, due to the low intensity signals which were detected. Furthermore, the 100 $\mu$m path length means, unlike the device presented in chapter 3, the benefits of improved refractive index matching when using IPA do not outweigh the absorptions from transmission through the sample, hence a decrease in signal intensity is observed.

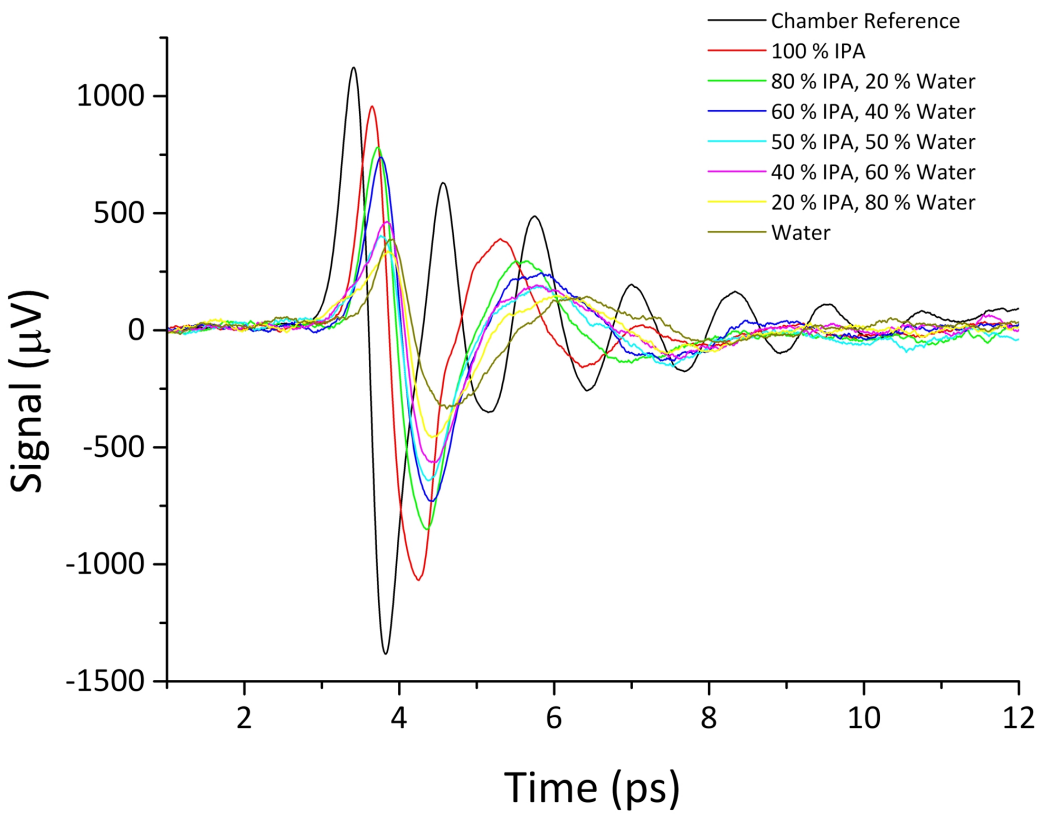


Figure 7.10: Temporal waveform showing the evolution of the plasmonic activity as water concentration is increased.

By taking Fourier transforms of the data, the device sensitivity is clearly displayed, with a distinct redshift of the observed SPP resonance as water concentration is increased (fig. 7.11).

Such a frequency shift can be clearly understood by analysing equation 4.18, $\lambda_{peak} = L/\sqrt{(i^2+j^2)}\sqrt{\epsilon_d}$. Here $L$ is the period of the array, $i$ and $j$ are the mode orders (1 and 0 respectively in the case of the fundamental mode exploited here) and $\epsilon_d$ is the dielectric constant of the fluid. By plotting the observed peak frequency as a function of IPA concentration, fits can be made to the data, calculating the expected peak position from the dielectric properties (refractive index) of the liquid (fig. 7.12). The dielectric information was extracted separately using results from chapter 3, along with previously published literature [16, 226].

The observed peak frequencies can be seen to redshift 0.24 THz over the IPA-$H_2O$

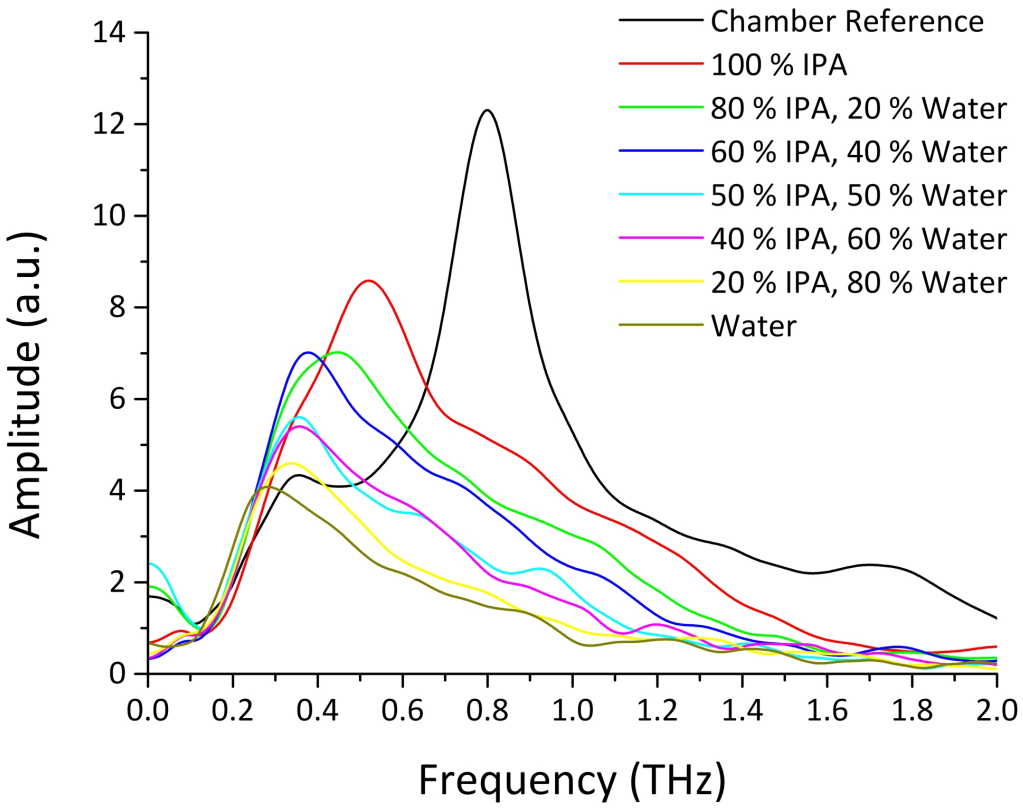


Figure 7.11: Fourier transforms of the time domain data displayed in fig. 7.10. One can clearly see the redshift in the peak frequency as the water content is increased.

series, from 0.52 to 0.28 THz as the refractive index of the fluid is increased. Fitting theoretical traces to this data requires a number of decisions to be made relating to which specific frequency the dielectric information is taken at. Although the periodicity of the device is 300 $\mu$m, corresponding to an expected resonance at 1 THz, the observed resonance is 0.8 THz. As it is the strict *periodicity* of the array which defines the excitation frequency of the SPPs, dielectric properties will be calculated at the frequency corresponding to the array periodicity, i.e. 1 THz. Calculating the predicted peak position from the 1 THz dielectric data produces the red curve in figure 7.12, which follows the overall shape, but resides above the recorded data. By shifting this curve down by 0.2 THz, the difference between the theoretical and observed peak positions of the array, the green curve is produced, providing a reasonable fit to the data. Justification for this shift can be given as follows: Although the frequency response of the array produces a peak at 0.8

THz, the periodicity of the apertures excites SPPs at 1 THz. This excitation frequency dictates the frequency at which the dielectric information should be calculated. As the array resonance is observed at 0.8 THz, not 1 THz, the calculated peak positions cannot be expected to fit unless shifted by the difference between the theoretical and observed resonances.

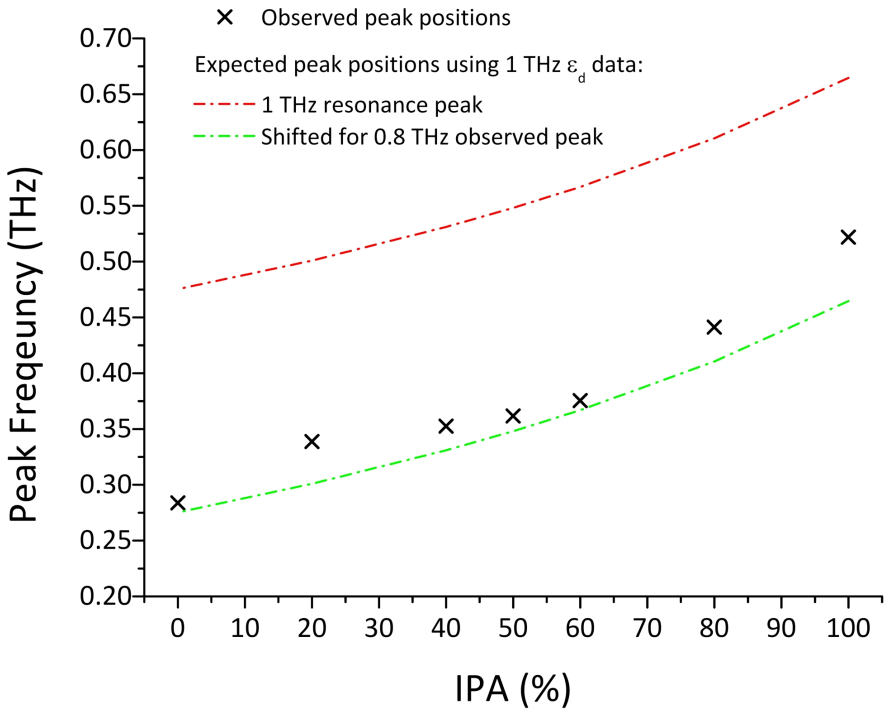


Figure 7.12: Plot of observed peak position as a function of IPA concentration. The two dotted traces corresponds to the expected position of the peaks calculated using the dielectric data of the SPPs at 1 THz (the SPP excitation frequency). The red trace shows the positions for a 1 THz array resonance, whilst the green trace shows the expected peak positions shifted for the 0.8 THz array resonance peak actually observed.

The green trace produced in figure 7.12 clearly follows the shape of the data. An ideal fit to the data cannot be expected due to the discrepancies between the theoretical and observed resonances of the bare array, ultimately dictating the degree by which the data should be shifted. Theoretical discrepancies lie in the approximations made to arrive at equation 4.18, namely the lack of consideration given to aperture dimensions, array thickness, the dielectric properties of the metal and diffraction effects. Physical

discrepancies, argued from a time-of-flight perspective, arise due to the various distances between apertures, the finite velocity of the plasmons, and the unknown processes by which SPPs couple and recouple. Ultimately, despite knowledge of the aforementioned unknowns, the device has clearly demonstrated the ability to sense changes in a neighbouring dielectric through modifying the SPP resonance. As highlighted with analysis of similar devices [201], an improved quantitative model must be devised before the device can be used to identify materials based on the observed redshift of the SPP resonance.

As a measure of the sensitivity of the device, a metric calculating the observed resonance shift ($\Delta f_{obs}$) divided by the change in refractive index of the fluids causing the shift ($\Delta n$), was adopted, as per reference [201]:

$$Sensitivity = \Delta f_{obs}/\Delta n \tag{7.1}$$

Calculating these values from the array reference resonance frequency produced the results presented in figure 7.13. The calculated sensitivity demonstrates the device to be most sensitive when dealing with fluids with small refractive indices, with sensitivity residing around 0.54 THz/RIU. As the refractive index of the solution increases, the sensitivity can be seen to decrease - demonstrated by the smaller differences between the observed peak frequencies as IPA the content was decreased (fig. 7.12). A greater sensitivity is achieved with our embedded device when compared to the only other similar device in the literature [201], where a sensitivity of 0.40 THz/RIU was demonstrated.

Ultimately, the plasmonic device offers many distinct benefits over the simple device presented in chapter 3. The results of the plasmonic device are decoupled from the thickness of the chamber, with the frequency response of the device relying only on the intimate relationship between the surface plasmons and the neighbouring dielectric. Furthermore, as the device analyses frequency shifts, it is no longer susceptible to laser fluctuations (intensity drop-off), a factor which often hampers traditional THz-TDS experiments.

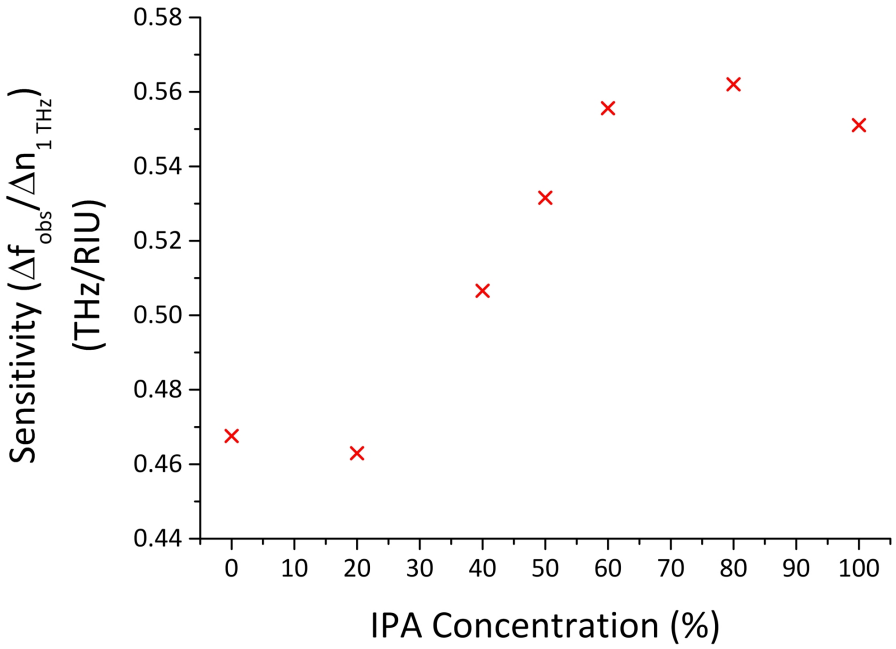


Figure 7.13: Sensitivity of the device calculated using equation 7.1, as used in [201].

# Chapter 8

# Conclusions

The unique benefits of THz-TDS have seen it rapidly become a commonplace tool in academic research and industry. Besides the inherently useful broadband nature of the technique, the access to temporal information can itself be exploited to give a greater understanding of underlying physical mechanisms. There are however, many fundamental problems associated with the technique, the most prominent of which is the strong absorptions which occur when analysing aqueous samples. Whilst higher power sources can be used to circumvent this problem (e.g. THz QCLs), the temporal and broadband aspects of the TDS systems are lost. As the wavelength scales associated with THz radiation are commensurate with the dimensions commonly used with bulk microfabrication techniques, devices can be fabricated which are structured on the same length scale as the radiation. This thesis has sought to exploit existing microfabrication techniques to create devices which provide a direct solution to the problems associated with THz-TDS. This confluence of technologies has enabled a variety of microfluidic and plasmonic devices to be fabricated and tested, culminating in a plasmonic sensor with a range of potential applications.

Working between the electrical and optical regimes of the EM spectrum, in itself, provides many challenges, mostly involving the generation of coherent sources of radiation. Chapter 2 explored the current technology used to both generate and detect coherent

sources of THz radiation, concentrating on the THz-TDS arrangement utilised in this thesis. Working in the time-domain provides a further set of challenges, specifically when accurate spectroscopic information is required. Basic data extraction techniques were outlined, demonstrating how dielectric information can be extracted from temporal waveforms, without the need for Kramers-Kronig relationships. A more thorough derivation was given for data extraction techniques involving sub-wavelength, dielectric filled cavities, where Fabry-Pérot effects must be taken into consideration. Finally, a data extraction algorithm was detailed, demonstrating how more accurate data can be yielded through defining and minimising an error function.

Chapter 3 documented the design, fabrication and testing of a microfluidic device for THz frequencies, fabricated from silicon - a material inherently transparent to THz radiation. Ultimately, this device hinged on the idea that by minimising the optical path length through a fluidic sample, a strong signal could be detected after direct transmission. Exploiting a range of lithographic, chemical etching and wafer bonding processes, a microfluidic sample cell was fabricated solely out of silicon. These processes, in conjunction with a variety of surface profiling techniques, enabled cavities to be etched and measured to sub-micron tolerances - an important factor for extracting accurate dielectric data. The design enabled samples to be pumped through the device, in turn, negating alignment discrepancies when interchanging samples. A 50 $\mu$m chamber depth proved ideal, with refractive index matching increasing transmission when using low loss dielectrics, whilst allowing strong signals to be detected when using liquid water. Accurate dielectric properties of a range of samples were extracted using the algorithms and considerations outlined in chapter 2. Ultimately, this device provides the necessary means to analyse aqueous solutions in a standard THz-TDS arrangement, enabling a myriad of biological studies to be undertaken.

A detailed background to surface plasmon polaritons was presented in chapter 4, providing formal definitions, details of their dispersion relations and the implications for their

excitation at optical frequencies. The phenomenon of extraordinary optical transmission was then introduced, detailing the historical experimental discovery of this interesting anomaly. The remaining section of the chapter concentrated on surface modes at THz frequencies, outlining the nuances and boundaries between different surface modes, along with the idea of 'spoof' SPPs, generated by surfaces structured on a sub-wavelength scale. This review was evidently necessary, given the confusion and lack of clarity in the literature. The chapter was concluded by presenting the underlying physics surrounding EOT observed using two-dimensional arrays of sub-wavelength apertures, prior to a comprehensive literature review of the work previously undertaken on the topic.

Chapter 5 looked to build upon the physics and theories presented in the chapter 4, by exploiting SPPs to increase transmission through a sub-wavelength aperture for THz near-field imaging. Plasmonic apertures ultimately allow greater transmission through ever-decreasing apertures diameters, increasing spatial resolution for near-field imaging applications. Plasmonic 'bulls-eye' apertures were created using the negative photoresist SU-8, flanking a single, sub-wavelength aperture with periodic corrugations. By matching the period of the corrugations to the wavelength of the THz QCL source, EOT was clearly observed, demonstrated by line scans of the intensity profile of radiation exiting the aperture. However, the presence of high intensity side lobes, thought to originate from the decoupling of SPPs on the exit facet of the aperture, acted as further point sources, ultimately limiting the achievable spatial resolution for imaging applications. By planarising the existing apertures with a further layer of SU-8, even greater transmission was achieved, with no sacrifice to beam quality. As a proof of concept imaging experiment, inhomogeneous mixtures of an amorphous polymer pharmaceutical tablet coating, and crystalline drug samples, were raster scanned in the near-field of the aperture. The intensity variations detected in the far-field related to the absorption differences between the amorphous and crystalline domains - not detectable using optical microscopy. The use of sub-wavelength apertures allowed these compositional variations to be imaged with a

greater spatial resolution than that classically achievable with the wavelength of the QCL source.

The work documented in chapter 6, investigated the effects of aperture dimensions on the transmission properties of two-dimensional sub-wavelength aperture arrays at THz frequencies. This thorough experimental work led to the development of a time-of-flight theory, explaining the transmission properties of these structures. The qualitative model can be used to explain the combined effects of varying aperture width, length, orientation, area and aspect ratio, such that extremely sharp resonances can be engineered in the frequency domain. Much of this work is owed to the exceptional transmission properties of free standing electroformed copper arrays, where distinct temporal oscillations were observed with relative ease. This fabrication process ultimately allowed the creation of hybrid structures, combining the aperture arrays with the surface plasmon techniques of chapter 5, to demonstrate 'super' EOT.

The culmination of this thesis, in chapter 7, combined the microfluidic technology developed in chapter 3, with the highly resonant surface plasmon structures presented in chapter 6. This device exploited the innate dependence of the surface plasmons to the metal-dielectric interface, for use as a sensor. A free-standing copper aperture array was embedded inside a microfluidic cell. Clear, coherent temporal oscillations could be detected when the device was placed in a standard THz-TDS system, leading to a pronounced peak in the frequency domain. By introducing the a range of fluids into the device, the change in the metal-dielectric interface induced a change in the amplitude and period of the temporal oscillations, redshifting the resonant peak in the frequency domain in relation to the refractive index of the fluid. This plasmonic sensor demonstrates how microfabrication can be successfully exploited to create devices for THz applications, encompassing a range of technologies - from fluidics to plasmons, all on a sub-wavelength scale.

## 8.1 Future Work

The work presented in this thesis has opened up a variety of exciting research avenues. Future work could not only seek to utilise the microfluidic devices for spectroscopic studies, but also begin to probe the fundamental properties of surface plasmons at terahertz frequencies, through further experiments with the copper aperture arrays. The microfluidic devices presented in chapters 3 and 7 differ greatly in their operation, however the short optical path lengths allow a range of spectroscopic investigations to be undertaken. The simple microfluidic cell provides a means to assist studies of dynamics and hydration in biological systems, [8–11], as strong terahertz signals can be detected after interaction with aqueous solutions. The inclusion of mixing chambers in the device would allow for greater fluidic control, which, when used in conjunction with a fast optical delay line, would allow kinetic induced terahertz absorption (KITA) style experiments to be undertaken [227]. Further work into the underlying structure and dynamics of liquid water [12, 19, 24] will also be possible with this device. The creation of a 'nanofluidic' device, by defining a chamber in a $SiO_2$ layer, as opposed to silicon, would allow for experimental testing of the dynamical models currently proposed for polar mixtures under nanoconfinement [228].

Whilst silicon is transparent to terahertz radiation, the strong Fresnel reflections occurring at each silicon-air interface reduce the achievable transmission through the microfluidic device. The inclusion of broadband anti-reflective structures on the outer silicon surfaces [82, 229] would allow even stronger signals to be detected than those demonstrated in this thesis. An even simpler approach could even take the form of a refractive index matching material, where the application of Scotch tape may provide distinct benefits [230]. Silicon is often used as a platform for the attachment of monolayers of organic materials [231–234]. By exploiting these techniques, enzyme catalysis monitoring experiments, similar to the work presented in [235] could be undertaken, where standard THz-TDS arrangements could be used instead of the lower frequency vector network

analysers demonstrated previously. These experiments fundamentally rely on the ability to monitor monolayer binding events on a functionalised surface. Whilst it is unknown whether traditional transmission THz-TDS spectroscopy would be able to distinguish between the dominant aqueous environment, and a change in refractive index caused by a surface binding event, such experiments would have a greater chance of success using the plasmonic device presented in chapter 7. Here, experiments would resemble traditional infrared SPR experiments, where mono-molecular binding events could be monitored in real-time by observing a shift in the plasmonic resonance in the frequency domain.

The study of SPP modes excited on copper aperture arrays presented in chapter 6, revealed a great deal of information about the temporal properties of these surface states. Further work needs to be undertaken to understand the microscopic processes involved with decoupling events [236], and how these modes vary as a function of array thickness and incidence angle. More fundamentally however, there is a great deal of work which can be done to probe SPP lifetime, velocity and confinement.

The velocity and confinement of SPPs could be investigated using an arrangement displayed in figure 8.1. This arrangement is similar to that used in reference [206], however, periodic corrugations fabricated using the double plating technique (section 6.6), would be used for the SPP coupling and decoupling mechanism as opposed to the inefficient knife-edge launch mechanisms used previously (where coupling efficiency is $\approx$1 % in the infra-red region [36, 237]).

By decorating the central region, using complimentary sub-wavelength, periodic pits or dimples for example (as in fig. 8.2), the confinement, and ultimately the velocity of the SPPs will be varied. A quantitative measure of the velocity of the SPPs could be taken from the temporal waveforms, whilst the perpendicular confinement could be measured using a metallic knife-edge to act as a cut-off, blocking any propagating modes extending above a certain distance from the metal surface. The extent of the spatial confinement could then be measured as a function of the dimensions of the surface modifications. A

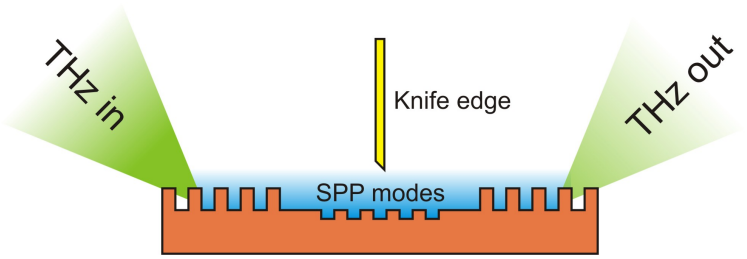


Figure 8.1: Possible optical arrangement to investigate the velocity and confinement of surface plasmons. Periodic corrugations initiate the SPPs which travel across the central region. By decorating this region with sub-wavelength periodic pits, or dimples, the velocity and the confinement of the surface plasmons can be varied. A further series of periodic corrugations will lead to decoupling of the SPP modes into free space radiation, allowing for detection.

measure of SPP lifetime, and equally coupling (and decoupling) efficiency could also be gained by varying the number of features in the central region; more features would ultimately lead to an increase in confinement (leading to greater ohmic losses), and increased decoupling (through diffraction), with both factors leading to shorter SPP lifetimes. Having a greater understanding of SPP confinement would allow for the development of much more sensitive SPP devices.

Further experiments could also be conducted to probe the fundamentals of the 'spoof' SPP model, by observing at what length scale sub-wavelength features begin to change the spatial confinement (and velocity) of the SPP modes. Increasing the confinement of SPP modes ultimately acts to increase the sensitivity of any plasmonic device exploited for sensor applications. If the length scales of these structures prove to be extremely sub-wavelength, i.e. $< 1$ $\mu$m, a different fabrication approach must be taken due the limits of standard, university-based lithographic processing. One possible process would look to fabricate aperture arrays from nanoporous nickel [238]. This electrochemical dealloying process can be used to create three-dimensional networks of interconnected pores, the dimensions of which are governed by the electric potential used in the electrochemical deposition process. By varying the dimensions of the pores, the confinement of any SPP modes could be varied, and tuned accordingly, ultimately allowing for more sensitive

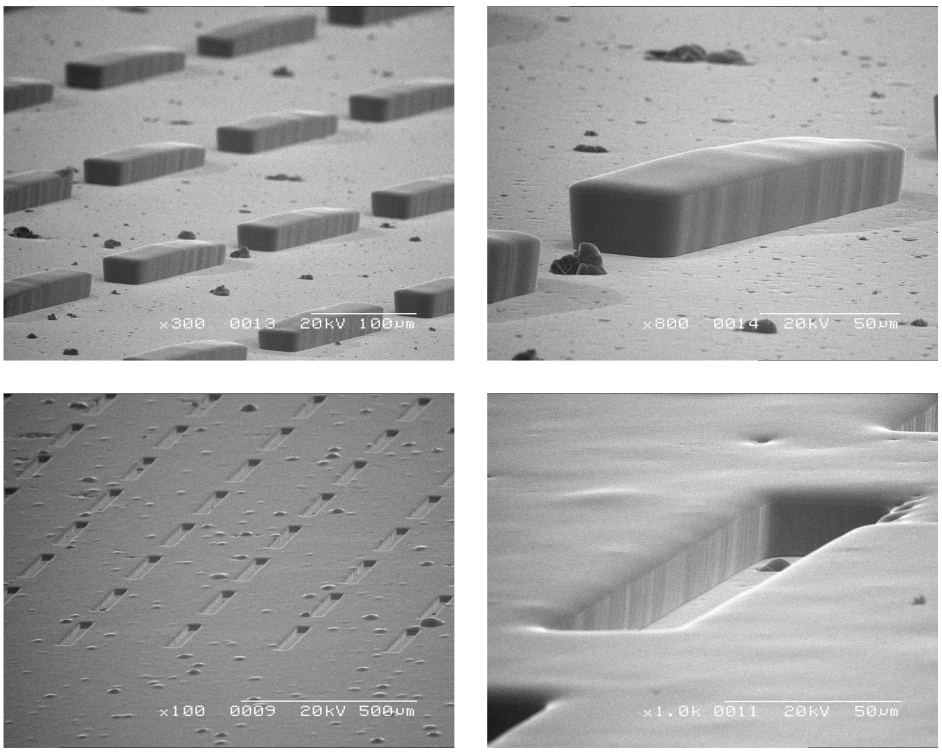


Figure 8.2: SEM images of complimentary periodic structures which could be used as a possible means to investigate the confinement and velocity of SPPs.

devices.

One final, intriguing experiment could be used to settle the long running debate as to whether a surface EM mode can be excited on liquid water [239,240]. Previous approaches have adopted a standard knife edge cut-off to attempt to couple to these modes. A novel suggestion would be to replace a copper foil, with water structured in the same manner. This could be achieved by fabricating a silicon chamber, structured with a periodic array of pillars. By ensuring the chamber is deep enough to block any direct transmission, the only transmission which could occur is through the 'apertures' in the liquid (through the silicon pillars), from a resonant SPP-like contribution sustained on the surface of the liquid. Such transmission would manifest itself as a decaying temporal oscillation, as typically observed for the metallic aperture arrays. If resonant transmission was found to occur, it could be exploited for sensor applications, assuming the temporal characteristics of the transmission process are dictated by the dielectric properties of the liquid.

# References


[1] J. M. Chamberlain, "Where optics meets electronics: Recent progress in decreasing the terahertz gap," *Phil. Trans. R. Soc. Lond. A*, vol. 362, no. 1815, pp. 199 – 213, 2004.

[2] E. Castro-Camus and M. B. Johnston, "Conformational changes of photoactive yellow protein monitored by terahertz spectroscopy," *Chem. Phys. Lett.*, vol. 455, pp. 289 – 292, 2008.

[3] J. Xu, K. W. Plaxco, and S. J. Allen, "Probing the collective vibrational dynamics of a protein in liquid water by terahertz absorption spectroscopy," *Protein Sci.*, vol. 15, pp. 1175 – 1181, 2006.

[4] B. M. Fischer, M. Walther, and P. U. Jepsen, "Far-infrared vibrational modes of DNA components studied by terahertz time-domain spectroscopy," *Phys. Med. Biol.*, vol. 47, pp. 3807 – 3814, 2002.

[5] M. Brucherseifer, M. Nagel, P. H. Bolivar, H. Kurz, A. Bosserhoff, and P. Buttner, "Label-free probing of the binding state of DNA by time-domain terahertz sensing," *Appl. Phys. Lett.*, vol. 77, no. 24, pp. 4049 – 4051, 2000.

[6] M. Franz, B. Fischer, D. Abbott, and H. Helm, "Terahertz Study of Chiral and Racemic Crystals," in *Joint 31st International Conference on Infrared, Millimeter and Terahertz Waves and 14th International Conference on Teraherz Electronics*, (Shanghai), p. 230, September 2006.

[7] M. Walther, B. M. Fischer, and P. U. Jepsen, "Noncovalent intermolecular forces in polycrystalline and amorphous saccharides in the far infrared," *Chem. Phys.*, vol. 288, pp. 261 – 268, 2003.

[8] B. Born, S. J. Kim, S. Ebbinghaus, M. Gruebele, and M. Havenith, "The terahertz dance of water with the proteins: The effect of protein flexibility on the dynamical hydration shell of ubuquitin," *Faraday Discuss.*, vol. 141, pp. 161 – 173, 2009.

[9] B. Born, H. Weingartner, E. Brundermann, and M. Havenith, "Solvation dynamics of model peptides probed by terahertz spectroscopy. Observation of the onset of collective network motions," *J. Am. Chem. Soc.*, vol. 131, pp. 3752 – 3755, 2009.

[10] S. Ebbinghaus, S. J. Kim, M. Heyden, X. Yu, U. Heugen, M. Gruebele, D. M. Letiner, and M. Havenith, "An extended dynamical hydration shell around proteins," *PNAS*, vol. 104, no. 52, pp. 20749 – 20752, 2007.

[11] D. M. Leitner, M. Gruebele, and M. Havenith, "Solvation dynamics of biomolecules: Modeling and terahertz experiments," *HFSP Journal*, vol. 2, no. 6, pp. 314 – 323, 2008.

[12] D. A. Schmidt, O. Birer, S. Funkner, B. P. Born, R. Gnanasekaran, G. W. Schwabb, D. M. Leitner, and M. Havenith, "Rattling in the cage: Ions as probes of sub-picosecond water network dynamics," *J. Am. Chem. Soc.*, vol. 131, pp. 18512 – 18517, 2009.

[13] D. Auston, K. Cheung, and P. Smith, "Picosecond photoconducting hertzian dipoles," *Appl. Phys. Lett.*, vol. 45, no. 3, pp. 284–286, 1984.

[14] C. Fattinger and D. Grischkowsky, "Point source terahertz optics," *Appl. Phys. Lett.*, vol. 53, no. 16, pp. 1480–1482, 1988.

[15] Q. Wu and X. C. Zhang, "Electrooptic sampling of freely propagating terahertz fields," *Opt. Quant. Electron*, vol. 28, pp. 945–951, 1996.

[16] P. U. Jepsen, U. Moller, and H. Merbold, "Investigation of aqueous alcohol and sugar solutions with reflection terahertz time-domain spectroscopy," *Opt. Express*, vol. 15, no. 22, pp. 14717 – 14737, 2007.

[17] P. U. Jepsen, J. Kristin, and U. Moller, "Characterisation of aqueous alcohol solutions in bottles with THz reflection spectroscopy," *Opt. Express*, vol. 16, no. 13, pp. 9318 – 9331, 2008.

[18] P. U. Jepsen and H. Merbold, "Terahertz reflection spectroscopy of aqueous NaCl and LiCl solutions," *J. Infrared Millim. Te.*, vol. 31, pp. 430 – 440, 2010.

[19] N. Kaun, J. R. Baena, D. Newnham, and B. Lendl, "Terahertz pulsed spectroscopy as a new tool for measuring the structuring of solutes on water," *Appl. Spectrosc.*, vol. 59, no. 4, pp. 505 – 510, 2005.

[20] J. T. Kindt and C. A. Schmuttenmaer, "Far-infrared dielectric properties of polar liquids probed by femtosecond terahertz pulse spectroscopy," *J. Phys. Chem.*, vol. 100, pp. 10373 – 10379, 1996.

[21] H. Kitahara, T. Yagi, K. Mano, M. W. Takeda, S. Kojima, and S. Nishizawa, "Dielectric characteristics of water solutions of ethanol in the terahertz region," *J. Korean Phys. Soc.*, vol. 46, no. 1, pp. 82 – 85, 2005.

[22] A. Stoppa, J. Hunger, R. Buchner, G. Hefter, A. Thoman, and H. Helm, "Interactions and dynamics in ionic liquids," *Phys. Chem. Lett. B*, vol. 112, pp. 4854 – 4858, 2008.

[23] D. S. Venables and C. A. Schmuttenmaer, "Spectroscopy and dynamics of mixtures of water with acetone, acetonitrile and methanol," *J. Chem. Phys.*, vol. 24, pp. 11222 – 11236, 2000.

[24] D. S. Venables, A. Chiu, and C. A. Schmuttenmaer, "Structure and dynamics of nonaqueous mixtures on dipolar liquids. 1. Infrared and far-infrared spectroscopy," *J. Chem. Phys.*, vol. 8, pp. 3243 – 3248, 2000.

[25] D. S. Venables and C. A. Schmuttenmaer, "Far-infrared spectra and associated dynamics in acetonitrile-water mixtures measured with femtosecond THz pulse spectroscopy," *J. Chem. Phys.*, vol. 108, no. 12, pp. 4935 – 4944, 1998.

[26] J. K. Vij, D. R. J. Simpson, and O. E. Panarina, "Far infrared spectroscopy of water at different temperatures: GHz to THz dielectric spectroscopy of water," *J. Mol. Liq.*, vol. 112, pp. 125 – 135, 2003.

[27] H. Yada, M. Nagai, and K. Tanaka, "The intermolecular stretching vibration mode in water isotopes investigated with broadband terahertz time-domain spectroscopy," *Chem. Phys. Lett.*, vol. 473, pp. 279 – 283, 2009.

[28] L. Zhou, W. Xu, B. Jin, J. Chen, L. Kang, and P. Wu, "Research on terahertz time-domain spectroscopy methodology of liquid samples," *Science China*, vol. 53, no. 4, pp. 1012 – 1015, 2010.

[29] K. Kawase, Y. Ogawa, Y. Watanabe, and H. Inouse, "Non-destructive terahertz imaging of illicit drugs using spectral Fingerprints," *Opt. Express*, vol. 11, no. 20, pp. 2549–2554, 2003.

[30] A. G. Davies, A. D. Burnett, W. H. Fan, E. H. Linfield, and J. E. Cunningham, "Terahertz spectroscopy of explosives and drugs," *Mater. Today*, vol. 11, no. 3, pp. 18 – 26, 2008.

[31] R. A. Cheville and D. Grischkowsky, "Time domain terahertz impulse ranging studies," *Appl. Phys. Lett.*, vol. 67, no. 14, pp. 1960–1962, 1995.

[32] E. Abraham, A. Younus, J. C. Delagnes, and P. Mounaix, "Non-invasive investigation of art paintings by terahertz imaging," *Appl. Phys. A*, vol. 100, no. 3, pp. 585–590, 2010.

[33] C. D. Stoik, M. J. Bohn, and J. L. Blackshire, "Nondestructive evaluation of aircraft composites using transmissive terahertz time domain spectroscopy," *Opt. Express*, vol. 16, no. 21, pp. 17039–17051, 2008.

[34] A. J. Fitzgerald, V. P. Wallace, M. Jimenez-Linan, L. Bobrow, R. J. Pye, A. D. Purushotham, and D. D. Arnone, "Terahertz Pulsed Imaging of Human Breast Tumors," *Radiology*, vol. 239, no. 2, pp. 533 – 540, 2006.

[35] H. Raether, *Surface plasmons on smooth and rough surfaces and on gratings*. 111, Berlin: Springer-Verlag, 1988.

[36] V. M. Agranovich and D. L. Mills, eds., *Surface Polaritons: Electromagnetic Waves at Surfaces and Interfaces*. Modern Problems in Condensed Matter Sciences, Amsterdam: North Holland Publishing Company, 1982.

[37] T. W. Ebbesen, H. J. Lezec, H. F. Ghaemi, T. Thio, and P. A. Wolff, "Extraordinary transmission through sub-wavelength hole arrays," *Nature*, vol. 391, pp. 667 – 669, 1998.

[38] J. B. Pendry, L. Martin-Moreno, and F. J. Garcia-Vidal, "Mimicking surface plasmons with structured surfaces," *Science*, vol. 305, pp. 847 – 848, 2004.

[39] W. Zhang, "Resonant terahertz transmission in plasmonic arrays of subwavelength holes," *Eur. Phys. J. Apply. Phys.*, vol. 43, pp. 1 – 18, 2008.

[40] C. Janke, J. G. Rivas, C. Schotsch, L. Beckmann, P. H. Bolivar, and H. Kurz, "Optimisation of enhanced terahertz transmission through arrays of subwavelength apertures," *Phys. Rev. B*, vol. 69, no. 20, 205314, 2004.

[41] H. Yoshida, Y. Ogawa, Y. Kawai, S. Hayashi, A. Hayashi, C. Otani, E. Kato, F. Miyamaru, and K. Kawase, "Terahertz sensing method for protein detection method using a thin metallic mesh," *Appl. Phys. Lett.*, vol. 91, no. 25, 253901, 2007.

[42] J. Han, X. Lu, and W. Zhang, "Terahertz transmission in subwavelength holes of asymmetric metal-dielectric interfaces: The effect of the dielectric layer," *J. Appl. Phys.*, vol. 103, no. 3, 033108, 2008.

[43] S. A. Maier, S. R. Andrews, L. Martin-Moreno, and F. J. Garcia-Vidal, "Terahertz surface plasmon-polariton propagation and focussing on periodically corrugated metal wires," *Phys. Rev. Lett.*, vol. 97, no. 17, 176805, 2006.

[44] K. Ishihara, G. Hatakoshi, T. I. H. Minamide, H. Ito, and K. Ohashi, "Terahertz wave enhanced transmission through a single sub wavelength aperture with periodic surface structures," *Jpn. J. Appl. Phys.*, vol. 44, no. 32, pp. L1005 – L1007, 2005.

[45] M. van Exter, C. Fattinger, and D. Grischkowsky, "Terahertz time-domain spectroscopy of water vapor," *Opt. Lett.*, vol. 14, no. 20, pp. 1128–1130, 1989.

[46] J. T. Lu and J. C. Cao, "Terahertz generation and chaotic dynamics in GaN NDR diode," *Semicond. Sci. Technol.*, vol. 19, no. 3, pp. 451 – 456, 2004.

[47] O. Cojocari, B. Mottet, M. Rodriguez-Girones, S. Biber, L. Marchand, L.-P. Schmidt, and H. L. Hartnagel, "A new structural approach for uniform submicrometer anode metallization of planar THz Schottky components," *Semicond. Sci. Technol.*, vol. 19, pp. 537 – 542, 2004.

[48] R. Köhler, A. Tredicucci, F. Beltram, H. E. Beere, E. H. Linfield, A. G. Davies, D. A. Ritchie, R. C. Iotti, and F. Rossi, "Terahertz semiconductor-heterostructure laser," *Nature*, vol. 417, pp. 156 – 159, 2002.

[49] C. Walther, M. Fischer, G. Scalari, R. Terazzi, N. Hoyler, and J. Faist, "Quantum cascade lasers operating from 1.2 To 1.6 THz," *Appl. Phys. Lett.*, vol. 91, no. 13, 131122, 2007.

[50] S. Kumar, C. I. Chan, Q. Hu, and J. L. Reno, "A 1.8-THz quantum cascade laser operating significantly above the temperature of $\hbar\omega/k_B$," *Nat. Phys.*, vol. 7, no. 2, pp. 166–171, 2011.

[51] J. R. Freeman, J. Madéo, A. Brewer, S. Dhillon, O. P. Marshall, N. Jukam, D. Oustinov, J. Tignon, H. E. Beere, and D. A. Ritchie, "Dual wavelength emission from a terahertz quantum cascade laser," *Appl. Phys. Lett.*, vol. 96, no. 5, 051120, 2010.

[52] G. W. Chantry, *Long-wave Optics, The Science and Technology of Infrared and Near-Millimetre Waves*, vol. 2 - Applications. London: Academic Press Inc., 1984.

[53] M. Y. Tretyakov, S. A. Volokhov, G. Y. Golubyatnikov, E. N. Karyakin, and A. F. Krupnov, "Compact Tunable Radiation Source at 180 – 1500 GHz Frequency Range," *Int. J. Infrared Milli.*, vol. 20, no. 8, pp. 1443 – 1451, 1999.

[54] A. Dobroiu, M. Yamashita, Y. N. Ohshima, Y. Morita, C. Otani, and K. Kawase, "Terahertz imaging system based on a backward-wave oscillator," *Appl. Optics*, vol. 43, no. 30, pp. 5637 – 5646, 2004.

[55] Y. Cai, I. Brener, J. Lopata, J. Wynn, and L. Pfeiffer, "Design and Performance of singular electric field terahertz photoconducting antennas," *Appl. Phys. Lett.*, vol. 71, no. 15, pp. 2076 – 2078, 1997.

[56] Z. Piao, M. Tani, and K. Sakai, "Carrier Dynamics and Terahertz Radiation in Photoconductive Antennas," *Jpn. J. Appl. Phys.*, vol. 39, no. 1, pp. 96–100, 2000.

[57] I. S. Gregory, C. Baker, W. R. Tribe, M. J. Evans, H. E. Beere, E. H. Linfield, A. G. Davies, and M. Missous, "High resistivity annealed low-temperature GaAs with 100 fs lifetimes," *Appl. Phys. Lett.*, vol. 83, no. 20, pp. 4199–4201, 2003.

[58] G. Zhao, R. N. Schouten, N. van der Valk, W. T. Wenckebach, and P. C. M. Planken, "Design and performance of a THz emission and detection setup based on a semi-insulating GaAs emitter," *Rev. Sci. Instrum.*, vol. 73, no. 4, pp. 1715–1719, 2002.

[59] S.-G. Park, M. R. Melloch, and A. M. Weiner, "Comparison of terahertz waveforms measured by electro-optic and photoconductive sampling," *Appl. Phys. Lett.*, vol. 73, no. 22, pp. 3184–3186, 1998.

[60] T.-A. Liu, M. Tani, M. Nakajima, M. Hangyo, and C.-L. Pan, "Ultrabroadband terahertz field detection by photoconductive antennas based on multi-energy arsenic-ion-implanted GaAs and semi-insulating GaAs," *Appl. Phys. Lett.*, vol. 83, no. 7, pp. 1322–1324, 2003.

[61] P. U. Jepsen and B. M. Fischer, "Dynamic range in terahertz time-domain transmission and reflection spectroscopy," *Opt. Lett.*, vol. 30, no. 1, pp. 29 – 31, 2005.

[62] P. C. Ashworth, *Biomedical Applications of Terahertz Technology*. PhD thesis, University of Cambridge, 2010.

[63] P. A. George, W. Hui, F. Rana, B. G. Hawkins, A. E. Smith, and B. J. Kirby, "Microfluidic device for terahertz spectroscopy of biomolecules," *Opt. Express*, vol. 16, no. 3, pp. 1577 – 1582, 2008.

[64] A. G. Markelz, "Terahertz dielectric sensitivity to biomolecular structure and function," *IEEE J. Sel. Top. Quant.*, vol. 14, no. 1, pp. 180 – 190, 2008.

[65] P. H. Bolivar, M. Brucherseifer, J. G. Rivas, R. Gonzalo, I. Ederra, A. L. Reynolds, M. Holker, and P. de Maagt, "Measurement of the dielectric constant and loss tangent of high dielectric-constant materials at terahertz frequencies," *IEEE T. Microw. Theory*, vol. 51, no. 4, pp. 1062 – 1066, 2003.

[66] L. Duvillaret, F. Garet, and J. Coutaz, "A reliable method for extraction of material parameters in terahertz time-domain spectroscopy," *IEEE J. Sel. Top. Quant.*, vol. 2, no. 3, pp. 739 – 745, 1996.

[67] L. Duvillaret, F. Garet, and J. Coutaz, "Highly precise determination of optical constants and sample thickness in terahertz time-domain spectroscopy," *Appl. Opt.*, vol. 38, no. 2, pp. 409 – 415, 1999.

[68] W. Withayachumnankul, B. Ferguson, T. Rainsford, S. P. Mickan, and D. Abbott, "Material parameter extraction for terahertz time-domain spectroscopy using fixed-point iteration," *Proc. of SPIE*, vol. 5840, pp. 221 – 231, 2005.

[69] T. D. Dorney, R. G. Baraniuk, and D. M. Mittleman, "Material parameter estimation with terahertz time-domain spectroscopy," *J. Opt. Soc. Am. A.*, vol. 18, no. 7, pp. 1562 – 1571, 2001.

[70] D. Zhou, E. P. J. Parrott, D. J. Paul, and J. A. Zeitler, "Determination of complex refractive index of thin metal films from terahertz time-domain spectroscopy," *J. Appl. Phys.*, vol. 104, no. 5, 053110, 2008.

[71] E. P. J. Parrott, J. A. Zeitler, L. F. Gladden, S. N. Taraskin, and S. R. Elliott, "Extracting accurate optical parameters from glasses using terahertz time-domain spectroscopy," *J. Non-Cryst. Solids*, vol. 335, pp. 1824 – 1827, 2009.

[72] M. Scheller, C. Jansen, and M. Koch, "Analysing sub-100-um samples with transmission terahertz time domain spectroscopy," *Opt. Commun.*, vol. 282, pp. 1304 – 1306, 2009.

[73] M. Naftaly and R. E. Miles, "A method for removing etalon oscillations from THz time-domain spectra," *Opt. Commun.*, vol. 280, pp. 291 – 295, 2007.

[74] I. Pupeza, R. Wilk, and M. Koch, "Highly accurate optical material parameter determination with THz time-domain spectroscopy," *Opt. Express*, vol. 15, no. 7, pp. 4335 – 4350, 2005.

[75] M. Scheller and M. Koch, "Fast and accurate thickness determination of unknown materials using terahertz time domain spectroscopy," *J. Infrared. Millim. Te.*, vol. 30, pp. 762 – 769, 2009.

[76] B. Yu, F. Zeng, Y. Yang, Q. Xing, A. Chechin, X. Xin, I. Zeylikovich, and R. R. Alfano, "Torsional vibrational modes of tryptophan studied by terahertz time-domain spectroscopy," *Biophys. J.*, vol. 86, no. 3, pp. 1649 – 1654, 2004.

[77] K. M. Tych, A. D. Burnett, C. D. Wood, J. E. Cunningham, A. R. Pearson, A. G. Daviesa, and E. H. Linfield, "Applying broadband terahertz time-domain spectroscopy to the analysis of crystalline proteins: A dehydration study," *J. Appl. Crystallogr.*, vol. 44, pp. 129–133, 2011.

[78] J. Y. Chen, J. R. Knab, S. Ye, Y. He, and A. G. Markelz, "Terahertz dielectric assay of solution phase protein binding," *Appl. Phys. Lett.*, vol. 90, no. 24, 243901, 2007.

[79] A. Abbas, P. Supiot, V. Mille, D. Guillochon, and D. Bocquet, "Capillary microchannel fabrication using plasma polymerized TMDS for fluidic MEMS technology," *J. Micromech. Microeng.*, vol. 19, no. 4, 045022, 2009.

[80] N. Nguyen, C. Wang, T. N. Wong, L. N. Low, and S. S. Ho, "A silicon/glass based microfluidic device for investigation of lagrangain velocity field in microdroplets," *J. Phys. Conf. Ser.*, vol. 34, pp. 130 – 135, 2006.

[81] http://www.specac.com, SPECAC, Accessed April 2011.

[82] Y. W. Chen, P. Y. Han, and X. C. Zhang, "Tunable broadband antireflection structures for silicon at terahertz frequency," *Appl. Phys. Lett.*, vol. 94, no. 4, 041106, 2009.

[83] W. Withayachumnankul, B. M. Fischer, and D. Abbott, "Material thickness optimization for transmission-mode terahertz time domain spectroscopy," *Opt. Express*, vol. 16, no. 10, pp. 7382 – 7396, 2008.

[84] M. J. Madou, *Fundamentals of Microfabrication, The Science of Miniaturisation*. Boca Raton: CRC Press, 2002.

[85] B. Bahreyni and C. Shafai, "Investigation and simulation of $XeF_2$ isotropic etching of silicon," *J. Vac. Sci. Technol., A*, vol. 20, no. 6, pp. 1850–1855, 2002.

[86] M. Schmidt, "Wafer-to-wafer bonding for microstructure formation," *P. IEEE*, vol. 96, no. 8, pp. 1575 – 1585, 1998.

[87] U. Gosele, Q. Y. Tong, A. Schumacher, G. Krauter, M. Reiche, A. Plosl, P. Kopperschmidt, T. H. Lee, and W. J. Kim, "Wafer bonding for Microsystems technology," *Sensor. Actuator*, vol. 74, pp. 161 – 168, 1999.

[88] U. Gosele and Q. Y. Tong, "Semiconductor Wafer Bonding," *Annu. Rev. Mater. Sci.*, vol. 28, pp. 215 – 241, 1998.

[89] Z. Liu and D. L. DeVoe, "Micromechanism fabrication using silicon fusion bonding," *Robot. Cim-Int. Manuf.*, vol. 17, pp. 131 – 137, 2001.

[90] X. Lin, G. Liao, Z. Tang, and T. Shi, "UV surface exposure for low temperature hydrophilic silicon direct bonding," *Microsyst. Technol.*, vol. 15, pp. 317 – 321, 2009.

[91] C. Gui, H. Albers, J. G. E. Gardeniers, M. Elwenspeek, and P. V. Lambeck, "Fusion bonding of rough surfaces with polishing technique for silicon micromachining," *Microsyst. Technol.*, vol. 128, pp. 122 – 128, 1997.

[92] X. X. Zhang and J. Raskin, "Low-temperature wafer bonding: A study of void formation and influence on bonding strength," *J. Microelectromech. S.*, vol. 14, no. 2, pp. 368 – 382, 2005.

[93] H. Takagi, R. Maeda, T. R. Chung, and T. Suga, "Low-temperature direct bonding of silicon and silicon dioxide by the surface activation method," *Sensor Actuat. A-Phys*, vol. 70, pp. 164 – 170, 1998.

[94] A. Berthold, B. Jokoby, and M. J. Vellekoop, "Wafer-to-wafer fusion bonding of oxidised silicon to silicon at low temperatures," *Sensor Actuat. A-Phys*, vol. 68, pp. 410 – 413, 1998.

[95] C. Wang, E. Higurashi, and T. Suga, "Void-free room-temperature silicon wafer birect bonding using sequential plasma activation," *Jpn. J. Appl. Phys.*, vol. 47, no. 4, pp. 2526 – 2530, 2008.

[96] O. Zucker, W. Langhemrich, M. Kulozik, and H. Goebel, "Application of oxygen plasma processing to silicon direct bonding," *Sensor Actuat. A-Phys*, vol. 36, pp. 227 – 231, 1993.

[97] P. R. Griffiths, *Chemical Infrared Fourier Transform Spectroscopy*. New York: John Wiley & Sons, 1975.

[98] P. R. Griffiths and J. A. de Haseth, *Fourier Transform Infrared Spectrometry*. New York: John Wiley & Sons, 1986.

[99] H. P. Merbold, *Terahertz time-domain spectroscopy of aqueous systems in reflection geometry*. PhD thesis, University of Frieburg, 2006.

[100] U. Møller, D. G. Cooke, K. Tanaka, and P. U. Jepsen, "Terahertz reflection spectroscopy of Debye relaxation in polar liquids [Invited]," *J. Opt. Soc. Am. B*, vol. 26, no. 9, pp. A113–A125, 2009.

[101] T. M. Korter and D. F. Plusquellic, "Continuous-wave terahertz spectroscopy of biotin: Vibrational anharmonicity in the far-infrared," *Chem. Phys. Lett.*, vol. 385, pp. 45 – 51, 2004.

[102] E. C. L. Ru and P. G. Etchegoin, *Principles of surface-enhanced Raman spectroscopy*. Oxford: Elsevier, 2009.

[103] B. Liedberg, C. Nylander, and I. Lundstrom, "Surface plasmon resonance for gas detection and biosensing," *Sensor. Actuator.*, vol. 4, pp. 299 – 304, 1983.

[104] K. Kneipp, Y. Wang, H. Kneipp, L. T. Perelman, I. Itzkan, R. Dasari, and M. S. Fields, "Single molecule detection using surface-enhanced Raman scattering (SERS)," *Phys. Rev. Lett.*, vol. 78, no. 9, pp. 1667 – 1670, 1997.

[105] T. Holmgaard, S. I. Bozhevolnyi, L. Markey, A. Dereux, A. V. Krasavin, P. Bolger, and A. V. Zayats, "Efficient excitation of dielectric-loaded surface plasmon-polariton waveguide modes at telecommunication wavelengths," *Phys. Rev. B*, vol. 78, no. 16, 165431, 2008.

[106] C. R. Williams, S. R. Andrews, S. A. Maier, A. I. Fernandez-Dominquez, L. Martin-Moreno, and F. J. Garcia-Vidal, "Highly confined guiding of terahertz surface plasmon polaritons on structured metal surfaces," *Nat. Photon.*, vol. 2, pp. 175 – 179, 2008.

[107] M. Bai, C. Guerrero, S. Ioanid, E. Paz, M. Sanz, and N. García, "Measuring the speed of a surface plasmon," *Phys. Rev. B*, vol. 69, no. 11, 115416, 2004.

[108] R. W. Alexander, G. S. Kovener, and R. J. Bell, "Dispersion curves for surface electromagnetic waves with damping," *Phys. Rev. Lett.*, vol. 32, pp. 154 – 157, 1974.

[109] G. S. Kovener, R. W. A. Jr, and R. J. Bell, "Surface electromagnetic waves with damping. I. Isotropic media," *Phys. Rev. B*, vol. 14, no. 4, pp. 1458 – 1464, 1976.

[110] A. Otto, "Excitation of nonradiative surface plasma waves in silver by method of frustrated total reflection," *Z. Phys.*, vol. 216, pp. 398 – 410, 1968.

[111] E. Kretschmann and H. Raether, "Radiative decay of non radiative surface plasmons excited by light," *Z. Naturf. A*, vol. 23, p. 2135, 1968.

[112] B. Liedberg, C. Nylander, and I. Lundstrom, "Biosensing with surface plasmon resonance how it all started," *Biosens. Bioelectron.*, vol. 10, pp. i – ix, 1995.

[113] A. K. Azad, *Resonant terahertz transmission of plasmonic subwavelength hole arrays*. PhD thesis, Oklahoma State University, 2006.

[114] J. Saxler, *Surface Plasmon Polaritons at Terahertz Frequencies on Metal and Semiconductor Surfaces*. PhD thesis, Aachen University, 2003.

[115] H. A. Bethe, "Theory of diffraction by small holes," *Phys. Rev.*, vol. 66, pp. 163 – 182, 1944.

[116] C. Genet and T. W. Ebbesen, "Light in tiny holes," *Nature*, vol. 445, pp. 39 – 44, 2007.

[117] R. W. Wood, "On a remarkable case of uneven distribution of light in a diffraction grating spectrum," *Philosophical Magazine*, vol. 4, pp. 396 – 402, 1902.

[118] J. W. S. Rayleigh, "Note on the remarkable case of diffraction spectra described by Prof Wood," *Philospohical Magazine Series 6*, vol. 14, no. 79, pp. 60 – 65, 1907.

[119] J. Strong, "Effect of evaporated films on energy distribution in grating spectra," *Phy. Rev.*, vol. 49, pp. 291 – 296, 1936.

[120] M. C. Hutley and V. M. Bird, "A detailed experimental study of the anomalies of a sinusoidal diffraction grating," *Optica Acta*, vol. 20, no. 10, pp. 771 – 782, 1973.

[121] Y. Teng and E. Stern, "Plasma radiation from metal grating surfaces," *Phys. Rev. Lett.*, vol. 19, no. 9, pp. 511 – 514, 1967.

[122] A. Mitsuishi, Y. Otsuka, S. Fujita, and H. Yoshinaga, "Metal mesh filters in the far infrared region," *Jap. J. Appl. Phys.*, vol. 2, no. 9, pp. 575 – 578, 1963.

[123] R. Ulrich, "Far-infrared properties of metallic mesh and its complimentary structure," *Infrared Physics*, vol. 7, no. 1, pp. 37 – 50, 1966.

[124] J. V. Coe, J. M. Heer, S. Teeters-Kennedy, H. Tian, and K. R. Rodriquez, "Extraordinary transmission of metal films with arrays of subwavelength holes," *Annu. Rev. Phys. Chem.*, vol. 59, pp. 179 – 202, 2008.

[125] R. Ulrich, "Modes of propagation on an open periodic waveguide for the far infrared," in *Symp. Opt. Acoust. Microelectron.*, (Brooklyn Polytechn. Inst. New York), pp. 359 – 376, April 1974.

[126] U. Fano, "The theory of anomalous diffraction gratings and of quasi-stationary waves on metallic surfaces: Sommerfeld's Waves," *J. Opt. Soc. Am.*, vol. 31, pp. 213 – 222, 1941.

[127] C. Winnewisser, F. Lewen, and H. Helm, "Transmission characteristics of dichroic filters measured by THz time-domain spectroscopy," *Appl. Phys. A*, vol. 66, pp. 593 – 598, 1998.

[128] D. L. Mills and E. Burstein, "Polaritons: The electromagnetic modes of media," *Rep. Prog. Phys.*, vol. 37, pp. 817 – 926, 1974.

[129] F. Yang, J. R. Sambles, and G. W. Bradberry, "Long-range surface modes supported by thin films," *Phys. Rev. B*, vol. 44, no. 11, pp. 5855 – 5872, 1991.

[130] J. Zenneck, "Über die Fortpflanzung ebener elektromagnetischer Wellen längs einer ebenen Leiterfläche und ihre Beziehung zur drahtlosen Telegraphie," *Ann. Phys.*, vol. 23, pp. 846 – 866, 1907.

[131] D. Schumacher, C. Rea, D. Heitmann, and K. Scharnberg, "Surface plasmons and Sommerfeld-Zenneck waves on corrugated surfaces: Application to high-Tc superconductors," *Surface Sciecne*, vol. 408, pp. 203 – 210, 1998.

[132] G. Goubau, "Surface waves and their application to transmission lines," *J. Appl. Phys.*, vol. 21, pp. 1119 – 1128, 1950.

[133] J. G. Rivas, C. Schotsch, P. H. Bolivar, and H. Kurz, "Enhanced transmission of THz radiation through subwavelength holes," *Phys. Rev. B*, vol. 68, no. 20, 201306R, 2003.

[134] D. Qu, D. Grischkowsky, and W. Zhang, "Terahertz transmission of thin, subwavelength metallic hole arrays," *Opt. Lett.*, vol. 29, no. 8, pp. 896 – 898, 2004.

[135] A. K. Azad, Y. Zhao, and W. Zhang, "Transmission properties of terahertz pulses through an ultrathin subwavelength silicon hole array," *Appl. Phys. Lett.*, vol. 86, no. 14, 141102, 2005.

[136] M. Tanaka, F. Miyamaru, M. Hangyo, T. Tanaka, M. Akazawa, and E. Sano, "Effect of a thin dielectric layer on terahertz transmission characteristics for metal hole arrays," *Opt. Lett.*, vol. 30, no. 10, pp. 1210–1212, 2005.

[137] J. Saxler, J. G. Rivas, C. Janke, H. P. M. Pellemans, P. H. Bolivar, and H. Kurz, "Time-domain measurements of surface plasmon polaritons in the terahertz frequency range," *Phys, Rev. B*, vol. 69, no. 15, 155427, 2005.

[138] A. Agrawal and N. Nahata, "Time-domain radiative properties of a single subwavelength aperture surrounded by an exit side surface corrugation," *Opt. Express*, vol. 14, no. 5, pp. 1973 – 1981, 2006.

[139] K. Ishihara, K. Ohashi, T. Ikari, H. Minamide, H. Yokoyama, J. I. Shikata, and H. Ito, "Terahertz-wave near-field imaging with subwavelength resolution using surface-wave-assisted bow-tie aperture," *Appl. Phys. Lett.*, vol. 89, no. 20, 201120, 2006.

[140] A. P. Hibbins, E. Hendry, M. J. Lockyear, and J. R. Sambles, "Prism coupling to 'designer' surface plasmons," *Opt. Express*, vol. 20, no. 20, 20441, 2008.

[141] W. L. Barnes, W. A. Murray, J. Dintinger, E. Devaux, and T. W. Ebbesen, "Surface plasmon polaritons and their role in the enhanced transmission of light through periodic arrays of subwavelength holes in a metal film," *Phys. Rev. Lett.*, vol. 92, no. 10, 107401, 2004.

[142] S. A. Darmanyan and A. V. Zayats, "Light tunnelling via resonant surface plasmon polariton states and the enhanced transmission of periodically nanostructured metal films: An analytical study," *Phys. Rev. B*, vol. 67, no. 3, 035424, 2003.

[143] A. Degiron and T. W. Ebbesen, "The role of localised surface plasmon modes in enhanced transmission of periodic subwavelength apertures," *J. Opt. A: Pure Appl. Opt.*, vol. 7, pp. S90 – S96, 2005.

[144] Z. Fan, L. Zhan, X. Hu, and Y. Xia, "Critical process of extraordinary optical transmission through periodic subwavelength hole array: Hole-assisted evanescent-field coupling," *Opt. Commun.*, vol. 281, pp. 5467 – 5471, 2008.

[145] H. F. Ghaemi, T. Thio, D. E. Grupp, T. W. Ebbesen, and H. J. Lezec, "Surface plasmons enhance optical transmission through subwavelength holes," *Phys. Rev. B*, vol. 58, no. 11, pp. 6779 – 6782, 1998.

[146] A. Krishnan, T. Thio, T. J. Kim, H. J. Lezec, T. W. Ebbesen, P. A. Wolff, J. Pendry, L. Martin-Moreno, and F. J. Garcia-Vidal, "Evanescently coupled resonance in surface plasmon enhanced transmission," *Opt. Commun.*, vol. 200, pp. 1 – 7, 2001.

[147] L. Martin-Moreno, F. J. Garcia-Vidal, H. J. Lezec, K. M. Pellerin, T. Thio, J. B. Pendry, and T. W. Ebbesen, "Theory of extraordinary optical transmission through subwavelength hole arrays," *Phys. Rev. Lett.*, vol. 86, no. 6, pp. 1114 – 1117, 2001.

[148] A. Mary, S. G. Rodrigo, L. Martin-Moreno, and F. J. Garcia-Vidal, "Theory of light transmission through an array of rectangular holes," *Phys. Rev. B*, vol. 76, no. 15, 159414, 2007.

[149] Z. Ruan and M. Qui, "Enhanced transmission through periodic arrays of subwavelength holes The role of localised waveguide resonances," *Phys. Rev. Lett.*, vol. 96, no. 23, 233901, 2006.

[150] U. Schroter and D. Heitmann, "Surface plasmon enhanced transmission through metallic gratings," *Phys. Rev. B*, vol. 58, no. 23, pp. 15419 – 15421, 1998.

[151] M. M. J. Treacy, "Dynamical diffraction explanation of the anomalous transmission of light through metallic gratings," *Phys. Rev. B*, vol. 66, no. 19, 195105, 2002.

[152] J. M. Vigoureux, "Analysis of the Ebbesen experiment in the light of evanescent short range diffraction," *Opt. Commun.*, vol. 198, no. 4 - 6, pp. 257 – 263, 2001.

[153] S. M. Williams and J. V. Coe, "Dispersion study of the infrared transmission resonances of freestanding Ni Microarrays," *Plasmonics*, vol. 1, pp. 87 – 93, 2006.

[154] H. Cao and A. Nahata, "Resonantly enhanced transmission of terahertz radiation through a periodic array of subwavelength apertures," *Opt. Express*, vol. 12, no. 6, pp. 1004 – 1010, 2004.

[155] A. K. Azad, Y. Zhao, W. Zhang, and M. He, "Effect of dielectric properties of metals on terahertz transmission in subwavelength hole arrays," *Opt. Lett.*, vol. 31, no. 17, pp. 2637 – 2639, 2006.

[156] A. K. Azad and W. Zhang, "Resonant terahertz transmission in subwavelength metallic hole arrays of sub-skin-depth thickness," *Opt. Lett.*, vol. 30, no. 21, pp. 2945 – 2947, 2005.

[157] D. Qu and D. Grischkowsky, "Observation of a new type of resonance of surface plasmons propagating on metal-film hole arrays," *Phys. Rev. Lett.*, vol. 93, no. 19, 196804, 2004.

[158] A. Degiron, H. J. Lezec, N. Yamamoto, and T. W. Ebbesen, "Optical transmission properties of a single subwavelength aperture in a real metal," *Opt. Commun.*, vol. 239, pp. 61 – 66, 2004.

[159] K. J. K. Koerkamp, S. Enoch, F. B. Segerink, N. F. van Hulst, and a. L. Kuipers, "Strong influence of hole shape on extraordinary transmission through periodic arrays of subwavelength holes," *Phys. Rev. Lett.*, vol. 92, no. 18, 183901, 2004.

[160] F. Miyamaru, M. Tanaka, and M. Hangyo, "Effect of hole diameter on terahertz surface-wave excitation in metal-hole arrays," *Phys. Rev. B*, vol. 74, no. 15, 153416, 2006.

[161] K. L. van der Molen, K. J. K. Koerkamp, S. Enoch, F. B. Segerink, N. F. van Hulst, and L. Kuipers, "Role of shape and localised resonance in extraordinary transmission through periodic arrays of subwavelength holes: Experiment and theory," *Phys. Rev. B*, vol. 72, no. 4, 045421, 2005.

[162] J. Han, A. K. Azad, M. Gong, X. Lu, and W. Zhang, "Coupling between surface plasmons and nonresonant transmission in subwavelength holes at terahertz frequencies," *Appl. Phys. Lett.*, vol. 91, no. 7, 071122, 2007.

[163] H. Cao and A. Nahata, "Influence of aperture shape on the transmission properties of a periodic array of subwavelength apertures," *Opt. Express*, vol. 12, no. 16, pp. 3664 – 3672, 2004.

[164] C. Genet, M. P. van Exeter, and J. P. Woerdman, "Fano-type interpretation of red shifts and red tails in hole array transmission spectra," *Opt. Commun.*, vol. 225, pp. 331 – 333, 2003.

[165] F. Miyamaru and M. W. Takeda, "Coupling between localized resonance and excitation of surface waves in metal hole arrays," *Phys. Rev. B*, vol. 79, no. 15, 153405, 2009.

[166] J. Bravo-Abad, L. Martín-Moreno, F. J. García-Vidal, E. Hendry, and J. G. Rivas, "Transmission of light through periodic arrays of square holes: From a metallic wire mesh to an array of tiny holes," *Phys. Rev. B*, vol. 76, no. 24, 241102R, 2007.

[167] F. Miyamaru and M. Hangyo, "Finite size effect of transmission property for metal hole arrays in subterahertz region," *Appl. Phys. Lett.*, vol. 84, no. 15, pp. 2742 – 2744, 2004.

[168] T. Matsui, A. Agrawal, A. Nahata, and Z. V. Vardeny, "Transmission resonances through aperiodic arrays of subwavelength apertures," *Nature*, vol. 446, pp. 517 – 521, 2007.

[169] B. B. Hu and M. C. Nuss, "Imaging with terahertz waves," *Opt. Lett.*, vol. 20, no. 16, pp. 1716–1718, 1995.

[170] L. Ho, R. Muller, M. Romer, K. C. Gordon, J. Heinamaki, P. Kleinebudde, M. Pepper, T. Rades, Y. C. Shen, C. J. Strachan, P. F. Taday, and J. A. Zeitler, "Analysis of sustained-release tablet film coats using terahertz pulsed imaging," *J. Control. Release*, vol. 119, no. 3, pp. 253–261, 2007.

[171] K. L. Wang and D. M. Mittleman, "Metal wires for terahertz wave guiding," *Nature*, vol. 432, no. 7015, pp. 376 – 379, 2004.

[172] M. M. Awad and R. A. Cheville, "Transmission terahertz waveguide-based imaging below the diffraction limit," *Appl. Phys. Lett.*, vol. 86, no. 22, 221107, 2005.

[173] N. C. J. van der Valk, W. A. M. van der Marel, and P. C. M. Planken, "Terahertz polarization imaging," *Opt. Lett.*, vol. 30, no. 20, pp. 2802–2804, 2005.

[174] H.-T. Chen, R. Kerstinga, and G. C. Cho, "Terahertz imaging with nanometer resolution," *Appl. Phys. Lett.*, vol. 83, no. 15, pp. 3009–3011, 2003.

[175] A. Gallant, A. J. Baragwanath, P. Swift, D. Wood, and M. Chamberlain, "Micromachined Terahertz Waveguides with Embedded Metal Rods," in *33rd international conference on infrared, millimeter and terahertz waves, vols 1 and 2*, (Pasadena, CA), pp. 104 – 105, September 2008.

[176] Q. Chen, Z. Jiang, G. X. Xu, and X.-C. Zhang, "Near-field terahertz imaging with a dynamic aperture," *Opt. Lett.*, vol. 25, no. 15, pp. 1122 – 1124, 2000.

[177] R. Degl'Innocenti, M. Montinaro, J. Xu, V. Piazza, P. Pingue, A. Tredicucci, F. Beltram, H. E. Beere, and D. A. Ritchie, "Differential Near-Field Scanning Optical Microscopy with THz quantum cascade laser sources," *Opt. Express*, vol. 17, no. 26, pp. 23785–23792, 2009.

[178] F. Miyamaru, M. W. Takeda, T. Suzuki, and C. Otani, "Highly sensitive surface plasmon terahertz imaging with planar plasmonic crystals," *Opt. Express*, vol. 15, no. 22, pp. 14804 – 14809, 2007.

[179] K. Ishihara, T. Ikari, H. Minimide, J. Shikate, K. Oshashi, H. Yokoyama, and H. Ito, "Terahertz near-field imaging using enhanced transmission through a single subwavelength aperture," *Jpn. J. Appl. Phys.*, vol. 44, no. 29, pp. L929 – L931, 2005.

[180] P. Maraghechi, C. Straatsma, Z. Liu, V. Zhao, and Y. Elezzabi, "Plasmon-assisted terahertz imaging inside metal-filled media," *Opt. Express*, vol. 17, no. 19, pp. 16546 – 16464, 2009.

[181] T. Thio, K. M. Pellerin, R. A. Linke, H. J. Lezec, and T. W. Ebbesen, "Enhanced light transmission through a single subwavelength aperture," *Opt. Lett.*, vol. 26, no. 24, pp. 1972–1974, 2001.

[182] H. Cao, A. Agrawal, and A. Nahata, "Controlling the transmission resonance lineshape of a single subwavelength aperture," *Opt. Express*, vol. 13, no. 3, pp. 763 – 769, 2005.

[183] A. Agrawal, H. Cao, and A. Nahata, "Excitation and scattering of surface plasmon-polaritions on structured metal films and their application to pulse shaping and enhanced transmission," *New J. Phys.*, vol. 7, p. 249, 2005.

[184] H. Lorenz, M. Despont, N. Fahrni, J. Brugger, P. Vettiger, and P. Renaud, "High-aspect-ratio, ultrathick, negative-tone near-UV photoresist and its applications for MEMS," *Sensor Actuat. A-Phys.*, vol. 64, no. 1, pp. 33 – 39, 1998.

[185] C. H. Lin, G. B. Lee, B. W. Chang, and G. L. Chang, "A new fabrication process for ultra-thick microfluidic microstructures utilizing SU-8 photoresist," *J. Micromech. Microeng.*, vol. 12, no. 5, pp. 590 – 597, 2002.

[186] S. Arscott, F. Garet, P. Mounaix, L. Duvillaret, J.-L. Coutaz, and D. Lippens, "Terahertz time-domain spectroscopy of films fabricated from SU-8," *Electron. Lett*, vol. 35, no. 3, pp. 243 – 244, 1999.

[187] A. J. Gallant, M. A. Kaliteevski, D. Wood, M. C. Petty, R. A. Abram, S. Brand, G. P. Swift, D. A. Zeze, and J. M. Chamberlain, "Passband filters for terahertz radiation based on dual metallic photonic structures," *Appl. Phys. Lett.*, vol. 91, no. 16, 161115, 2007.

[188] Y. Zhao and D. R. Grischkowsky, "2-D Terahertz Metallic Photonic Crystals in Parallel-Plate Waveguides," *IEEE T. Microw. Theory*, vol. 55, no. 4, pp. 656–633, 2007.

[189] S. Barbieri, J. Alton, H. E. Beere, J. Fowler, E. H. Linfield, and D. A. Ritchie, "2.9 THz quantum cascade lasers operating up to 70 K in continuous wave," *Appl. Phys. Lett.*, vol. 85, no. 10, pp. 1674–1676, 2004.

[190] S. Kumar, "Recent Progress in Terahertz Quantum Cascade Lasers," *IEEE J. Sel. Top. Quant.*, vol. 17, no. 1, pp. 38–47, 2011.

[191] F. J. Garcia-Vidal, L. Martin-Moredo, H. J. Lezec, and T. W. Ebbesen, "Focusing light with a single subwavelength aperture flanked by surface corrugations," *Appl. Phys. Lett.*, vol. 83, no. 22, pp. 4500 – 4502, 2003.

[192] S. M. Williams, *Characteristics and applications of the infrared enhanced transmission of metallic subwavelength arrays*. PhD thesis, Ohio State University, 2006.

[193] A. Degiron, H. J. Lezec, W. L. Barnes, and T. W. Ebbesen, "Effects of hole depth on enhanced light transmission through subwavelength hole arrays," *Appl. Phys. Lett.*, vol. 81, no. 23, pp. 4327–4329, 2002.

[194] D. M. Mittleman, M. Gupta, R. Neelamani, R. G. Baraniuk, J. V. Rudd, and M. Koch, "Recent advances in terahertz imaging," *Appl. Phys. B*, vol. 68, no. 6, pp. 1085 – 1094, 1999.

[195] http://www.cfa.harvard.edu/HITRAN/, HITRAN Database, Accessed April 2011.

[196] J. A. Zeitler, P. F. Taday, D. A. Newnham, M. Pepper, K. C. Gordon, and T. Rades, "Terahertz pulsed spectroscopy and imaging in the pharmaceutical setting: a review," *J. Pharm. Pharmacol.*, vol. 59, no. 2, pp. 209–223, 2007.

[197] S. Yoshida, E. Kato, K. Suizu, Y. Nakagomi, Y. Ogawa, and K. Kawese, "Terahertz sensing of thin Poly(ethylene Terephthalate) film thickness using a metallic mesh," *Appl. Phys. Express*, vol. 2, no. 1, 012301, 2009.

[198] S. Yoshida, K. Suizu, E. Kato, Y. Nakagomi, Y. Ogawa, and K. Kawese, "A high-sensitivity terahertz sensing method using a metallic mesh with unique transmission properties," *J. Mol. Spectrosc.*, vol. 256, pp. 146 – 151, 2009.

[199] F. Miyamaru, S. Hayashi, C. Otani, K. Kawase, Y. Ogawa, H. Yoshida, and E. Kato, "Terahertz surface-wave resonant sensor with a metal hole array," *Optics Lett.*, vol. 31, no. 8, pp. 1118 – 1120, 2006.

[200] F. Miyamaru, Y. Sasagawa, and M. W. Takeda, "Effect of dielectric thin films on reflection properties of metal hole arrays," *Appl. Phys. Lett.*, vol. 96, no. 2, 021106, 2010.

[201] Z. Tian, J. Han, X. Lu, J. Gu, Q. Xing, and W. Zhang, "Surface plasmon enhanced transmission spectroscopic distinguishing between isotopes," *Chem. Phys. Lett.*, vol. 475, pp. 132 – 134, 2009.

[202] R. Gordon, A. G. Brolo, A. McKinnon, A. Rajpra, B. Leathem, and K. L. Kavanagh, "Strong polarization in the optical transmission through elliptical nanohole arrays," *Phys. Rev. Lett.*, vol. 92, no. 3, 037401, 2004.

[203] T. H. Isaac, W. L. Barnes, and E. Hendry, "Surface-mode lifetime and the terahertz transmission of subwavelength hole arrays," *Phys. Rev. B*, vol. 80, no. 11, 115423, 2009.

[204] J. Homola, "Present and future of surface plasmon resonance biosensors," *Anal. Bioanal. Chem.*, vol. 377, pp. 528 – 539, 2003.

[205] http://www.biacore.com/lifesciences/index.html, BIAcore Life Sciences, Accessed May 2011.

[206] J. G. Rivas, "The art of confinement," *Nat. Photonics*, vol. 2, pp. 137 – 138, 2008.

[207] E. Kato, H. Yoshida, S. Hayashi, Y. Ogawa, and K. Kawase, "THz sensing method based on thin metallic mesh and an application for bimolecular sensing," in *Joint 31st International Conference on Infrared Millimeter Waves and 14th International Conference on Teraherz Electronics*, (Shanghai, China), p. 185, September 2006.

[208] A. Hassani and M. Skorobogatiy, "Surface plasmon resonance-like integrates sensor at terahertz frequencies for gaseous analytes," *Opt. Express*, vol. 16, no. 25, pp. 20206 – 20214, 2008.

[209] C. Huang and K. Najafi, "Fabrication of Ultrathin p++ Silicon Microstructures Using Ion Implantation and Boron Etch-Stop," *J. Microelectromech. S.*, vol. 10, no. 4, pp. 532–537, 2001.

[210] X. Ding, W. H. Ko, and J. M. Mansour, "Residual Stress and Mechanical Properties of Boron-doped p +-Silicon Films," *Sensor. Actuat. A-Phys.*, vol. 23, no. 1-3, pp. 866–871, 1990.

[211] M. J. de Boer, J. G. E. Gardeniers, H. V. Jansen, E. Smulders, M.-J. Gilde, G. Roelofs, J. N. Sasserath, and M. Elwenspoek, "Guidelines for Etching Silicon MEMS Structures Using Fluorine High-Density Plasmas at Cryogenic Temperatures," *J. Microelectromech. S.*, vol. 11, no. 4, pp. 385–401, 2002.

[212] H. Jansen, H. Gardeniers, M. de Boer, M. Elwenspoek, and J. Fluitman, "A survey on the reactive ion etching of silicon in microtechnology," *J. Micromech. Microemg.*, vol. 6, pp. 14–28, 1996.

[213] E. Gogolides, S. Grigoropoulos, and A. G. Nassiopoulos, "Highly anisotropic room-temperature sub-half-micron Si reactive ion etching using fluorine only containing gases," *Microelectron. Eng.*, vol. 27, pp. 449–452, 1995.

[214] H. Jensen, M. de Boer, J. Burger, R. Legtenberg, and M. Elwenspoek, "The black silicon method II: The effect of mask material and loading on the reactive ion etching of deep silicon trenches," *Microelectron. Eng.*, vol. 27, pp. 475–480, 1995.

[215] R. Legtenberg, H. Jensen, M. de Boer, and M. Elwenspoek, "Anisotropic reactive ion etching of silicon using $SF_6/O_2/CHF_3$ gas mixtures," *J. Electrochem. Soc.*, vol. 142, no. 6, pp. 2020–2028, 1995.

[216] A. Tserepi, E. Gogolides, C. Cardinaud, L. Rolland, and G. Turban, "Highly anisotropic silicon and polysilicon room-temperature etching using fluorine-based high density plasmas," *Microelectron. Eng.*, vol. 41-42, pp. 411–414, 1998.

[217] H. Zou, "Anisotropic reactive ioni deep beam etching with profile control using $SF_6/O_2$ plasma," *Microsyst. Technol.*, vol. 10, pp. 603–607, 2004.

[218] H. Jensen, M. de Boer, R. Legtenberg, and M. Elwenspoek, "The black silicon method: A universal method for determining the parameter setting of a fluorine-based reactive ion etcher in deep silicon trench etching with profile control," *J. Micromech. Microeng.*, vol. 5, pp. 115–120, 1995.

[219] Z. Duric, M. M. Smiljanic, K. Radulovic, and Z. Lazic, "Boron redistribution during SOI wafer thermal oxidation," in *25th International conference on Microelectronics (MIEL)*, (Belgrade, Serbia and Montenegro), pp. 313 – 316, May 2006.

[220] H. Seidel, L. Csepregi, A. Heuberger, and H. Baumgartel, "Anisotropic etching of crystalline silicon in alkaline solutions II: Influence of dopants.," *J. Electrochem. Soc.*, vol. 137, no. 11, pp. 3626–3632, 1990.

[221] C. R. Becker, D. C. Miller, and C. R. Stoldt, "Galvanically coupled gold/silicon-on-insulator microstructures in hydrofluoric acid electrolytes: Finite element simulation and morphological analysis of electrochemical corrosion," *J. Micromech. Microeng.*, vol. 20, no. 8, p. 085017, 2010.

[222] E. Hendry, F. J. Garcia-Vidal, L. Martin-Moreno, J. G. Rivas, M. Bonn, A. P. Hibbins, and M. J. Lockyear, "Optical control over Surface-Plasmon-Polariton-Assisted THz Transmission through a Slit Aperture," *Phys. Rev. Lett.*, vol. 100, no. 12, 123901, 2008.

[223] E. Berry, R. D. Boyle, A. J. Fitzgerald, and J. W. Handley, *Computer Vision: Beyond the Visible Spectrum. Advances in Pattern Recognition.*, ch. Time frequency analysis in terahertz pulsed imaging. London, UK: Springer Verlag, 2005.

[224] D. M. Mittleman, R. H. Jacobsen, R. Neelamani, R. G. Baraniuk, and M. C. Nuss, "Gas sensing using terahertz time-domain spectroscopy," *Appl. Phys. B*, vol. 67, pp. 379 – 390, 1998.

[225] M. M. Nazarov, L. S. Mukina, A. V. Shuvaev, D. A. Sapozhnikov, A. P. Shkurinov, and V. A. Trofimov, "Excitation and propagation of surface electromagnetic waves studied by terahertz spectrochronography," *Laser Phys. Lett.*, vol. 2, no. 10, pp. 471 – 475, 2005.

[226] Y. Yomogida, Y. Sato, R. Nozaki, T. Mishina, and J. Nakahara, "Comparative study of boson peak in normal and secondary alcohols with terahertz time-domain spectroscopy," *Physica B*, vol. 405, pp. 2208 – 2212, 2010.

[227] S. J. Kim, B. Born, M. Havenith, and M. Gruebele, "Real-time detection of protein-water dynamics upon protein folding by terahertz absorption spectroscopy," *Angew. Chem. Int. Ed.*, vol. 47, pp. 6486 – 6489, 2008.

[228] J. Rodriguez, M. D. Elola, and D. Laria, "Polar mixtures under nanoconfinement," *J. Phys. Chem. B*, vol. 113, pp. 12744 – 12749, 2009.

[229] P. Han, Y. W. Chen, and X. C. Zhang, "Application of Silicon micropyramid structures for antireflection of terahertz waves," *IEEE J. Sel. Top. Qunat.*, vol. 16, no. 1, pp. 338 – 343, 2010.

[230] P. H. Bolivar *Private Communication*, April 2011.

[231] F. Zhang and M. P. Srinivasan, "Self-assembeld molecular films of Aminosilanes and their immobilization capacities," *Langmuir*, vol. 20, pp. 2309 – 2314, 2004.

[232] D. F. S. Petri, G. Wenz, P. Schunk, and T. Schimmel, "An improved method for the assembly of amino-terminated monolayers on $SiO_2$ and the vapor deposition of gold layers," *Langmuir*, vol. 15, pp. 4520 – 4523, 1999.

[233] I. Haller, "Covalently attached organic monolayers on semiconductor surfaces," *J. Am. Chem. Soc.*, vol. 100, no. 26, pp. 8050 – 8055, 1978.

[234] N. Graf, E. Y. A. Lippitz, D. Treu, T. Wirth, and W. E. S. Under, "Optimisation of cleaning and amino-silinization protocols for Si wafers to be used as platforms for biochip microarrays by surface analysis (XPS, ToF-SIMS and NEXAS spectroscopy)," *Surf. Interface Anal.*, vol. 40, pp. 180 – 183, 2008.

[235] A. Abbas, A. Treizebre, P. Supiot, N. Bourzgui, D. Guillochon, D. Vercaigne-Marko, and B. Bocquet, "Cold plasma functionalized terahertz bioMEMS for enzyme reaction analysis," *Biosens. Bioelectron.*, vol. 25, pp. 154 – 160, 2009.

[236] H. Liu and P. Lalanne, "Microscopic theory of the extraordinary optical transmission," *Nature*, vol. 452, pp. 728–731, 2008.

[237] G. N. Zhizhin, M. A. Moskaleva, E. V. Shomina, and V. A. Yakovlev, "Edge effects due to propagation of surface IR electromagnetic-waves along a metal-surface," *JETP Lett.*, vol. 29, no. 9, pp. 486 – 489, 1979.

[238] L. Sun, C.-L. Chien, and P. C. Searson, "Fabrication of Nanoporous Nickel by Electrochemical Dealloying," *Chem. Mater.*, vol. 16, pp. 3125–3129, 2004.

[239] V. N. Datsko and A. A. Kopylov, "On surface electromagnetic waves," *Phys. Usp.*, vol. 51, no. 1, pp. 101 – 102, 2008.

[240] A. V. Kukushkin, "On the physical meaning of the Zenneck wave," *Phys. Usp.*, vol. 52, no. 7, pp. 755 – 756, 2009.